Thermal-Capillary Analysis of the Horizontal Ribbon Growth of Solar Silicon

A THESIS

SUBMITTED TO THE FACULTY OF THE GRADUATE SCHOOL

OF THE UNIVERSITY OF MINNESOTA

BY

Parthiv Daggolu

IN PARTIAL FULFILLMENT OF THE REQUIREMENTS

FOR THE DEGREE OF

DOCTOR OF PHILOSOPHY

Jeffrey J. Derby, ADVISER

December, 2013

© Parthiv Daggolu 2013
ALL RIGHTS RESERVED

Acknowledgements

First and foremost, I would like to thank my advisor, Prof. Jeffrey J. Derby, for his valuable guidance, support and patience during the five years of my graduate studies. This experience, as his graduate student, has truly enhanced my scientific thought process for conducting research and made me feel well prepared to pursue my career as a Research Scientist in industrial R&D. He contributed immensely towards improving my technical writing skills, presentation skills to describe my work and express my ideas, and always motivated me to strive for perfection. When I got the offer to work for SunEdison, but was under pressure to join right away, he was caring enough to let me go before writing and defending my thesis. This stands as an evidence of his generosity, flexibility and understanding towards me. I also thank my thesis committee members Professors Satish Kumar, Prodromos Daoutidis and Victor Barocas for their support and encouragement.

I am indebted to Andrew Yeckel, senior Research Associate in Prof. Derby's group, without whose contributions none of this work would be possible. His mentoring and worldly advice has been invaluable and something I will always treasure. It is an absolute delight to be in the company of Andrew and his wife Lisa, where they opened me up to a lot of exiting things about American culture ranging from interesting cuisines to cult movies of Coen Brothers. Gaurab Samanta, who joined as a postdoctoral scholar in Prof. Derby's group in 2010, has provided clarifications for my research whenever required through our elaborate technical discussions and computational roundtables. Nan Zhang

and Wei, fellow graduate students in Prof. Derby's group, were always quick to offer help and advice when in need. Gaurab and Nan have become my very good friends and are currently also my colleagues at SunEdison forming our own Derby group here. I would also like to acknowledge other Derby group members Jeff Peterson, Yutao Tao, Kerry Wang and various other visiting scholars I had the privilege of working with. I have fond memories of hanging out with all the group members at various conferences such as ICCG in China and ACCG in Monterey to name a few. I am also grateful to our collaborator, Dr. Bleil at Energy Materials research, who provided essential inputs, while still protecting his intellectual property, that helped me with major breakthroughs in my research. I would also like to thank Julie Prince, Teresa Bradahl and Mary Nissen who were very resourceful and handy with the administrative help.

I have met many talented and bright minds while at University of Minnesota and they all had an influence on me. Shameek Bose, a close friend from the department, is one of the persons whose versatile knowledge thoroughly impressed me and I enjoyed all of the stimulating intellectual discussions with him and our travels together. Reetam Chakraborty, not only a close friend from the department but also my roommate during all my years in Minnesota, is one of the most pleasant and genuine persons I have come across. I appreciate all of his guidance through my job hunt and interviewing process. Being part of the Titans Cricket Club and Minnesota Cricket Association has provided me with a constant source of entertainment, exciting summers during the cricket season, an amazing group of friends and a social life that I will dearly miss.

Finally, I am indebted to my family especially my parents Jhansi Lakshmi and Vivekanada Reddy. My dad, as a reader in Political Science, and my mom, as a lecturer in Botanical Sciences, have instilled in me a great respect and desire for higher education right from childhood and always provided me with the resources and helped me stay focused. My mom could not be here today, but I know how proud she would be with my achievements as this has been her dream for me. My sister, Chethana Daggolu, has always been there for me to share all of my happiness and lift my spirits through

the toughest of times. I don't know what I would do without her. I couldn't be more grateful for all the support I received over the years from my brother-in-law, Vinod Doddareddy, and all of my cousins, Kiran Patur, Deepa Rekha and Narendranath.

Dedication

to my Mom, ***Jhansi Lakshmi*** and Dad, ***Vivekananda Reddy***

Abstract

Horizontal ribbon growth (HRG) promises the growth of crystalline silicon at rates that are orders of magnitude greater than vertical ribbon growth technologies. If successful, this process would enable the production of higher-quality, near-single-crystalline silicon wafers at fraction of the cost of current production techniques. This fascinating process was first conceived by Shockley in late 1950's for silicon growth and was practiced by Bleil in the late 1960's for germanium growth. Large-scale development efforts were subsequently carried out by Kudo in Japan in the late 1970's and by the Energy Materials Corporation in the US in the early 1980's. However, after encouraging early results, experimental advances and process development efforts stalled, and this technique was abandoned in favor of growth methods that were easier to develop.

Unlike vertical meniscus-defined crystal growth processes, such as edge-defined film-fed growth (EFG), which are inherently stable, there are many failure modes that must be avoided in the HRG process. We argue that its successful operation will rely on a thorough understanding of system design and control-issues that are perhaps only feasibly addressed via computational modeling of the system. Towards these ends, we present a comprehensive thermal-capillary model based on finite-element methods to study the coupled phenomena of heat transfer, fluid mechanics and interfacial phenomena (solidification and capillarity) in the HRG process. Bifurcation analysis coupled with transient computations using this model reveals process limitations that manifest as failure mechanisms, such as bridging of crystal onto crucible, spilling of melt from the crucible, and undercooling of melt at the ribbon tip, that are consistent with prior experimental observations and suggests operating windows that may allow for stable process operation. Further, coupled impurity transport calculations reveal interesting and potentially beneficial redistribution mechanisms at the solidification interface that lead to an inherent purification of the majority of the growing crystal ribbon.

Contents

Acknowledgements **i**

Dedication **iv**

Abstract **v**

List of Tables **ix**

List of Figures **x**

1 Introduction **1**

1.1 Silicon PV technology 1

1.2 PV silicon crystal growth 5

1.2.1 Mono-crystalline silicon 5

1.2.2 Multi-crystalline Silicon 8

1.3 Ribbon growth techniques 10

1.3.1 Vertical Ribbon Growth (VRG) methods 11

1.3.2 Horizontal Ribbon Growth (HRG) method 15

2 Thermal-Capillay Model **22**

2.1 Field equations 22

2.2 Solidification interface 24

2.3 Capillary interfaces 25
2.4 Ribbon thickness 27
2.5 Melt level and outlet flows 28
2.6 Thermal boundary conditions 29

3 Numerical Methods **31**
3.1 Galerkin Finite Element discretization 31
3.2 Elliptic Mesh Generation 34
3.3 Boundary Conditions 36
3.4 Solution Methods 36

4 Thermal-Capillary Analysis **39**
4.1 Quasi-steady base case 42
4.1.1 Thermal field 42
4.1.2 Velocity field and menisci 46
4.2 Pull rate limitations 48
4.2.1 Pull rate, ribbon thickness, and solution multiplicity 48
4.2.2 Stability 51
4.3 Achieving higher pull rates 53
4.4 Conclusions 55

5 Stability Limits **58**
5.1 Limits with respect to pull rate 58
5.1.1 Crystal freezing onto crucible 59
5.1.2 Growth beyond the limiting pull rate 61
5.1.3 Spilling of the lower meniscus 63
5.1.4 Melt under-cooling at the ribbon tip 66
5.2 Limits due to pull angle and melt height 69
5.2.1 Pull angle 69

5.2.2 Melt height and batch operation 71
5.3 Conclusions 74

6 Segregation Analysis **77**
6.1 Thermal-capillary, species segregation model 79
6.2 Quasi-steady base case 81
6.3 Transient simulation 88
6.4 Effect of solute properties 88
6.5 Effect of pull rate 91
6.6 Limiting behaviors for carbon segregation 94
6.7 Conclusions 98

7 Concluding Remarks **100**
7.1 Thesis summary 100
7.2 Directions for future research 103
7.2.1 Coupled global modeling 103
7.2.2 Process instabilities 108
7.2.3 Thermal-stress analysis 111

References **116**

List of Tables

4.1 Sensitivity of results to the mesh size 40
4.2 Furnace heat transfer parameters and material properties used in all calculations performed here. 41

List of Figures

1.1 The global PV module price learning curve for c-Si wafer based modules [1] 2

1.2 (a) Schematic of the various production segments involved in c-Si PV module manufacturing (b) Cost breakdown of various processing steps as of 2010 [2] 4

1.3 (a) Schematic of the CZ process [3] (b) Experimental growth furnace of the CZ process [4] (c) CZ grown single crystal silicon ingot [4] 5

1.4 (a) Schematic of the FZ process [5] (b) Experimental growth furnace of the FZ process [6] 7

1.5 (a) Schematic of the casting and DS process (Adapted from [5]) (b) Experimental growth furnace of the DS process (Adapted from [7]) (c) Cast silicon ingot (Adapted from [8]) 8

1.6 (a) Schematic of inner diameter sawing [4] (b) Schematic of multi-wire sawing [4] 10

1.7 (a) Schematic of dendritic web process [9] (b) Schematic of string ribbon process [10] (c) Schematic of EFG process [11] (left), industrial EFG growth furnace [12] (middle), contrast of 10cm face and 12.5cm face EFG grown octagon ribbons [12] (right) 12

1.8 Typical defects seen in an etched cross-section of a 2.0 mm thick EFG ribbon [13] 14

1.9 Schematic of HRG system showing the domains of melt, crystal and crucible, along with the shape of extended growth interface and pulling direction 15
1.10 (a) Schematic of Kudo's HRG system [14] (b) Germanium ribbons grown by Bleil [15] (top) and silicon ribbons grown by Kudo [14] (bottom) (c) Schematic of the RGS system [16] (top) and optical microscope image showing columnar grain growth in RGS grown ribbon [17] (bottom) . . 17
1.11 Kudo's schematic illustrations of problems encountered in the HRG experiments [14]: (a) Bridging between seed and crucible (b) Melt spilling (c) Polycrystalline growth (plan view) 19
2.1 Crucible geometry and thermal boundary conditions for base case simulation of the HRG system along with illustration of growth angle, wetting angle and pinning conditions at melt–crucible junctions and at triple phase lines (TPLs). 23
3.1 Parametric mapping to a unit square parent element [18] 32
4.1 Top: Meshing scheme in the whole domain (The crystal extends beyond what is shown in the figure). Bottom: An enlarged view near the solidification interface showing stretching of the mesh near the free and moving boundaries(bottom) 40
4.2 Schematic of the heating and cooling arrangements in the HRG system. Notation corresponds to the description in Table 4.2 42

4.3 (a) Temperature field in the melt and crucible domains with T_{max} = 1702 K at the crucible bottom and T_{min} =1683 K at the growth interface. In color, higher temperatures are red and cooler temperatures are blue. Isotherm contour spacing is ΔT = 0.95 K. (b) Enlarged view near the growth interface with T_{max} = 1688 K at the bottom of crucible shelf and T_{min} =1672.5 K at the crystal edge after it exits the growth wedge region. Contour spacing is ΔT =1.1 K. (c) Heat-flux from top surface of the crystal in the growth wedge region with $\mathcal{F}_{max}$ = 75 W/cm^2 in the active cooling region and $\mathcal{F}_{min}$ = 22 W/cm^2 in the passive cooling region 43

4.4 For the base case simulation at V_g = 4.4 cm/min, temperature versus distance: (a) along line 1, showing horizontal thermal profile and (b) along line 2, showing vertical thermal profile. 44

4.5 Stream function contours in the melt domain with a flow rate of 1.72 mm^2/s between consecutive streamlines. Solid and dashed streamlines indicate vortices turning in the clockwise and counter-clockwise directions, respectively. Enlarged views: (b) near the ribbon tip, flow rate between streamlines is 1.75 mm^2/s; (c) near growth interface, flow rate between streamlines is 0.056 mm^2/s; and (d) near exit meniscus, flow rate between streamlines is 0.051 mm^2/s. 47

4.6 (a) Crystal thickness plotted as a function of pull-rate and compared with the prediction from idealized heat transfer analysis of Zoutendyk [19]. (b) Bifurcation into multiple branches presented in projections of growth interface length and wedge factor plotted as a function of pull rate. (c) Bifurcation plot in the projection of lower meniscus length versus pull rate. (d) Enlarged view near the growth interface for $P1$ and $P2$ showing the contrasting interfacial shapes. 50

4.7 (a) Time evolution of states on lower solution branch of prior figure after a step disturbance in pull rate at time $t = 0$. (b) Time integration of state $P2$ on upper solution branch of prior figure, without any initial perturbation. (c) Enlarged view near the growth interface during the evolution of simulation starting with state $P2$ on upper solution branch at $t = 0$ and $t = 8.5$ s. 52
4.8 (a) Crystal thickness plotted as a function of pull rate for three different crucible cantilever shelf lengths. (b) Wedge factor versus pull rate for the three different cases. 54
5.1 Variation of lower meniscus length(dashed curve) and crystal thickness(solid curve) with pull rate (b) Interfacial shapes for pull rates of $V_g = 5.6$ cm/min and $V_g = 4$ cm/min respectively, showing the contracting lower meniscus shape 60
5.2 (a) Evolution of crystal thickness(solid curve) and wedge factor(dashed curve) with time after a step change in pull rate from $V_g = 6.9$ cm/min to $V_g = 7.2$ cm/min, which is beyond the thermal-capillary limit (b) Evolution of interfacial shapes with time 62
5.3 Schematic of wetting and pinning of the lower meniscus along the crucible and crucible edge; see text for explanation. 63
5.4 (a) Shapes of the lower meniscus for different pull rates from $V_g = 4.8$ cm/min to $V_g = 6.8$ cm/min. Stable shapes are indicated by the solid curves; unstable shapes are indicted by dashed curves. (c) Contact angle as a function of pull rate, marked with regions of stability according to Gibbs limit. 65
5.5 Surface temperature profile along the upper meniscus and crystal surface, near the ribbon tip (above), plotted for three different pull rates of $V_g = 4.4$ cm/min, 5.3 cm/min, and 6.9 cm/min, showing regions of undercooled melt at higher growth rates (below). 67

5.6 Evidence of dendrites on a RGS grown ribbon from an undercooled melt [20] 68
5.7 Stability limits exist for the variations of other parameters. (a) Lower meniscus length plotted as a function of pull angle. (b) Interfacial shapes corresponding to the stability limits at P1 and P2 in (a). 70
5.8 Stability limits exist for the variations of other parameters. (a) Lower meniscus length plotted as a function of melt height. (b) Interfacial shapes corresponding to the stability limits at P1 and P2 in (a). 72
5.9 (a) Plot of crystal thickness(solid curve) and melt height(dashed curve) with time during a batch simulation of the process at V_g = 5 cm/min (b) Evolution of interfacial shapes with time 73
5.10 Stability limits and operating window with respect to pull rate 75
6.1 (a) Global representation shows a nearly constant composition field through the melt. (b) Expanded view of melt composition under the solidification interface; maximum concentration is $c_{max} = 4.52c_0$, minimum concentration is $c_{min} = c_0$, and contour spacing is $\Delta c = 0.58c_0$. (c) Expanded view of melt composition near lower meniscus; maximum concentration is c_{max} =94.3c_0, minimum concentration is $c_{min} = 3.64c_0$, and contour spacing is $\Delta c = 9.1c_0$. 83
6.2 (a) Solute concentration and cumulative distribution of solute in crystal are plotted as a function of crystal thickness; t=0 refers to the top crystal surface and t=t_0 refers to the bottom crystal surface. (b) Depiction of streamlines of melt flow in various zones under the solidifying crystal. . 84

6.3 (a) Solute concentration and tangential melt velocity close to the interface are plotted as a function of crystal thickness. Zone numbers refer to regions identified in previous figure. (b) Solute concentration and tangential melt velocity close to the interface are plotted as a function of crystal thickness in zone 3, near the bottom of the ribbon and the lower meniscus. 86
6.4 Temporal evolution of the concentration field near the solidification interface region: t = 1.7s - 1. Max $c = 4.05c_0$, Min $c = c_0$ 2. Max $c = 18.2c_0$, Min $c = 1.08c_0$; t= 10.25 s - 1. Max $c = 4.2c_0$, Min $c = c_0$ 2. Max $c = 60.7c_0$, Min $c = 2.68c_0$; t = 18.79s - 1. Max $c = 4.35c_0$, Min $c = c_0$ 2. Max $c = 94.2c_0$, Min $c = 3.64c_0$ 89
6.5 Temporal evolution of the impurity profile at various crystal portions along $t = 0$(top), $t = t_0/2$(center) and $t = t_0$(bottom) 90
6.6 Solute concentration is plotted as a function of crystal thickness for different equilibrium partition coefficients. 91
6.7 Solute concentration is plotted as a function of crystal thickness for different solute diffusion coefficients in the melt. 92
6.8 (a) Solute concentration is plotted as a function of crystal thickness for three different pull rates (b) The ratio of maximum to minimum solute concentration in grown crystal, which signifies the extent of redistribution, is plotted as a function of pull rate. 93

6.9 (a) Carbon redistribution for the case of the non-interacting crucible. Above: Concentration field in the melt near the solidification interface; maximum concentration is $c_{max} = 4.52c_0$, minimum concentration is $c_{min} = c_0$, and contour spacing is $\Delta c = 0.58c_0$. Below: Melt composition near lower meniscus; maximum concentration is $c_{max} = 94.3c_0$, minimum concentration is $c_{min} = 3.64c_0$, and contour spacing is $\Delta c = 5.5c_0$. (b) Carbon redistribution for the case of the crucible wall at saturation. Above: Concentration field in the melt near the solidification interface; maximum concentration is $c_{max} = 4.52c_{sat}$, minimum concentration is $c_{min} = c_{sat}$, and contour spacing is $\Delta c = 0.58c_{sat}$. Below: Melt composition near lower meniscus; maximum concentration is $c_{max} = 28.8c_{sat}$, minimum concentration is $c_{min} = 3.64c_{sat}$, and contour spacing is $\Delta c = 5.5c_{sat}$. 95

6.10 Carbon impurity concentration profile across the ribbon thickness for the limiting cases of a non-interacting crucible and a crucible at the saturation limit, labeled as $\mathbf{n} \cdot \nabla \mathbf{c} = \mathbf{0}$ and $c = c_{sat}$, respectively. 97

7.1 Melt crystal growth in an electrodynamic gradient freeze furnace is represented using coupled models. (a) Matching temperature and heat flux boundary conditions are exchanged between a finite volume furnace model and a finite element model of ampoule contents. (b) Temperature in the furnace is computed by CrysMAS, and temperature and melt flow in the ampoule are computed by Cats2D (adapted from [21]) 105

7.2 Schematic showing the division of the global system into subdomains comprising of the furnace design and the local HRG system. Furnace heat transfer will be modeled by the CrysMAS software while the local thermal-capillary physics will be modeled by the in-house Cats2D software with two-way modular coupling between the codes 107

7.3 The Floating Silicon Method (FSM), under development of Varian Semiconductor Equipment, grows silicon ribbon in a horizontal orientation, from [22] 110

7.4 (a) Typical liquidus temperature distribution in the presence of impurities and thermal gradients in melt near the growth interface: Scenario 2 corresponds to shallow gradients with melt temperatures falling below the liquidus temperature resulting in supercooled region. (b) Cellular structures developed on the interface during melt crystal growth of Ga doped Ge under the conditions of morphological instability [23] 111

7.5 Von-Mises stress field in the crystal: Min σ/G = -3.04x10^{-5}, Max σ/G = 1.99x10^{-2}, $\Delta\sigma$/G = 9.9x10^{-4} 114

Chapter 1

Introduction

1.1 Silicon PV technology

The development of renewable energy may be the most important challenge for the future of human civilization. Of overriding importance in the quest for renewable energy sources is the development of low-cost and reliable solar-to-electric conversion methods [24]. The vast majority of such methods rely on photovoltaic (PV) devices, or solar cells, to directly convert sunlight to electricity. The barrier for deploying such technologies comes down to a single number, the cost to produce electricity by solar cells, which in turn is determined by the efficiency of the solar cell, the production cost of the entire PV module, and the lifetime of the module. The current high cost of PV modules per watt produced remains the single most important barrier that must be reduced to make solar energy competitive with fossil fuels.

There has been over 30 years of research worldwide on terrestrial PV technology, with the outcome of many competing technologies and significant expansions of markets [25]. The most established technology is based on the fabrication of solar cells from crystalline silicon (c-Si), termed as 1st generation PV. Thin film technologies, referred to as 2nd generation PV, employ a more diverse range of semiconductor materials such as

amorphous silicon (a-Si), cadmium telluride (CdTe) and copper-indium-gallium-selenide (CIGS) offering lower material and manufacturing costs. However, poor conversion efficiencies and concerns over toxicity of some of the materials involved remain a major barrier to compete with the conventional silicon based technologies. 3rd generation PV technologies such as concentrating PV (CPV), dye-sensitized solar cells (DSSC) and organic solar cells are still in developmental stages and have not yet been commercialized. Currently, crystalline silicon wafer based solar cell production dominates the market accounting for 85% of the global PV sales in 2010 [26], and the most likely scenario is that this technology will continue to dominate for the next decade and probably longer [25].

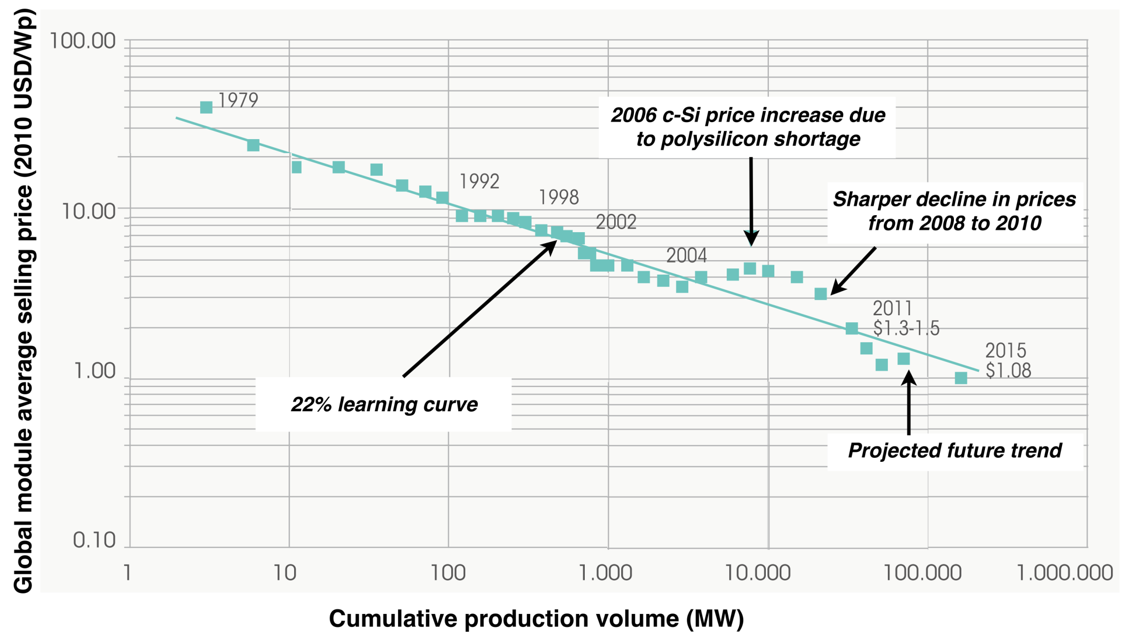

Figure 1.1: The global PV module price learning curve for c-Si wafer based modules [1]

The capital cost of a c-Si PV system can be decomposed into costs associated with the manufacturing of the PV module; structural installation costs for site preparation,

mounting and racking of the PV system; electrical installation costs involving inverters, wiring and other miscellaneous electrical components; and storage system costs of batteries. Among these, the PV module cost itself typically accounts for around half of the total capital cost of a PV system [1] and a continued reduction of the module costs is essential to achieve grid parity in the near future. The trends in the module prices over the years, shown in Fig 1.1, reveal a characteristic 22% learning curve, meaning that the module costs have gone down by roughly one-fifth for every doubling of the production capacity. In the recent years, the average global price of c-Si PV modules underwent a much sharper decline from $4.05/W in 2008 to $2.21/W in 2010 [27] and such a decline needs to be further maintained via breakthrough technological innovations in manufacturing.

PV module manufacturing commences with the purification of the quartzite mineral to metallurgical grade silicon and further to solar grade polysilicon. The polysilicon feed rod is then melted and carefully resolidified via an appropriate crystal growth technique to yield crystalline material which is then processed into wafers of a specified size and thickness. These wafers are ultimately used to fabricate the solar cells and are arranged into a PV module. These various processing segments involved are shown schematically in Fig 1.2a and a break down of the associated costs, shown in Fig 1.2b, emphasizes that the crystal growth and wafer production costs does contribute to a significant portion of the total PV module cost. Furthermore, efficiency of the module is strongly dependent upon material quality, which ultimately again relates back to crystal growth processes, where controls of defects and impurities can best be put into place. For continued development of the c-Si PV technology, Surek [28] argues that, for a given cell and module, the use of a crystalline wafer resulting in the highest efficiency is generally preferred over the cheapest wafer or process. Therefore, advances in crystal growth that reduce cost and maintain or increase cell efficiency are required and to realize the scope for such improvements, a review of the current silicon crystal growth technologies is presented in the ensuing section.

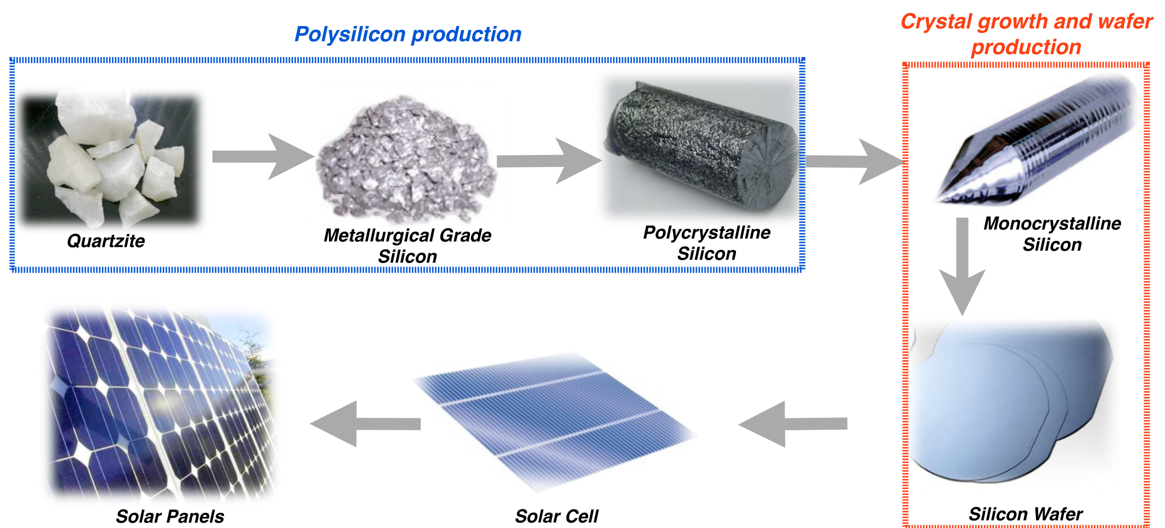

(a)

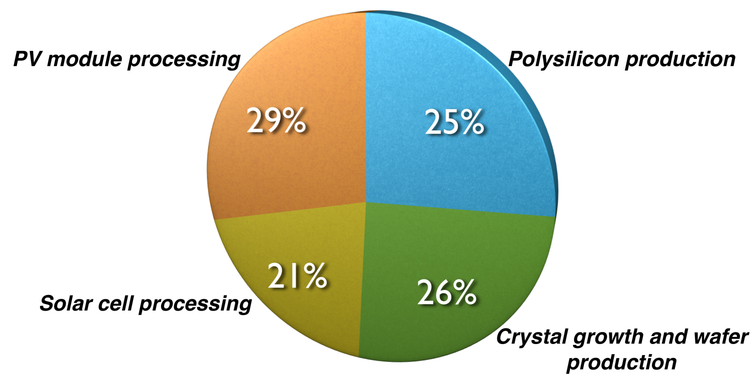

(b)

Figure 1.2: (a) Schematic of the various production segments involved in c-Si PV module manufacturing (b) Cost breakdown of various processing steps as of 2010 [2]

1.2 PV silicon crystal growth

1.2.1 Mono-crystalline silicon

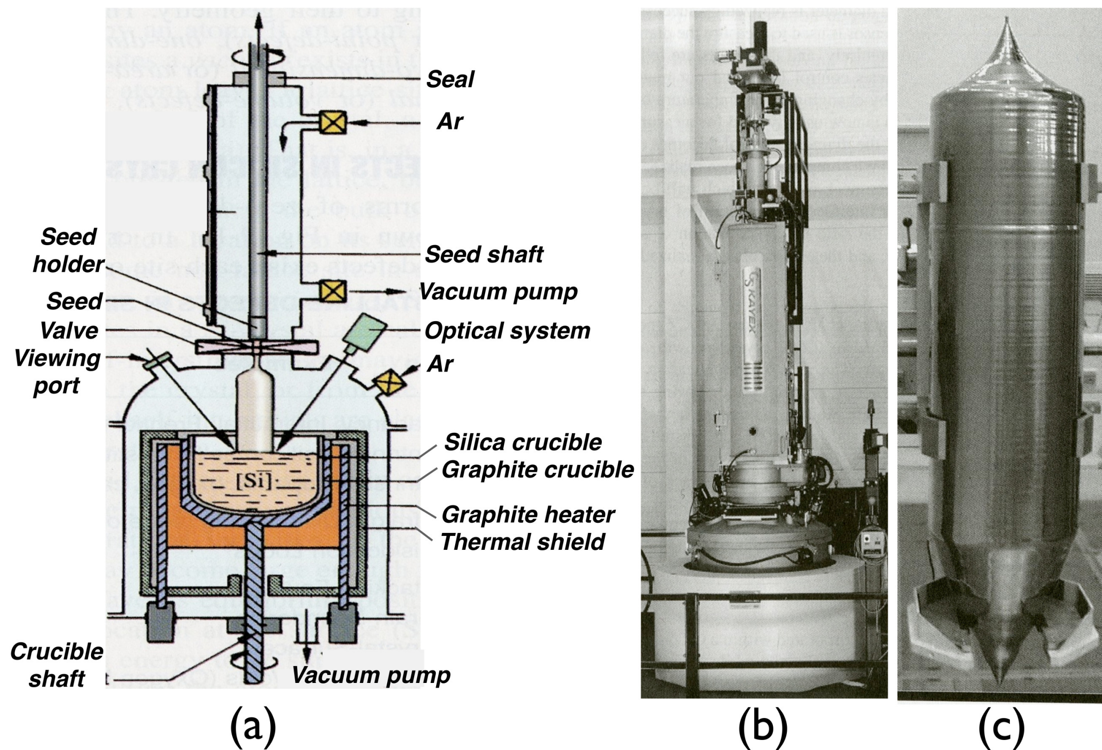

Figure 1.3: (a) Schematic of the CZ process [3] (b) Experimental growth furnace of the CZ process [4] (c) CZ grown single crystal silicon ingot [4]

Mono-crystalline or single crystal silicon possesses a continuous periodic arrangement of atoms in a diamond cubic lattice, throughout the entire solid unbroken to its edges, with the absence of any grain boundaries and dislocations. The modern day electronic devices are fabricated almost exclusively on only mono-crystalline silicon wafers, where billions of transistor-based circuits are combined into a single chip to manufacture, for example, a microprocessor. The presence of grain boundaries, dislocations and other crystallographic defects such as point defect clusters can adversely affect the

performance of such electronic devices, thereby making the single crystal silicon growth techniques and facilities an integral part of the electronics industry. Mono-crystalline silicon is also increasingly used in the fabrication of high-performance and high-efficiency solar cells, albeit at higher costs. Czochralski and Float-Zone are the two established single crystal silicon growth techniques, employed in both the electronics and the PV industries.

Czochralski (CZ) technique, named after its inventor and pioneered in the early 1950's for silicon growth, involves pulling of a mono-crystalline cylindrical ingot of silicon from its melt, and a schematic of the growth process is shown in Fig 1.3. A charge of electronic grade silicon is first loaded into a fused-silica crucible and melted, in a chamber filled with an inert atmosphere. A seed crystal of precise crystallographic orientation is then lowered into the melt and pulled away continuously, along with simultaneous rotation of the seed-crystal and crucible in opposite directions, promoting the growth of crystalline silicon at the melt/solid interface. After the initial neck formation to eliminate the propagation of dislocations (Dash technique [29]), the pulling is then controlled to achieve and maintain a prescribed diameter for the remainder of the growth, typically in the range of 200-300 mm, until the charge is nearly exhausted, at which point the ingot is withdrawn and a bottom tail section develops. The relative simplicity of this process, along with the development and integration of sophisticated automatic monitoring and control, helped the CZ process emerge as the dominant technology to grow mono-crystalline silicon, for electronics industry, in a highly reproducible and routine fashion. In 2010, approximately 36% of PV module production also employed silicon grown using the conventional Czochralski (CZ) process [30]. Efficiencies of the best, commercially-available CZ silicon solar cells are in excess of 21%, with efficiencies of "champion" solar cells exceeding 25% [31]. However, this process is also characterized by slow growth rates, long process turn-around times, and exceedingly higher costs.

Float-Zone (FZ) is a crucible-free growth technique, shown schematically in Fig

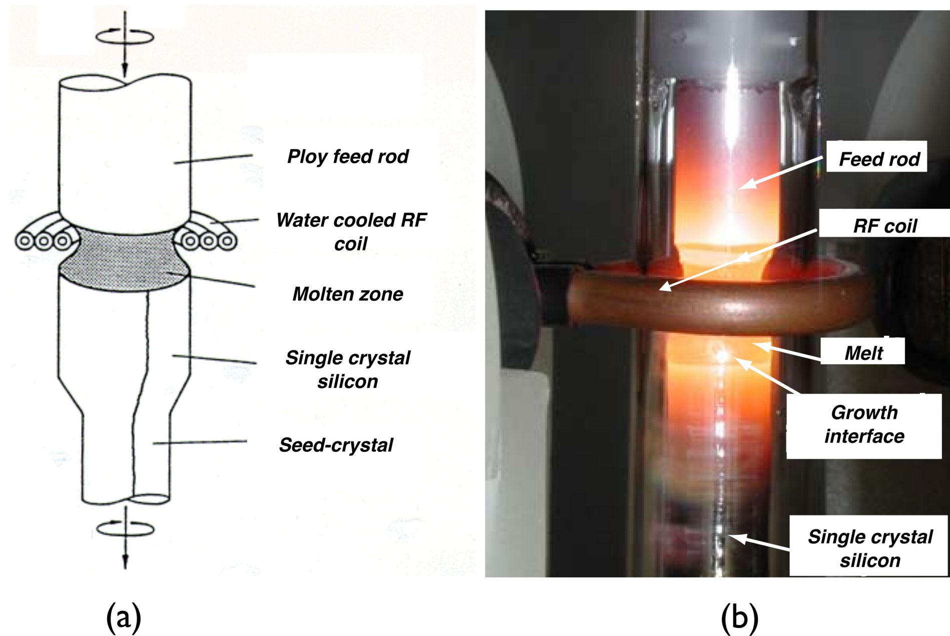

Figure 1.4: (a) Schematic of the FZ process [5] (b) Experimental growth furnace of the FZ process [6]

1.4, and presents the potential to grow higher purity mono-crystalline silicon than CZ process. In CZ process, the presence of silica crucible presents the problem of oxygen impurity incorporation into the growing crystal at high concentrations, that can reduce the minority carrier lifetime in the solar cell and the resulting efficiency [32]. In FZ growth, a rotating polycrystalline feed rod of electronic grade silicon is passed through a Radio Frequency (RF) heating coil to form a localized molten zone at an edge of the feed rod. This molten zone, supported by the surface tension and electromagnetic forces, is brought into contact with a seed-crystal, rotating in the opposite direction, to promote growth at the interface. The technical challenges and instabilities involved with crucible-free growth limit growing large diameter ingots to 200 mm [33] and are often associated with higher costs. FZ grown wafers are typically only utilized for laboratory scale study of high-efficiency solar cells and are seldom used for commercial production [34].

1.2.2 Multi-crystalline Silicon

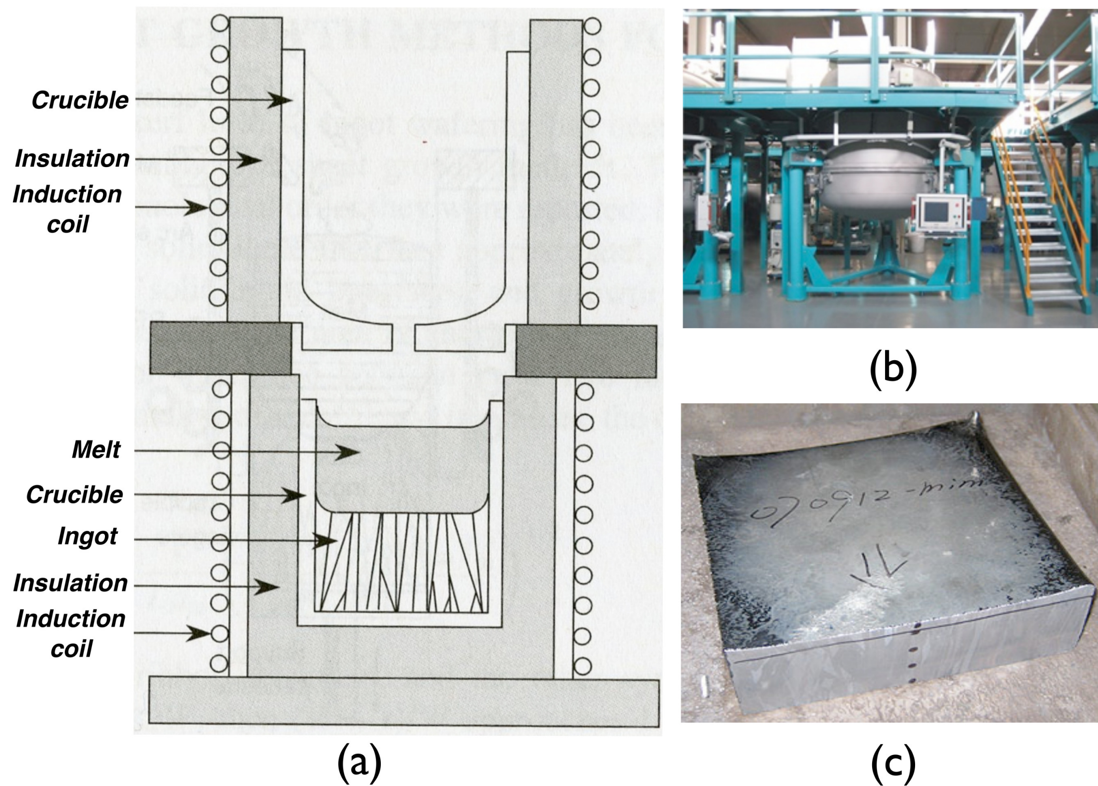

Figure 1.5: (a) Schematic of the casting and DS process (Adapted from [5]) (b) Experimental growth furnace of the DS process (Adapted from [7]) (c) Cast silicon ingot (Adapted from [8])

Unlike in electronics industry, PV silicon is more forgiving in terms of crystal perfection and multi-crystalline ingot growth methods emerged as an attractive alternative, which compromise on crystal quality to yield low-cost PV-cells of somewhat reduced efficiency due to grain boundary effects. However, this is offset by the relatively simpler equipment, lower required power inputs, reduced manpower, reduced operator skill and large ingot batch sizes that ultimately will result in a better cost per watt produced. Further, the efficiency reduction can be made to be not too drastic, if the grain size is

controlled to be in the order of mm to cm in width with an approximately columnar structure along the growth direction.

In the casting technique, shown schematically in Fig 1.5a, the feed silicon charge is first melted in a separate crucible and is then poured into a second crucible where it is solidified directionally starting from the bottom of the crucible. Alternatively, the silicon can be melted and directionally solidified in the same crucible and this technique is referred to as directional solidification (DS). Since melting and solidification is decoupled in the casting technique, it offers higher throughputs while the equipment and operation is simpler in directional solidification and both the techniques yield large ingots of multi-crystalline silicon. Growth rates are in the range of 1-2 mm/min and material production rates are 10-20 kg/hr, and it accounted for approximately 49% of worldwide PV module production in 2010 [30]. Multicrystalline silicon ingots are available commercially with cell efficiencies over 18% and champion cells have been fabricated with over 20% efficiency [31].

After a mono-crystalline or multi-crystalline ingot has been grown by any of the aforementioned techniques, a complex sequence of sawing and polishing steps are performed to produce wafers suitable for fabrication of solar cells. Running the ingot through an inner-diameter (ID) saw with stainless steel blades, coated with diamond particles to its edges, has been the conventional method adapted for sawing of ingots into wafers. However, in the recent times, ingots are typically sawn by pressing them against equally-spaced and properly-tensioned multiple stainless-steel wires under the injection of a slurry filled with abrasive particles. The throughput of wire sawing is superior to ID sawing as multiple wafers can be sliced in a single pass while also yielding more slices-per-inch of ingot due to efficient slicing.

The abrasive action during sawing of ingots into wafers results in loss of the material, termed as kerf losses, and the material yield (i.e., number of wafers produced per kilogram of silicon ingot) is estimated to be only 50–55% [35]. It can further introduce

defects, fractures and micro-cracks in the crystalline wafers affectting the material quality [36]. The silicon wafer contributes to 40–60% of the total fabrication cost of the PV cell [37] while the wafering technology itself contributes to roughly 2/3 of the total wafer production cost [35]. However, silicon wafer production in the current solar market is still predominantly based on cutting of large ingot crystals [36], thereby leaving a huge potential for cost reduction by circumventing this detrimental sawing process.

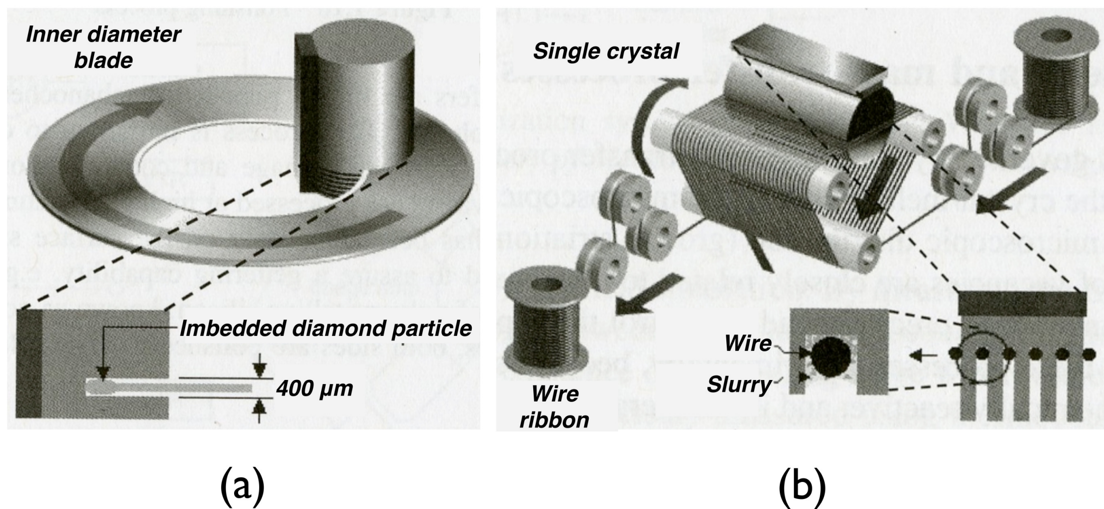

Figure 1.6: (a) Schematic of inner diameter sawing [4] (b) Schematic of multi-wire sawing [4]

1.3 Ribbon growth techniques

The shortage of silicon feedstock is a major barrier in driving the c-Si PV module prices lower and is a bottle-neck for the promising growth of this technology, placing an ever increasing emphasis on the efficient utilization of the feedstock material. This provided motivation for the innovation of a plethora of ribbon growth techniques, targeting the PV market, to directly grow crystalline silicon sheets in the final form, suitable for cell fabrication, and completely eliminate kerf losses and expenses associated with sawing

of ingots. Further, ribbon growth is less intensive in terms of energy consumption compared to ingot growth and can significantly reduce the energy payback time of the PV module [38]. These factors, put together, can achieve considerable decline in the wafer production costs and can lower the cost-per-watt produced of c-Si PV modules, if reasonable efficiencies are maintained. Various ribbon growth techniques, conceptualized and developed over the years, can broadly be classified into two categories: Vertical ribbon growth methods, characterized by a small-area solid/liquid interface, and horizontal ribbon growth methods, characterized by a large-area solid/liquid interface.

1.3.1 Vertical Ribbon Growth (VRG) methods

The dendritic web process, reported by Dermatis and Faust [39] in 1963, is one of the earliest developed ribbon growth techniques adapted for commercial production. In this process, a flat dendrite seed with (111) face is initially contacted with a supper cooled melt to grow a thermally-controlled lateral button, which is then raised to propagate growth of secondary dendrites from each end of the button, acting as bounding dendrites, while trapping a silicon web between them that crystallizes into ribbon. The technique was applied successfully to grow single crystal silicon ribbons of thickness 100–200μm and widths reaching up to 80 mm, with low dislocation densities and efficiencies as high as 15.5% [9]. However, acute temperature-control requirements, to initiate the web formation and to ensure steady dendrite propagation at the edges, demands a complex furnace design and renders the process technically intensive. In order to eliminate these stringent requirements, a more industrial friendly technique called string ribbon is adapted by Evergreen Solar [10] where the bounding dendrites are replaced by foreign filaments, typically carbon based, to facilitate the formation of the silicon web.

Edge-defined film-fed growth (EFG), first reported by Ciszek [13, 40] in 1972 and later developed by Mobil Solar [41, 42], was the most commercially established ribbon growth technique in the PV market. This process involves a shaping die immersed into the melt, as shown schematically in 1.7c, which rises through the die channels by the

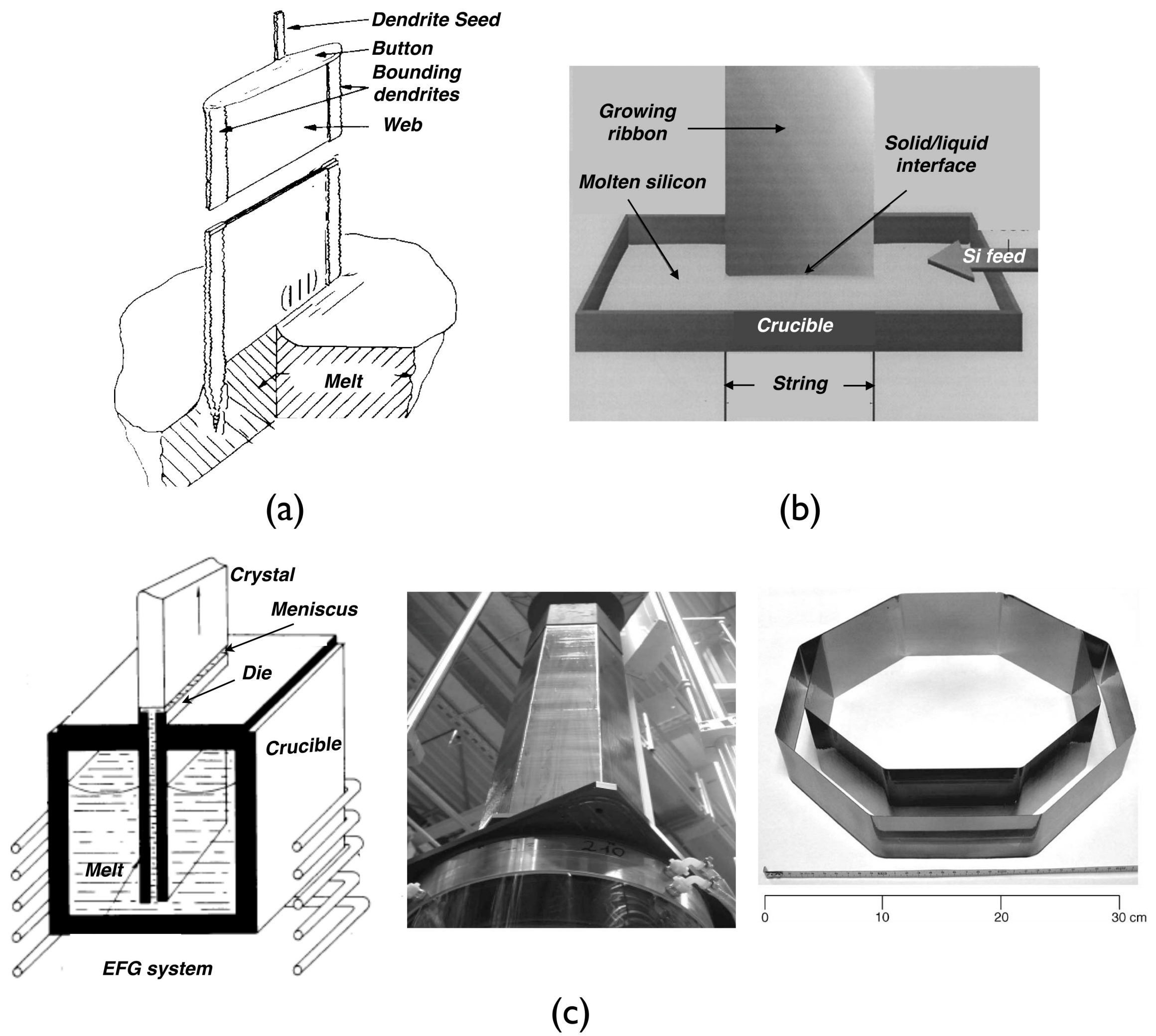

Figure 1.7: (a) Schematic of dendritic web process [9] (b) Schematic of string ribbon process [10] (c) Schematic of EFG process [11] (left), industrial EFG growth furnace [12] (middle), contrast of 10cm face and 12.5cm face EFG grown octagon ribbons [12] (right)

action of capillarity to reach the die top surface. It is then contacted by a seed crystal that spreads the melt over the die top till it reaches the die top edges, where it pins itself, thereby forming a meniscus. The seed crystal is then pulled continuously in the vertical direction promoting the growth of a ribbon whose cross-sectional shape is defined by the die edges. Graphite or silicon carbide coated with graphite are usually chosen for the shaping die material as they can withstand the high temperatures involved, present good wetting characteristics and are not detrimentally reactive with the silicon melt. Ribbons of 200–300μm thickness are grown typically in the form of hexagonal or octagonal closed tubes, to prevent edge instabilities, with 100–150 mm wide faces and PV cell blanks are laser-cut from the flat tube walls.

Vertical ribbon methods employ pulling rates in the range of 1–2 cm/min [44, 45], an order of magnitude higher than the ingot methods, yielding throughputs of 1–2 m^2/day for dendrite and string ribbon growth and about 20 m^2/day for EFG tube growth. However, these throughputs are still an order of magnitude lower than the ingot methods, despite faster pulling rates, due to their characteristic small-area solid/liquid interface. Rapid rates of radiative cooling, facilitated by the large surface-to-volume ratio of the ribbon, are employed to dissipate the latent heat of crystallization released at the growth interface and realize such fast pulling rates. However, at the same time, this also results in a deleterious build up of high non-uniform thermal gradients in the crystal, in the order of 500-1000 K/cm, giving rise to large thermal stresses as adjacent ribbon elements contract differently, proportional to their own temperature fall, and restrain each other's contraction. One of the mechanisms for stress relaxation in the crystal comes from in-plane plastic deformation and creep, arising from the slip and glide motion of the dislocations, contributing to a multiplication of dislocation densities to the order of $10^7 cm^{-2}$ causing further deterioration of the crystal quality [46, 12, 47, 48, 49]. When creep is inadequate to accommodate the build up of thermal stresses, relaxation occurs by means of out-of-plane buckling of the crystal resulting in large deviations from ribbon flatness rendering it useless for cell fabrication [46, 50, 51, 52]. According

to the plate bucking theory, the critical stress for buckling decreases as $(t/w)^2$ [53], where t is the crystal thickness and w is the width, implying that thermal stresses place severe limitations on developing these techniques to achieve wider and thinner ribbons at higher throughputs.

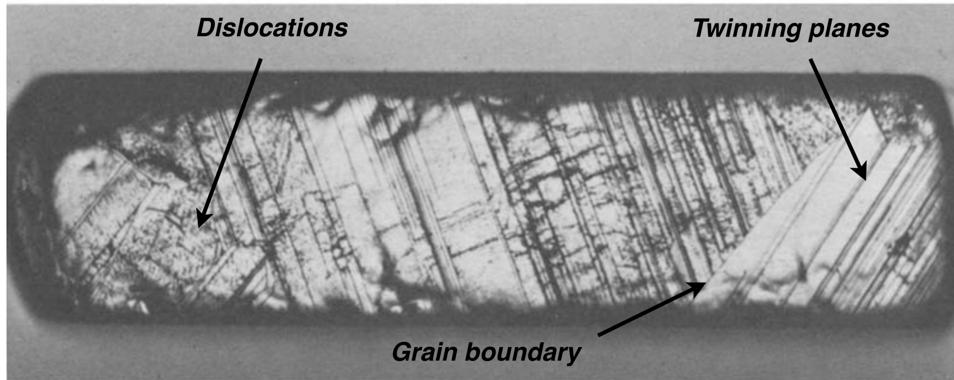

Figure 1.8: Typical defects seen in an etched cross-section of a 2.0 mm thick EFG ribbon [13]

The graphite shaping die, employed in EFG techniques to provide capillary rise, undergoes a continual erosion through reaction-diffusion processes and leads to high levels of carbon contamination in the melt. Once these impurities reach the solidification interface via transport processes, they get incorporated into the crystal at concentrations in the order of 2–3X10^{18}atoms/cm^3 [12] and introduces various types of crystallographic defects [42, 54]. Some of these defects such as dislocation arrays, grain boundaries and silicon carbide inclusions lead to significant local reductions in the carrier lifetimes due to strong electrical recombination activity. In addition, the unique twin lamellae structures commonly observed in EFG silicon have been attributed to high levels of carbon in the melt, which subsequently precipitates as layers between twinned crystals of silicon [55, 36]. These twinned regions correspond to high levels of residual stress causing concerns of ribbon fracture during processing of the PV cell blanks. Due to the high density of these various defects, EFG cell efficiencies are limited to 14–16% [25, 36], even after the utilization of lifetime enhancement processing such as gettering

and hydrogen passivation. These limitations described above act as impediments to the promising growth of VRG techniques, despite its advantage of efficient material utilization, and currently do not contribute to the commercial market.

1.3.2 Horizontal Ribbon Growth (HRG) method

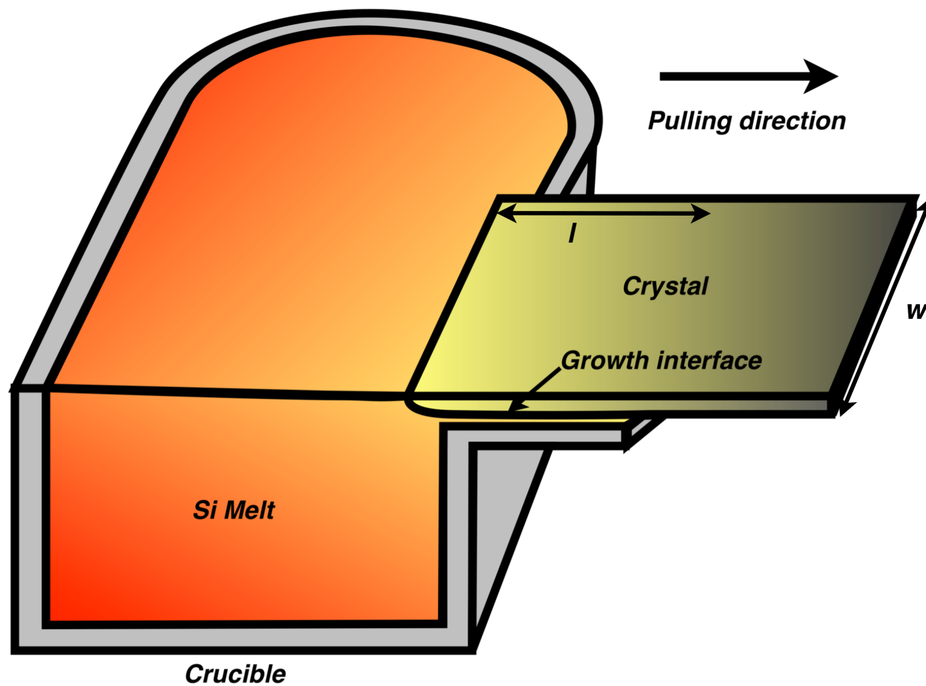

Figure 1.9: Schematic of HRG system showing the domains of melt, crystal and crucible, along with the shape of extended growth interface and pulling direction

The horizontal ribbon growth (HRG) technique, depicted schematically in Fig 1.9, promises to overcome many of the limitations associated with vertical ribbon growth methods. The compelling idea behind HRG is that the crystallization interface is stretched over a long distance, proportional to the length l indicated in Fig 1.9, which provides a much greater area over which the latent heat of solidification can be dissipated. Silicon releases a significant amount of heat upon phase change, and its removal from the system, as we have seen in the EFG system, is the limiting factor for attaining

fast growth rates [56]. In addition, the HRG method achieves growth without a carbon shaping die, such as employed by EFG, eliminating the prime source of carbon contamination of the melt and the crystal. Further, the furnace design in the system can be engineered to remove latent heat in a direction roughly perpendicular to the pulling direction, decoupling the pulling and the growth rates, and help achieve far higher pulling rates under far lower thermal gradients than in the vertical methods. Attaining a purer melt and reduced thermal gradients in the crystal allow for the possibility of higher quality, even single-crystalline, material growth by the HRG method.

In the late 1950s, Shockley first envisioned a process [57] that would grow thin silicon ribbons horizontally, supported by a molten material. The first practical implementation of the HRG process was achieved by Bleil in the late 1960s [15, 58], who succeeded in growing thin ribbons of ice and germanium. His process involved pulling the ribbon horizontally over the melt surface, with submerged heaters at the bottom and heat sinks at the top, to form a wedge shaped growth interface extending over several centimeters. In the late 1970s and early 1980s, focus had shifted towards the production of silicon ribbons for photovoltaic substrates by this technique. Subsequent development of the process for silicon growth was carried out through the mid-1970s to early 1980s in Japan under the Sunshine Project, as reported by Kudo [14, 59]. With several modifications in furnace design over Bleils configuration, Kudo demonstrated growth rates of 41.5 cm/min for single-crystal and 85 cm/min for multi-crystalline silicon, with thickness and width in the ranges of 200–400μm and 10–30 mm respectively and lengths reaching up to 2 m in a typical growth operation. Ribbon crystals were grown with dislocation densities of about 10^5cm^{-2}, with some sections of the ribbon completely dislocation free, and carbon concentrations of the order 10^{17}atoms/cm^3, significantly lower than EFG grown ribbons, and cells fabricated from these ribbons were reported to have nearly similar efficiencies as CZ crystals.

A similar effort in this time frame in the U.S. at the Energy Materials Corporation led to the development of the low-angle silicon sheet (LASS) growth process [60] where

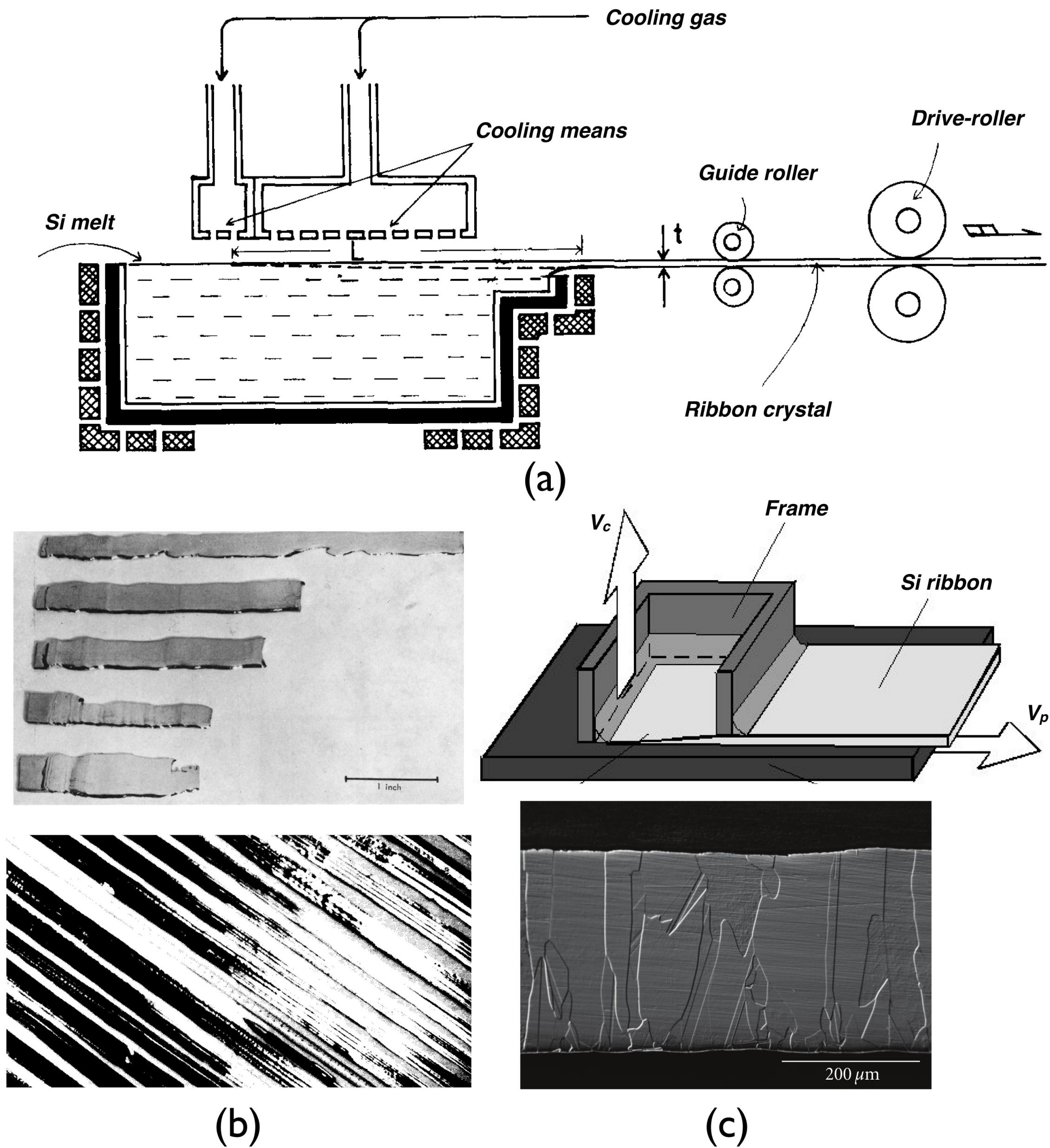

Figure 1.10: (a) Schematic of Kudo's HRG system [14] (b) Germanium ribbons grown by Bleil [15] (top) and silicon ribbons grown by Kudo [14] (bottom) (c) Schematic of the RGS system [16] (top) and optical microscope image showing columnar grain growth in RGS grown ribbon [17] (bottom)

growth rates of up to 60 cm/min were demonstrated. In very recent work, Ydstie and co-workers [61], inspired by the Pilkington float-glass process, proposed a horizontal silicon growth process similar to that of Shockley and produced a prototype HRG system to grow ice. A variant of the HRG process came into development in late 80's, termed as Ribbon Growth on Substrate (RGS), where the extended wedge-shaped interface is supported on a moving substrate as apposed to just floating on top of the melt [62]. The substrate gives rise to multiple nucleating sites and a consequent columnar grain structure in the growing ribbon and doesn't hold the promise of single-crystalline growth offered by the HRG process.

In spite of these promises, however, the HRG process is yet to be applied successfully for the production of solar silicon due to a host of challenges that disrupt stable growth conditions and must be addressed to make the HRG process work reliably. First, a precise control over heat transfer is needed to maintain the delicate balance of heat fluxes associated with the extended interface in HRG. Namely, the latent heat of solidification must be induced to travel primarily vertically, even though the sheet is being horizontally pulled, at a rapid rate, from the melt pool. Early efforts relied on passive cooling of of the top of the crystal by radiation and natural convection and further improved by Kudo [14] via active cooling using directed flows of helium gas toward the top surface, as shown in Fig 1.10a.

Additional challenges for stable HRG growth arise from the complicated interfaces in this system. Namely, the HRG process is subject to a number of potential edge instabilities that are not present in vertical, sheet growth methods. First, consider that the vertical edges of each flat face in the EFG process are connected by the bends of the closed octagonal tube (see Fig 1.7c), while the lateral edges defining the width (w in Fig 1.9) of the sheet in the HRG process are constrained only by the thermal field set up across the surface of the melt. In addition, unlike vertical systems, where the interplay of meniscus dynamics, sheet thickness, and gravity assures inherent shape stability during growth [63, 64, 65, 66], HRG can exhibit meniscus failure modes. The

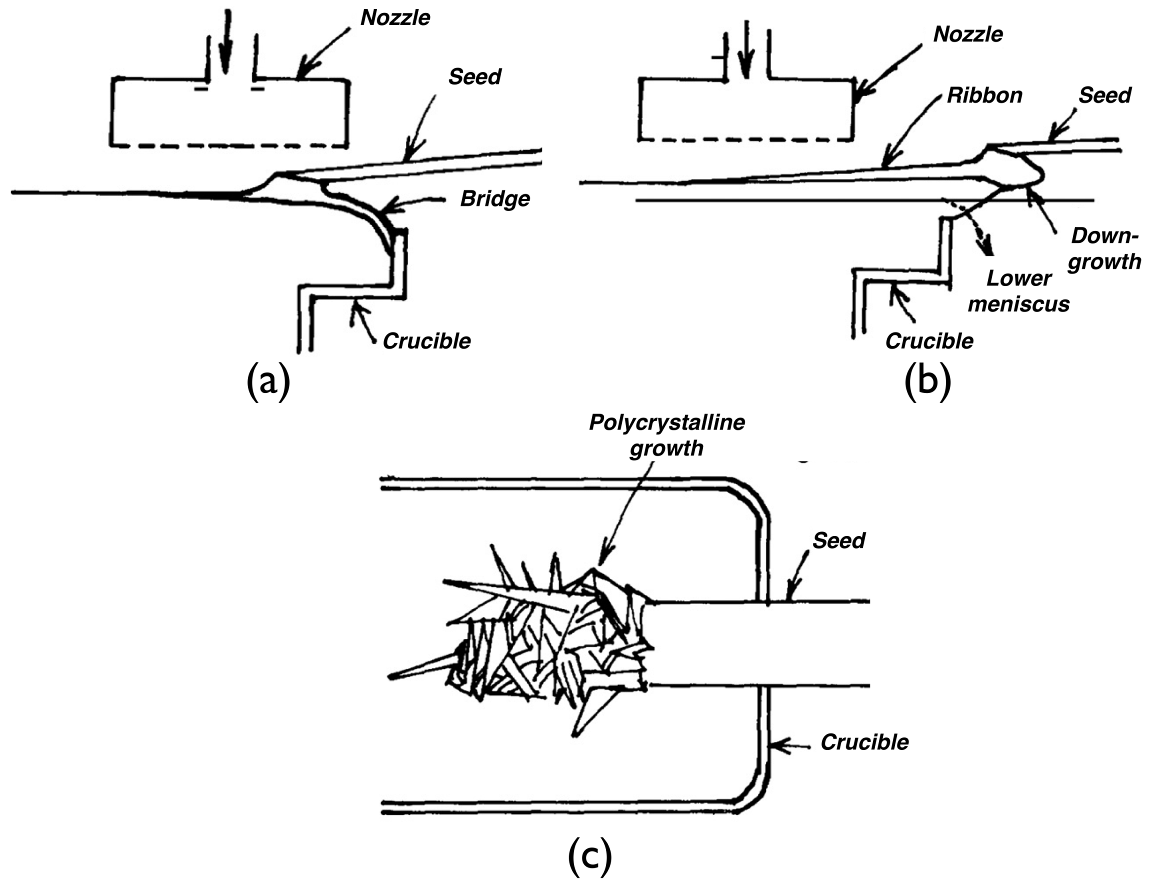

Figure 1.11: Kudo's schematic illustrations of problems encountered in the HRG experiments [14]: (a) Bridging between seed and crucible (b) Melt spilling (c) Polycrystalline growth (plan view)

lower meniscus, that connects the sheet with the front edge of the crucible by capillary forces as shown in Fig 1.11, is especially problematic, prone to breakage and subsequent melt spilling, if it is too long, and to freezing and bridging the ribbon to the crucible, if it is too short [15, 14]. Finally, the large rate of heat removal from the top surface of the melt needed to realize fast growth rates has led to reported supercooling followed by polycrystalline dendritic growth from the tip of the growing crystal as depicted in Fig 1.11 [14, 20]. A major objective of the thermal-capillary model that we develop here is to understand the cause and possible avoidance of these failure mechanisms.

Zoutendyk [19] was among the first to analyze heat transfer in the HRG process. By specifying the shape of the melt-solid interface and the thickness of the sheet, along with assuming a linear form of the temperature field in the crystal, he was able to relate pull speed, ribbon thickness, and thermal conditions in the melt for several limiting cases of heat removal by radiation from the top crystal surface and an isothermal top crystal surface, which was referred to as a heat clamp condition. A similar analysis was conducted by Kudo and Tamai [14] to elucidate the wedge factor, i.e., the extent of spreading of the melt-crystal interface across the surface of the melt, needed to support large growth rates in their system. In a later analysis, Zoutendyk [67] extended his model to account for forced convective heat transfer within the melt via a boundary layer analysis and also employed active cooling of the ribbon surface into their calculations.

Glicksman and Voorhees [68] performed an analysis of the morphological stability of the HRG process using an analytical form of a thermal field that was more appropriate than assumed by Zoutendyk [19], although Glicksman and Voorhees also employed the highly idealized heat clamp condition to specify the temperature along the upper surface of the crystal. They found that this model predicted inherent morphological stability for the process operating under reasonable conditions. In the most recent analysis of the HRG system, which now dates back 20 years, Thomas and Brown [56] used finite element models to probe the different operating behaviors of vertical and horizontal silicon sheet growth. Interestingly, while Thomas and Brown employed a thermal-capillary model to

compute coupled heat transfer, melt-crystal interface position, and meniscus shape for the vertical EFG system, they neglected the melt meniscus in the horizontal system and applied a rather idealized thermal boundary condition of a linear temperature profile along the lower side of the pulled silicon sheet. Even with these idealizations, they were able to better define the relationship between the aspect ratio of the interface (what Kudo referred to as the wedge factor), the growth rate, and heat transfer. Rhodes *et al.* [69] investigated the behavior of the meniscus connecting the crucible lip to the lower surface of the HRG crystal by solving two-dimensional Euler-Laplace capillary equation; however, they did not consider heat transfer effects.

While these prior models have elucidated many aspects of heat transfer, interface shape, and pull rate in the HRG system, all have critical shortcomings. Namely, all have treated heat transfer from the sheet in extremely idealized manners and are therefore unable to directly address furnace heat transfer design issues. In addition, none have addressed the modeling of the dynamics of the lower melt meniscus in this system, which represents a feature which may significantly impact the stability of the system. What is needed are comprehensive models that realistically represent all of these coupled phenomena of heat transfer, melt convection and capillary effects together in one model for the horizontal configuration. We address these shortcomings in the model presented here and demonstrate that the resulting comprehensive, thermal- capillary model provides insights into many of the limiting factors associated with the HRG system.

Chapter 2

Thermal-Capillay Model

Realistically representing the geometrical complexity of several, strongly coupled free boundaries makes modeling of the HRG system extremely challenging. Indeed, there have been no prior attempts to put together the complete thermal-capillary model required for this task. To do so here, we employ two simplifying assumptions. First, we assume that the most essential interactions of the HRG process can be represented in two dimensions, as depicted by the domains comprising melt, crystal and crucible shown in Figure 2.1. In this configuration, the growth interface spreads across a shallow melt supported by a cantilever shelf that extends from the crucible, similar to the geometry employed in laboratory development at Energy Materials Research. Second, we employ an idealized picture of furnace heat transfer that, while qualitatively representative of a real system, is purposely simplified for this study. Our discussion of model development for this nonlinear, coupled, moving-boundary problem is provided below.

2.1 Field equations

To model the temperature field throughout the system, $T(x, y)$, the energy conservation equation is applied with conduction terms in all three material domains. Convection

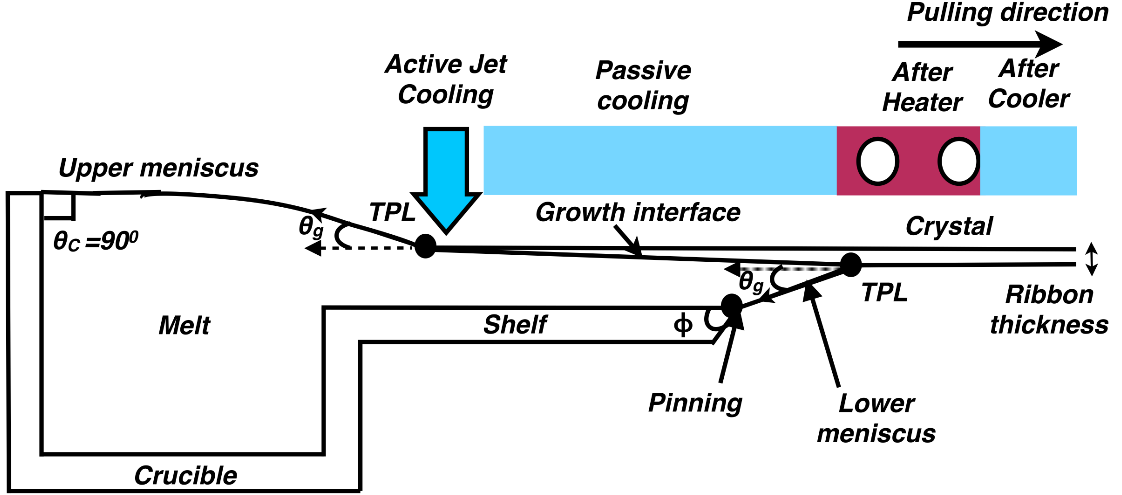

Figure 2.1: Crucible geometry and thermal boundary conditions for base case simulation of the HRG system along with illustration of growth angle, wetting angle and pinning conditions at melt–crucible junctions and at triple phase lines (TPLs).

terms in the melt and crystal domains account for fluid flow and ribbon motion, respectively.

$$\frac{\partial T}{\partial t} + \mathbf{u} \cdot \nabla T = \alpha_i \, \nabla^2 T, \; i = m, c \tag{2.1}$$

$$\frac{\partial T}{\partial t} = \alpha_i \, \nabla^2 T, \; i = d \tag{2.2}$$

The subscript i denotes the phase, with m for the melt, c for the crystal, and d for the crucible. The variable t refers to time, partial derivatives are represented by $\partial/\partial t$, and the nabla operator with $\nabla \equiv (\partial/\partial x)\mathbf{e}_x + (\partial/\partial y)\mathbf{e}_y$, where $\mathbf{e}_j$ indicates a unit vector pointing in the j-coordinate direction. The velocity field $\mathbf{u}$ is represented in the melt and crystal domains. The thermal diffusivity, $\alpha_i = k_i/\rho_i c_{pi}$ is written for each phase, where k_i is the thermal conductivity, ρ_i is the density and c_{pi} is the heat capacity.

The velocity field, $\mathbf{u}(x, y)$, and pressure field, $p(x, y)$, in the melt domain are governed

by the Navier–Stokes equations and the continuity equation, written for an incompressible fluid, to satisfy momentum and mass conservation, respectively:

$$\rho_m \frac{\partial \mathbf{u}}{\partial t} + \mathbf{u} \cdot \nabla \mathbf{u} = \nabla \cdot \mathsf{T} + \rho_m [1 + \beta_m (T_{mp} - T)]\mathbf{g}, \quad (2.3)$$

$$\nabla \cdot \mathbf{u} = 0, \quad (2.4)$$

In the above equations, T is the total stress tensor, $\mathbf{I}$ is the identity tensor, $\mathbf{g}$ is the gravity vector and μ_m is the viscosity of silicon melt. The momentum equation accounts for inertial, viscous, pressure, and gravity forces. In addition, it accounts for buoyancy forces according to the Boussinesq approximation by considering a temperature dependance of the density, $\rho = \rho_m(1 + \beta_m(T_{mp} - T))$, in the body force term of eq. (2.3). The melt density is represented by ρ_m, β_m is the thermal compressibility of the melt, and a reference temperature T_{mp} is chosen as the melting point of silicon.

Additional information is needed to specify the *a priori*-unknown positions of all moving boundaries in this problem, namely the solidification interface, the upper and lower melt menisci, and the thickness of the silicon ribbon. We discuss below the conditions that determine these moving boundaries, followed by other boundary conditions that must be supplied for the field equations to complete the specification of the mathematical model.

2.2 Solidification interface

Since the solidification interface divides the domains of melt and crystal, appropriate boundary conditions must be applied to assure the continuity of temperature and heat flux across the interface. Continuity of the temperature field is assured by setting

$$T|_m = T|_c \quad (2.5)$$

at the interface. Solidification of melt at the growth interface results in the release of latent heat at a rate proportional to crystal growth. Balancing the difference in heat

flux between melt and crystal with latent-heat yields:

$$k_m(\mathbf{n} \cdot \nabla T)|_m - k_c(\mathbf{n} \cdot \nabla T)|_c = \rho_m \Delta H_m \ \mathbf{n} \cdot (V_g \mathbf{e}_x + \dot{\mathbf{x}}), \tag{2.6}$$

where $\mathbf{n}$ is a unit vector normal to the interface, ΔH_m is the latent heat per unit of solidified mass, $\mathbf{e}_x$ is the unit coordinate vector in the horizontal direction, V_g is the horizontal pull rate, and $\dot{\mathbf{x}}$ is the rate at which the interface moves with respect to the fixed coordinates. Under quasi-steady growth conditions, the growth rate is exactly the pull rate, the interface is motionless in the coordinate frame, and $\dot{\mathbf{x}} = 0$.

Finally, the growth interface is assumed to lie along the melting-point isotherm, providing an additional constraint that serves to locate the solidification boundary. The isotherm condition is then

$$T(\mathbf{x}) = T_{mp}, \tag{2.7}$$

where $\mathbf{x}$ represents the coordinates that define the interface position and T_{mp} is the melting-point temperature. This approach is discussed in more depth by Yeckel and Derby [70] and is appropriate as long as the kinetics of phase change are sufficiently fast [71], which is usually the case for semiconductor melt growth.

2.3 Capillary interfaces

There are two melt-gas interfaces in the HRG system, labeled as the upper meniscus and lower meniscus in Figure 2.1, which are free surfaces. Forces and, consequently, the melt velocity along these free surfaces are influenced by surface tension and meniscus shape. A vector representation of the force balance across these menisci is:

$$\mathbf{n} \cdot \mathsf{T} = (-p_a + \gamma \frac{d\mathbf{t}}{ds})\mathbf{n} + (\frac{d\gamma}{dT} \ \mathbf{t} \cdot \nabla T)\mathbf{t}, \tag{2.8}$$

where the term on the left, $\mathbf{n} \cdot \mathsf{T}$, is the traction vector corresponding to forces from the melt at the interface, p_a is the ambient gas pressure, and s is the arc-length coordinate along the free surface. The surface tension, γ, and the mean curvature of the surface,

expressed as, $d\mathbf{t}/ds$, results in a normal stress acting on the free surface. The thermal variation of surface tension, $\gamma = \gamma_{mp} + (d\gamma/dT)(T - T_{mp})$, is represented in the second term on the left-hand-side of the above equation and imposes a tangential stress on the free surface which drives surface flows from low to high surface-tension regions, referred to as Marangoni flows.

The force balance above provides two conditions for momentum boundary conditions along the surface. An additional constraint is needed to specify the location of the free surfaces, namely the kinematic condition, which states that the meniscus is a material surface over which no mass escapes, leading to:

$$\mathbf{n} \cdot \mathbf{u} = \mathbf{n} \cdot \dot{\mathbf{x}}, \tag{2.9}$$

where $\mathbf{n} \cdot \mathbf{u}$ is the melt velocity normal to the surface and $\mathbf{n} \cdot \dot{\mathbf{x}}$ is the normal motion of the surface itself. Under quasi-steady conditions, the surface is motionless with respect to the fixed coordinate system and $\mathbf{n} \cdot \dot{\mathbf{x}} = 0$.

Since the mean curvature term in eq. (2.8) involves second derivatives of the free boundary shape, two additional boundary conditions, one specified at either end of both menisci, are required to complete their formulation for shape determination. At the outer end of the upper meniscus, we prescribe a wetting angle condition, specifying that the melt attain a flat surface away from the growing crystal and wet the inner crucible wall at a contact angle of $\theta_C = 90^0$. This condition does not pin the end of the meniscus, rather it allows the meniscus to float with the melt volume. Determination of the melt volume is discussed in ensuing Section 2.5. The other boundary condition for the upper melt meniscus is that it connects to the triple phase line (TPL) that is defined by the intersection of the solidification interface with the upper ribbon surface. For the lower meniscus, we simply specify endpoints that connect the melt surface to the lower crucible lip and to the TPL associated with the ribbon lower surface.

Finally, the pinning condition of the lower meniscus to the crucible merits additional discussion. Although this condition is unambiguous with respect to the mathematical

formulation of the problem, there are physical implications of this connection. Namely, when a liquid surface contacts a flat solid, it will form an equilibrium wetting angle θ_e. However, while a liquid may remain pinned at the edge at a corner, its apparent contact angle, θ_C, can differ markedly from θ_e. Such pinning arises due to the microscopic radius of curvature at the edge, which can allow a local equilibrium wetting angle to be satisfied while yielding a different macroscopic angle [72, 73]. For two solid surfaces forming a corner with a dihedral angle ϕ (see Figure 2.1), the classical Gibbs limit [74, 75, 76] states that the meniscus pinning condition is stable only when θ_C lies within the following values,

$$\theta_e < \theta_C < 180 - \phi + \theta_e. \tag{2.10}$$

Beyond these limits, the melt meniscus will either recede from or spill over the corner of the crucible.

2.4 Ribbon thickness

In the thermal-capillary formulation presented here, the thickness of the growing ribbon is computed as a part of the problem formulation. The only assumption is that we apply motion to the ribbon at a specified speed and direction, namely $V_g\mathbf{e}_x$ in the current problem specification.

The ribbon thickness is set by the positions of the triple phase lines (TPLs) of the upper and lower meniscus. Specifically, we enforce the growth angle condition at the TPL that arises from energetic considerations along each of the three intersecting surfaces, as shown in Figure 2.1. Eustathopoulos *et al.* [72] provide an excellent discussion of these issues. For the pulling direction considered here, a general equation for the vertical position of each TPL is written as

$$\frac{\partial y_i}{\partial t} = (V_g + \dot{\mathbf{x}} \cdot \mathbf{e}_x) \tan(\psi - \theta_g), \tag{2.11}$$

where y_i is the vertical coordinate of the TPL, θ_g is the growth angle, ψ is the actual

angle of attachment of the meniscus to the TPL, and the term $\dot{\mathbf{x}}\cdot\mathbf{e}_x$ denotes the transient horizontal motion of the TPL caused by movement of the solidification interface. In a transient simulation, the above conditions specify the evolving shape of the ribbon, where changes in thickness are moved away from the TPLs by solid-body translation in the pulling direction and result in a time-varying ribbon thickness.

Under conditions of quasi-steady growth, the above condition simplifies considerably to require that each meniscus attach to the crystal at the growth angle (thus assuring no change in TPL positions and a constant ribbon thickness), namely

$$\mathbf{n}\cdot\mathbf{e}_x = \sin\theta_g, \tag{2.12}$$

where $\mathbf{n}$ is the unit vector normal to the meniscus. For silicon crystals, a growth angle of $\theta_g = 11^0$ is maintained [73, 77, 64, 78].

2.5 Melt level and outlet flows

Mass conservation of the melt is specifically enforced by continuity, eq. (2.4), in conjunction with boundary conditions that specify flows normal to the boundaries. We have already specified no flows across the menisci by the kinematic condition, eq. (2.9). This condition is augmented by no-slip conditions along all solid surfaces. Along the inner crucible walls, we specify

$$\mathbf{u} = \mathbf{0}, \tag{2.13}$$

which sets the normal and tangential velocity components to zero.

However, the situation along the solidification interface is different; tangential and normal velocity conditions arising from mass conservation during phase change at the growth interface result in an effect known as solidification flow. Appropriate velocity conditions are imposed on the interface to capture these effects:

$$\mathbf{t}\cdot(\mathbf{u} - \frac{\rho_c}{\rho_m}V_g\ \mathbf{e}_x) = 0, \tag{2.14}$$

$$\mathbf{n}\cdot(\mathbf{u} - \frac{\rho_c}{\rho_m}V_g\ \mathbf{e}_x) = (1 - \frac{\rho_c}{\rho_m})\mathbf{n}\cdot\dot{\mathbf{x}}, \tag{2.15}$$

where $\dot{\mathbf{x}}$ denotes the time rate of interface movement with respect to the coordinates and $\mathbf{t}$ and $\mathbf{n}$ are unit vectors in tangential and normal directions to the interface, respectively.

Unless the melt is replenished continuously during growth, the upper meniscus position will steadily drop as the ribbon is pulled and the crucible empties. If a transient model is applied, the melt level will be determined by the initial melt volume and by mass conservation inherent in the problem formulation as stated above.

The case of continuous melt replenishment is of engineering interest, since this would allow for steady-state operation over extended periods of time. To assess this situation, we replace the no-slip conditions of eq. (2.13) with a different set of conditions along the bottom crucible inner surface. Specifically, we allow for a make-up flow that exactly counters the loss of melt material due to solidification at the interface using the following conditions:

$$\mathbf{t} \cdot \nabla \mathbf{u} = 0, \tag{2.16}$$

$$\mathbf{nn} : \mathsf{T} = -p_o, \tag{2.17}$$

where p_o, is set to attain a desired, quasi-steady melt level.

2.6 Thermal boundary conditions

The remaining boundary conditions account for heat transfer between the system and the surrounding furnace. Our current model employs relatively simple representations of applied heating and cooling, based on descriptions of prior HRG systems [14] and on configurations under development by Energy Materials Research.

Radiant heat fluxes are applied along all exterior surfaces via the Stefan-Boltzmann law:

$$k_i \ \mathbf{n} \cdot \nabla T|_i = \sigma \epsilon_i (T^4 - T_{a,j}^4), \tag{2.18}$$

where σ is the Stefan-Boltzmann constant, ϵ_i is the emissivity of surface i, and $T_{a,j}$ denotes an ambient temperature with which the surface exchanges heat. The ambient

temperatures, $T_{a,j}$, are set to qualitatively match heat transfer conditions. For example, the crucible bottom and sides are heated by a uniform temperature above the melting point of the system, the shelf of the crucible is heated by slightly hotter temperatures to provide larger gradients across the growth region and prevent lower meniscus freezing. The top surface of the melt and crystal cools to a uniform ambient temperature. Finally, an after-heater region is specified above and below the ribbon as it exits from the crucible shelf, with an ambient temperature slightly below the melting point, but significantly above the cool ambient applied elsewhere.

One important modification is made to the above heat flux conditions. Following the suggestion by Zoutendyk [67] and the description of Kudo [14], a gas jet is assumed to be positioned over the ribbon tip, and the flux condition is augmented in a thin region adjacent to the growth tip with a convective cooling term as follows,

$$k_c \; \mathbf{n} \cdot \nabla T|_c = \sigma \epsilon_c (T^4 - T_{a,t}^4) + h_c (T - T_{a,t}), \tag{2.19}$$

where $T_{a,t}$ denotes the cool ambient temperature over the top of the system and h_c is a heat transfer coefficient estimated for the cooling jet conditions described in [14].

Finally, we make the ribbon domain extend far enough out of the crucible so that it attains thermal equilibrium with the ambient temperature and its end position does not affect heat transfer near the growth region.

Chapter 3

Numerical Methods

3.1 Galerkin Finite Element discretization

The above equations governing the thermal-capillary model are posed for either a fully transient representation or as a quasi-steady model, where all time derivatives are set to zero and the appropriate inflow conditions are applied to set a melt level. We employ the Galerkin finite element method (GFEM) for the solution of these models. While referring the interested reader to several sources [79, 80, 81] for a detailed description of the method and its implementation, the essential ideas are presented here succinctly.

GFEM involves discretization of the problem domain dividing it into subdomains, known as finite elements. Here, the model geometry is discretized using nine-noded quadrilateral elements. To simplify discretization, the physical coordinates (x, y) are transformed into computational coordinates (ξ,η) using parametric mapping, as shown in 3.1, in which the quadrilateral element is mapped to a unit square parent element.

$$(x, y) = \sum_{k=1}^{N}(x^k, y^k)\phi^k(\xi, \eta), \tag{3.1}$$

where x^k, y^k are the physical nodal coordinates of the quadrilateral element, k refers to the node numbering and $\phi^k(\xi, \eta)$ are the variable-order Lagrange basis functions [80]

defined at each node k. These functions possess the convenient property that their value is equal to one at the corresponding node k and zero at all other nodes in the element.

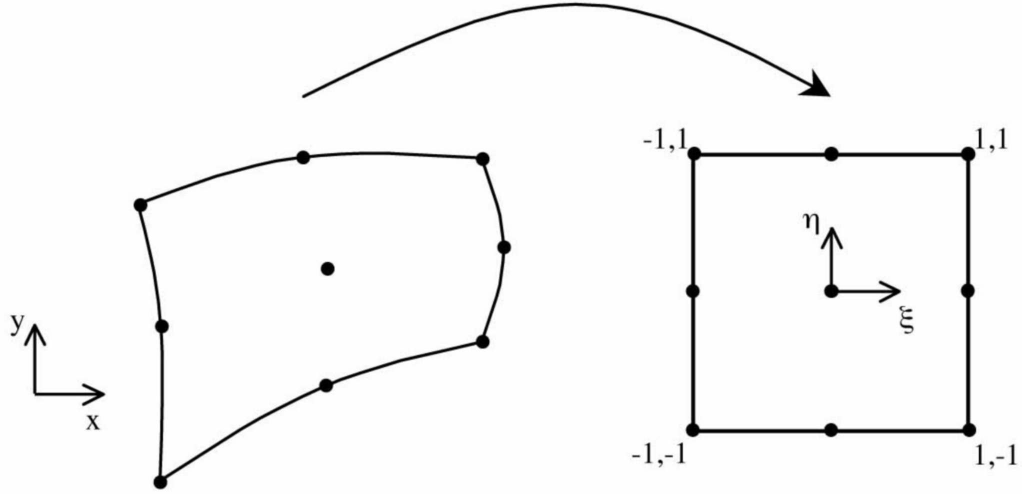

Figure 3.1: Parametric mapping to a unit square parent element [18]

To discretize the governing equations, the field variables of velocity (u), temperature (T) and pressure (p) are approximated on the parent element, again using the variable-order Lagrange basis functions(biquadratic (ϕ) for u, T and linear discontinuous (ψ) for p).

$$\begin{aligned} T = \hat{T} &= \sum_{k=1}^{N} T^k \phi_T^k(\xi, \eta) \\ u = \hat{u} &= \sum_{k=1}^{N} u^k \phi_u^k(\xi, \eta) \\ p = \hat{p} &= \sum_{k=1}^{N} p^k \psi_p^k(\xi, \eta), \end{aligned} \tag{3.2}$$

where $\hat{u}, \hat{T}$ and $\hat{p}$ refer to the approximated field variables. These are substituted into the governing partial differential equations (2.1 - 2.4), and terms are gathered on one

side to form residual equations.

$$
\begin{aligned}
\mathcal{R}_T &= \frac{\partial \hat{T}}{\partial t} + \hat{\mathbf{u}} \cdot \nabla \hat{T} - \alpha \nabla^2 \hat{T}, \\
\mathcal{R}_u &= \rho_m \frac{\partial \hat{\mathbf{u}}}{\partial t} + \hat{\mathbf{u}} \cdot \nabla \hat{\mathbf{u}} - \nabla \cdot \hat{\mathsf{T}} - \rho_m [1 + \beta_m (T_{mp} - \hat{T})] \mathbf{g} \\
\mathcal{R}_p &= \nabla \cdot \hat{\mathbf{u}} \qquad (3.3)
\end{aligned}
$$

with

$$\hat{\mathsf{T}} \equiv -\hat{p}\mathbf{I} + \mu_m (\nabla \hat{\mathbf{u}} + (\nabla \hat{\mathbf{u}})^{\mathsf{T}}). \qquad (3.4)$$

These residuals represent the error in the approximation to the differential equations and has to be made small in order to obtain an accurate solution. This is done in a weighted residual sense [82], where the residual equations are made orthogonal to basis functions over the entire domain, represented mathematically by the following equations.

$$\int_A \phi_T^i \mathcal{R}_T dA = 0, \int_A \phi_u^i \mathcal{R}_u dA = 0, \int_A \psi_p^i \mathcal{R}_p dA = 0 \qquad (3.5)$$

Here index i refers to all the nodes in the entire domain. To eliminate the second derivates of the field variables in these integro-differential equations, weak form of the weighted residuals are derived by using the chain rule of differentiation and the Gauss divergence theorem and are given below

$$\int_A \phi_T^i (\frac{\partial \hat{T}}{\partial t} + \hat{\mathbf{u}} \cdot \nabla \hat{T}) dA + \int_A \alpha \nabla \phi_T^i \cdot \nabla \hat{T} dA - \int_l \alpha \phi_T^i \mathbf{n} \cdot \nabla \hat{T} dl = 0$$

$$\int_A \phi_u^i (\rho_m \frac{\partial \hat{\mathbf{u}}}{\partial t} + \hat{\mathbf{u}} \cdot \nabla \hat{\mathbf{u}} - \rho_m [1 + \beta_m (T_{mp} - \hat{T})] \mathbf{g}) dA + \int_A \nabla \phi_u^i \cdot \hat{\mathsf{T}} dA - \int_l \phi_u^i \mathbf{n} \cdot \hat{\mathsf{T}} dl = 0,$$

$$\int_A \psi_p^i \nabla \cdot \hat{\mathbf{u}} dA = 0, \qquad (3.6)$$

where l refers to the boundary length. The area integrals in the physical real space are transformed to the parent element using the jacobian of transformation and the integrals are evaluated using 3X3 Gaussian quadrature rule [83] resulting in a set of non-linear algebraic equations.

3.2 Elliptic Mesh Generation

Due to the free and moving boundary nature of the various interfaces in the system, whose positions are unknown a priori, it is essential to parametrize the locations of the nodes. This is accomplished using elliptic mesh generation, developed by de Santos [84, 85], in which a pair of elliptic partial differential equations are used to describe the position of the nodes.

$$\begin{aligned} \nabla \cdot D_\xi(\xi,\eta)\nabla\xi &= 0 \\ \nabla \cdot D_\eta(\xi,\eta)\nabla\eta &= 0 \end{aligned} \tag{3.7}$$

The principle behind the method can be best explained using a thermal problem analogy where the two families of mesh lines ξ and η correspond to the iso-temperature lines of ξ and η in a pure conduction problem governed by the Laplace equations $\nabla^2\xi = 0$ and $\nabla^2\eta = 0$ respectively. The temperature field, ξ, has adiabatic condition, i.e. $\partial_n\xi = 0$, on two sides (say east and west) and a constant temperature of $\xi = 1$ and $\xi = 0$ on the other two sides (say north and south respectively) and similarly for the co-temperature field, η, except the boundary conditions on the sides are swapped. Owing to the properties of the solution of the Laplace equation, the two families of the mesh lines are bound to have a unique solution with maxima occurring only on the element boundaries, with iso-lines staying inside the domain and no intersection between the iso-lines, together giving rise to a distribution of structured quadrilateral elements throughout the domain.

The pair of diffusion coefficients, D_ξ and D_η, control the element size distribution in the domain, with constant diffusivity values generating a mesh of approximately equal element sizes. These values should vary exponentially from element to element in order to obtain stretching of the mesh, however, their values are calculated from just the initial mesh generated by the algebraic method. These mesh equations are coupled to the free and moving boundary conditions imposed by the physics, governing the evolution of the internal mesh while conforming to these boundaries and preserving the initial mesh characteristics.

For GFEM implementation, the governing mesh equations are again written in the weak-form of the weighted residuals as shown in Eq. 3.8, similar to the procedure adapted before. However, these equations are written in terms of the computational variables, ξ and η, and need to be transformed into the real space variables, x and y, by invoking the relationships between parametric mapping.

$$
\begin{aligned}
\int_A D_\xi \nabla\phi^i \cdot \nabla\xi dA - \int_l \phi^i D_\xi \mathbf{n} \cdot \nabla\xi dl = 0 \\
\int_A D_\eta \nabla\phi^i \cdot \nabla\eta dA - \int_l \phi^i D_\eta \mathbf{n} \cdot \nabla\eta dl = 0
\end{aligned}
\tag{3.8}
$$

The adaptation of such a mesh generation technique, however, introduces a complication with respect to how time derivates are evaluated. Note that the time derivates of the field variables in the governing equations are taken with respect to the Eulerian (or laboratory) frame of reference, whereas time derivates of the basis functions in the residual equations must be computed with respect to the reference frame fixed with the parent element. Therefore, the time derivates in the discretized equations must be converted from the Eulerean frame to the parent element frame:

$$\begin{aligned} \frac{\partial \hat{\mathbf{u}}}{\partial t} &= \dot{\mathbf{u}} - \dot{\mathbf{x}} \cdot \nabla \hat{\mathbf{u}} \\ \frac{\partial \hat{T}}{\partial t} &= \dot{T} - \dot{\mathbf{x}} \cdot \nabla \hat{T} \end{aligned} \tag{3.9}$$

where the overdot indicates time derivates with respect to the parent element frame which is analogous to the material derivate of the Reynolds transport theorem.

3.3 Boundary Conditions

The various boundary conditions considered in the model can be broadly classified into the following types: Dirichlet condition where the value of the field variable is specified at the boundary; Neumann condition where the derivative of the field variable is specified; and Robin condition where a linear combination of the field variable and its derivates are specified. Dirichlet condition, also referred to as an essential boundary condition in a finite element context, is imposed by replacing the residual of the conservation equation at the specified boundary. The Neumann and Robin conditions are referred to as natural boundary conditions as they appear naturally in the boundary integral of the weak-form of the residual, as $\mathbf{n} \cdot \nabla T$ in the energy residual and $\mathbf{n} \cdot \mathsf{T}$ in the momentum residual. These conditions are imposed by simply replacing the integrand in the boundary integral of the residuals with a specified value or a computable expression.

3.4 Solution Methods

These discretized equations result in a residual vector, $\mathbf{r}(\mathbf{z}, \dot{(\mathbf{z})}, \mathbf{p}) = 0$, where $\mathbf{z}$ is a vector of the nodal values of the field variables and and $\mathbf{p}$ denotes a vector of input parameters. For quasi-steady problems, $\dot{\mathbf{z}} = 0$ and $\mathbf{r}(\mathbf{z}, \mathbf{p}) = 0$, is a set of non-linear algebraic residual equations in $\mathbf{z}$ and are solved by Newton's method iteratively, where

the non-linear residuals are linearized about the solution vector, $\mathbf{z}^k$:

$$\mathbf{J}(\mathbf{z}^k, p)\delta^{(k+1)} = -\mathbf{r}(\mathbf{z}^k, p) \tag{3.10}$$

where k denotes the iteration count. The Jacobian matrix, $\mathbf{J}(\mathbf{z}^k, p)$, is defined as:

$$\mathbf{J}_{ij} = \frac{\partial \mathbf{r}_i}{\partial \mathbf{z}_j} \tag{3.11}$$

where the subscripts i and j denote row and column indices respectively ($\mathbf{r}_i$ is the ith component of vector $\mathbf{r}$ and $\mathbf{z}_j$ is the jth component of vector $\mathbf{z}$). The solution update vector, $\delta^{(k+1)}$, is defined by

$$\mathbf{z}^{(k+1)} = \mathbf{z}^{(k)} + \delta^{(k+1)} \tag{3.12}$$

The linearized matrix problem in Equation 3.10 is then put into LU-decomposition form using a direct solver method called the frontal solver developed by Hood [86]. Here, the Jacobian matrix, $\mathbf{J}$, is never completely assembled but instead its entries are computed finite element by finite element and summed into an array called the frontal matrix. This is allowed due to the sparse nature of the Jacobian matrix, $\mathbf{J}$, that results from the orthogonal nature of the basis functions and their derivates. Summation of each equation is complete when all finite elements that contribute to it have been assembled. Completely summed equations are eligible for immediate elimination from the frontal matrix, with the results stored in arrays representing the LU factors.

Starting from an initial guess, the Newton iterations continue until the L2 norm of the residual vector and the solution update vector are both less than 10^{-4} times the L2 norm of the solution vector. Since a prudent initial guess for such a non-linear problem with moving boundaries can be challenging, it is often difficult to obtain a converged solution using Newtons scheme. Under such circumstances, a damping (under-relaxation) factor of less than one is often beneficial during the iterations to obtain convergence. A

modified Newton iteration scheme is also employed appropriately, to reduce computational effort, where the Jacobian, **J**, is reused for several consecutive steps before it is refactorized.

For transient problems, third-order explicit Adams-Bashforth predictor and an implicit trapezoid rule corrector with variable time step is used to integrate the equations in time. The resulting time-dependent residuals are again non-linear algebraic equations and are solved by an iterative Newton's method similar to that applied to the quasi-steady problems.

Parameter continuation of steady states, with converged solution at parameter P acting as a good initial guess for the system at P+δP in zeroth order continuation, is conducted to study parametric sensitivity. First order continuation provides an even more prudent initial guess at P+δP, given a solution and its factorized Jacobian, **J**, at parameter value P, by estimating the first-order sensitivity of the solution vector with the parameter P. Arc-length continuation [87, 88] is used to track turning point singularities and bifurcations in the system behavior, by mapping the process parameter, P, onto a new parameter, L, that characterizes arc-length along the solution curve. Since arc-length has to monotonically increase along the solution curve, whereas P may or may not, turning points can be crossed by simply continuing in L instead of P. Parameter tracking allows for inverse formulation of the problem where it is possible to track the value of a parameter such that the desired physical constraint is satisfied. For example, a desired crystal thickness can be specified and the required pull-rate can be computed as part of the solution.

All the above mentioned numerical procedures are implemented using the Cats2D (Crystallization and transport simulator 2D) software developed at the University of Minnesota. An extensive description of this code is presented in [18].

Chapter 4

Thermal-Capillary Analysis

Simulations are performed for a model geometry with a graphite crucible that is taken to be 1 cm long with a wall thickness of 1 mm. The cantilever shelf extends laterally from the side of the crucible over a length of approximately 1.5 cm. For the quasi-steady cases considered here, we set inflow conditions to maintain a melt depth of 0.76 cm. The after-heater length is assumed to be 2 cm, and the width of cooling jet at the ribbon tip is 1.6 mm. These dimensions are representative of the Bleil's HRG system at Energy Materials Research. The crystal is pulled in the positive x-direction and its length is made sufficiently long enough($\sim$ 9 cm) to not affect calculations near the growth-interface, by allowing its far-end to attain thermal equilibrium with the ambient temperature. More details of the furnace heat transfer conditions used here and the materials properties of silicon are listed in Table 4.2.

A mesh, shown in Fig. 4.1, comprising of 8,580 elements was employed for all calculations presented here, giving rise to a total of 127,557 unknowns. The mesh was refined near the interfacial regions to more accurately represent the coupled, nonlinear phenomena exhibited there. Mesh refinement was undertaken to ensure that the results shown here are accurate and nearly independent of the mesh, as shown in Table 4.1.

Table 4.1: Sensitivity of results to the mesh size

Description	Mesh I	Mesh II	Error
Elements	8580	46242	
Ribbon thickness (μm)	681.72	683.82	0.31%
Average T (K)	1533.56	1533.02	0.03%
Average U (m/s)	1.223E-2	1.225E-2	0.14%
Average V (m/s)	0.183E-2	0.184E-2	0.48%

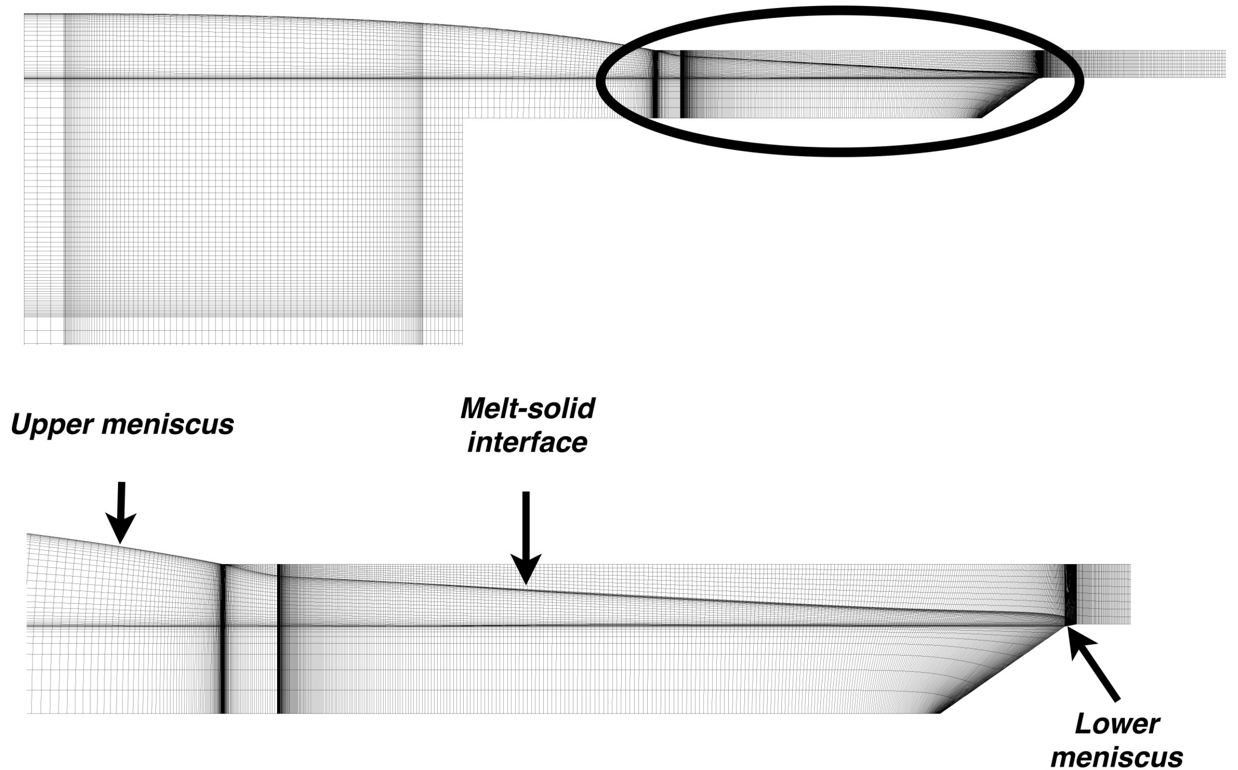

Figure 4.1: Top: Meshing scheme in the whole domain (The crystal extends beyond what is shown in the figure). Bottom: An enlarged view near the solidification interface showing stretching of the mesh near the free and moving boundaries(bottom)

Table 4.2: Furnace heat transfer parameters and material properties used in all calculations performed here.

Description (units)	Material	Symbol	Value
Ambient temperature (K)	Crucible heating	$T_{a,d}$	1747
	Shelf heating	$T_{a,s}$	1806
	Lower meniscus heating	$T_{a,e}$	2019
	Upper cooling	$T_{a,c}$	336
	After-heater	$T_{a,ah}$	1620
	After-cooler	$T_{a,ac}$	336
Conductivity (W $m^{-1}K^{-1}$)	Silicon melt	k_m	64
	Silicon crystal	k_c	22
	Gaphite crucible	k_d	43
Density (kg m^{-3})	Silicon melt	ρ_m	2420
	Silicon crystal	ρ_c	2300
Emissivity	Silicon melt	ϵ_m	0.27
	Silicon crystal	ϵ_c	0.64
	Graphite crucible	ϵ_d	0.85
Equilibrium wetting angle (deg)	Silicon melt on graphite	θ_e	30
Growth angle (deg)	Silicon	θ_g	11
Heat capacity (J $kg^{-1}K^{-1}$)	Silicon melt	$C_{p,m}$	1000
	Silicon crystal	$C_{p,c}$	1000
	Graphite crucible	$C_{p,d}$	1700
Heat of fusion (J kg^{-1})	Silicon	ΔH_f	1.8×10^6
Heat transfer coefficient (W $m^{-2}K^{-1}$)	Argon cooling jet	h_c	0.37
Melting temperature (K)	Silicon	T_{mp}	1683
Surface tension (N m^{-1})	Silicon melt	γ_{mp}	0.72
Surface tension gradient (N $m^{-1}K^{-1}$)	Silicon melt	$d\gamma/dT$	-2.19×10^{-4}
Thermal expansivity (K^{-1})	Silicon melt	β	1×10^{-4}
Viscosity (kg $m^{-1}s^{-1}$)	Silicon melt	μ	1.02×10^{-3}

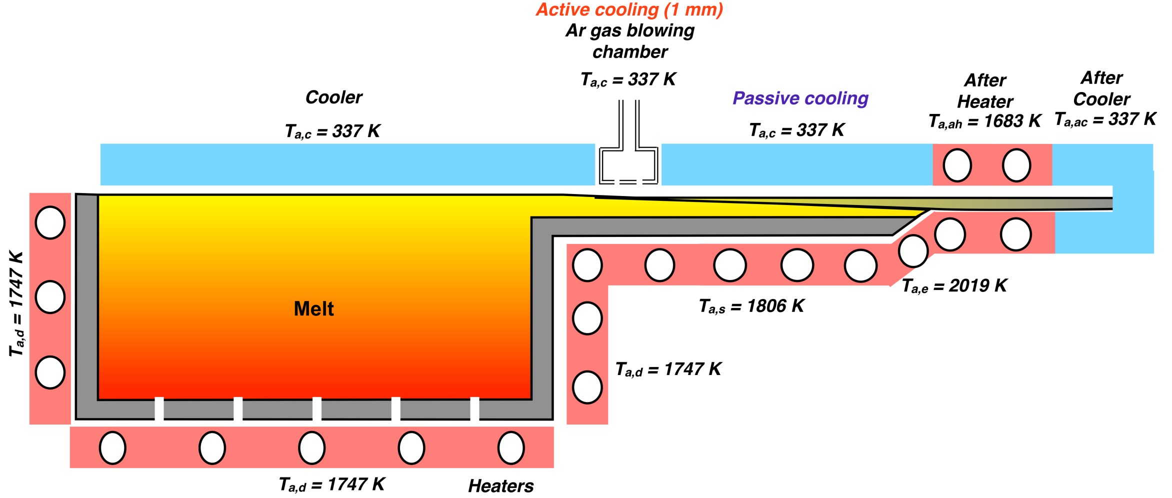

Figure 4.2: Schematic of the heating and cooling arrangements in the HRG system. Notation corresponds to the description in Table 4.2

4.1 Quasi-steady base case

A quasi-steady, base-case computation was performed using the parameters and properties described above, and the system geometry and temperature field are shown in Figure 4.3. With an applied pull rate of $V_g = 4.4$ cm/min, the model predicts a crystal ribbon thickness of $t = 674$ μm.

4.1.1 Thermal field

The overall thermal field is depicted in Figure 4.3a, which shows isotherms spaced at $\Delta T = 0.95$ K through the crucible and melt. A maximum temperature of 1702 K occurs at the heated crucible bottom, and the temperature gets progressively cooler toward the top surface. The melt cools even more toward the crucible cantilevered shelf, where the ribbon solidifies at 1683 K.

The highlighted region of Figure 4.3a is enlarged in Figure 4.3b to display isotherms plotted at $\Delta T = 1.1$ K through the crucible, melt, and crystal. Over much of the

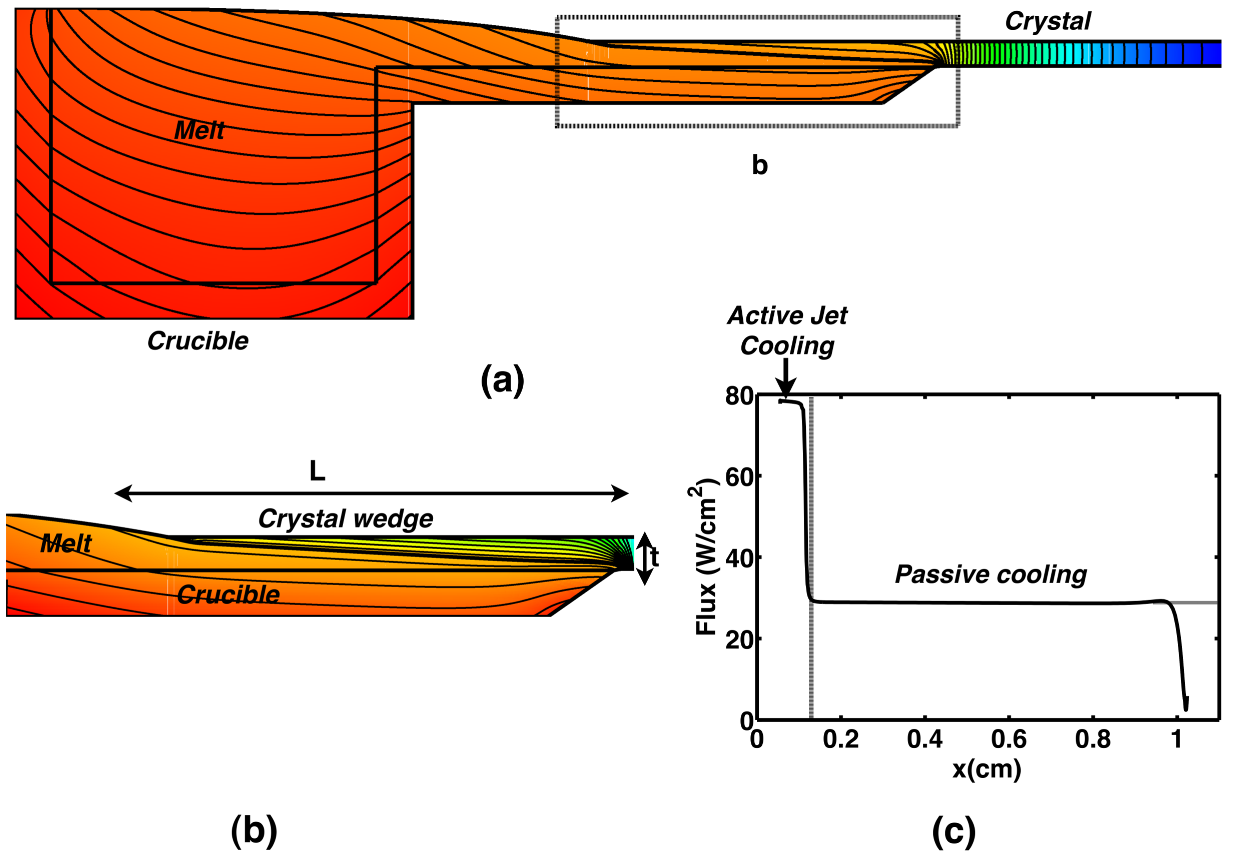

Figure 4.3: (a) Temperature field in the melt and crucible domains with T_{max} = 1702 K at the crucible bottom and T_{min} =1683 K at the growth interface. In color, higher temperatures are red and cooler temperatures are blue. Isotherm contour spacing is ΔT = 0.95 K. (b) Enlarged view near the growth interface with T_{max} = 1688 K at the bottom of crucible shelf and T_{min} =1672.5 K at the crystal edge after it exits the growth wedge region. Contour spacing is ΔT =1.1 K. (c) Heat-flux from top surface of the crystal in the growth wedge region with $\mathcal{F}_{max}$ = 75 W/cm^2 in the active cooling region and $\mathcal{F}_{min}$ = 22 W/cm^2 in the passive cooling region

growing ribbon, the solid-liquid interface is nearly straight, forming an extended, wedge-shaped crystal that is very similar to that originally assumed by Zoutendyk [19]. In this base case, the interface spans a horizontal length of $L = 0.97$ cm, forming an average wedge angle of approximately 4° and a wedge factor, $(L/t) \approx 14.4$. The wedge factor, defined as the ratio of solidification interface length (L) to the crystal thickness (t), is a measure of the interfacial area available for dissipation of the latent heat of solidification. Larger wedge factors are associated with faster growth rates and indicate the design advantage that HRG processes hold over vertical growth processes where the interface length is always approximately equal to the crystal thickness and $(L/t) \approx 1$.

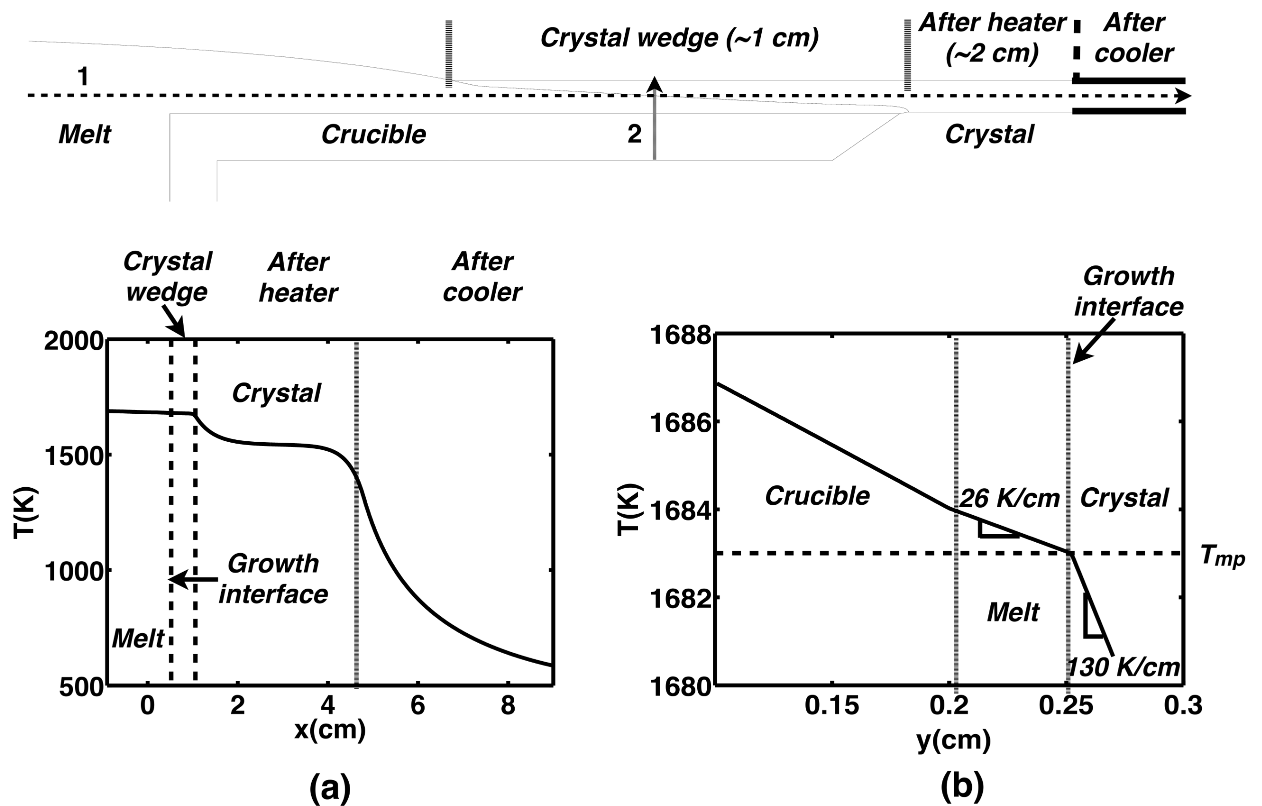

Figure 4.4: For the base case simulation at $V_g = 4.4$ cm/min, temperature versus distance: (a) along line 1, showing horizontal thermal profile and (b) along line 2, showing vertical thermal profile.

The isotherm contours in Figure 4.3b are densely packed in the crystal wedge and are aligned parallel with the interface over most of the growth region. This indicates a strong heat flux that is almost perpendicular to the pull direction. This cooling pattern withdraws more than 99% of latent heat upward through the crystal wedge, with less than 1% flowing horizontally along the ribbon growth direction. Note also the significant cooling of the growth tip via the gas jet directed at the ribbon tip. Consistent with the speculation of Zoutendyk [67], our calculations indicate that this additional cooling is needed to obtain an extended wedge shape for the growing crystal. Finally, returning to the temperature field in the crystal ribbon just beyond the crucible edge, visualized in the rightmost part of Figure 4.3b, there is no longer a growth interface generating latent heat, and the temperature field is quite one-dimensional, rearranging itself to vary primarily in the lateral direction.

Estimates of thermal gradients are obtained by plotting the temperature along horizontal and vertical cuts through the system in Figures 4.4a and b, respectively. Temperature is plotted along line 1 in Figure 4.4a, showing a very small horizontal gradient of approximately 1.15 K/cm through the melt and approximately 7 K/cm through the crystal near the growth interface. Horizontal gradients increase to as high as 240 K/cm as the crystal enters the after-heater region but soon decreases to values close to zero due to the effect of the after heater. The long cool-down of the sheet to ambient is evident as it is pulled away from the after-heater. Similarly, temperature is plotted vertically along line 2 in Figure 4.4b. Changes in slope are observed at the crucible-melt surface due to changes in thermal conductivity and at the melt-solid interface due to conductivity changes and the release of latent heat of solidification. Notably, vertical thermal gradients are found to be approximately 26 K/cm in the melt and 130 K/cm in the crystal, much larger than gradients in the horizontal direction.

4.1.2 Velocity field and menisci

Details of the velocity field in the melt and the shapes of the upper and lower menisci are featured in Figure 4.5. Marangoni forces, arising via surface tension variation with temperature, generate strong surface forces along the upper meniscus. These forces drive flows with velocities as large as 4.2 m/min (7 cm/s) from the hotter melt near the crucible on the left side of the domain toward the cooler melt adjacent to the solidifying crystal tip. Continuity and buoyancy forces in the bulk turn this flow to produce a clockwise vortex of considerable strength in the upper portion of the melt. Another vortex spins underneath, moving in a counter-clockwise direction with approximately half the strength of the upper vortex. The termination of one streamline at the bottom surface of the crucible is evidence of the make-up flow into the melt, artificially supplied through the bottom of the crucible to maintain a constant melt level in this quasi-steady simulation.

Figures 4.5b, c, and d show close-up views of the flow field and geometry. In particular, the solidification flow pattern, driven by the horizontal motion of the ribbon, is shown in Figure 4.5c. The velocity of this flow matches with the ribbon pulling speed, after density correction, to preserve mass during phase change. Figure 4.5d indicates the presence of another counter-clockwise vortex driven by Marangoni forces along the lower meniscus, though this flow is an order of magnitude weaker than that driven along the upper meniscus due to the very short meniscus length and smaller thermal gradients.

Of particular interest are the shapes of the menisci computed for this system. The upper meniscus is relatively flat over much of the melt in the crucible, owing to the effects of gravity, as shown in Figure 4.5a. However, its shape clearly curves downward toward the ribbon tip in order to satisfy the growth angle criterion, namely that the meniscus surface and the solid surface must form an angle of $\theta_g = 11^\circ$ at the triple phase line (see Figure 4.5b). The shape of the lower meniscus is shown in Figure 4.5d,

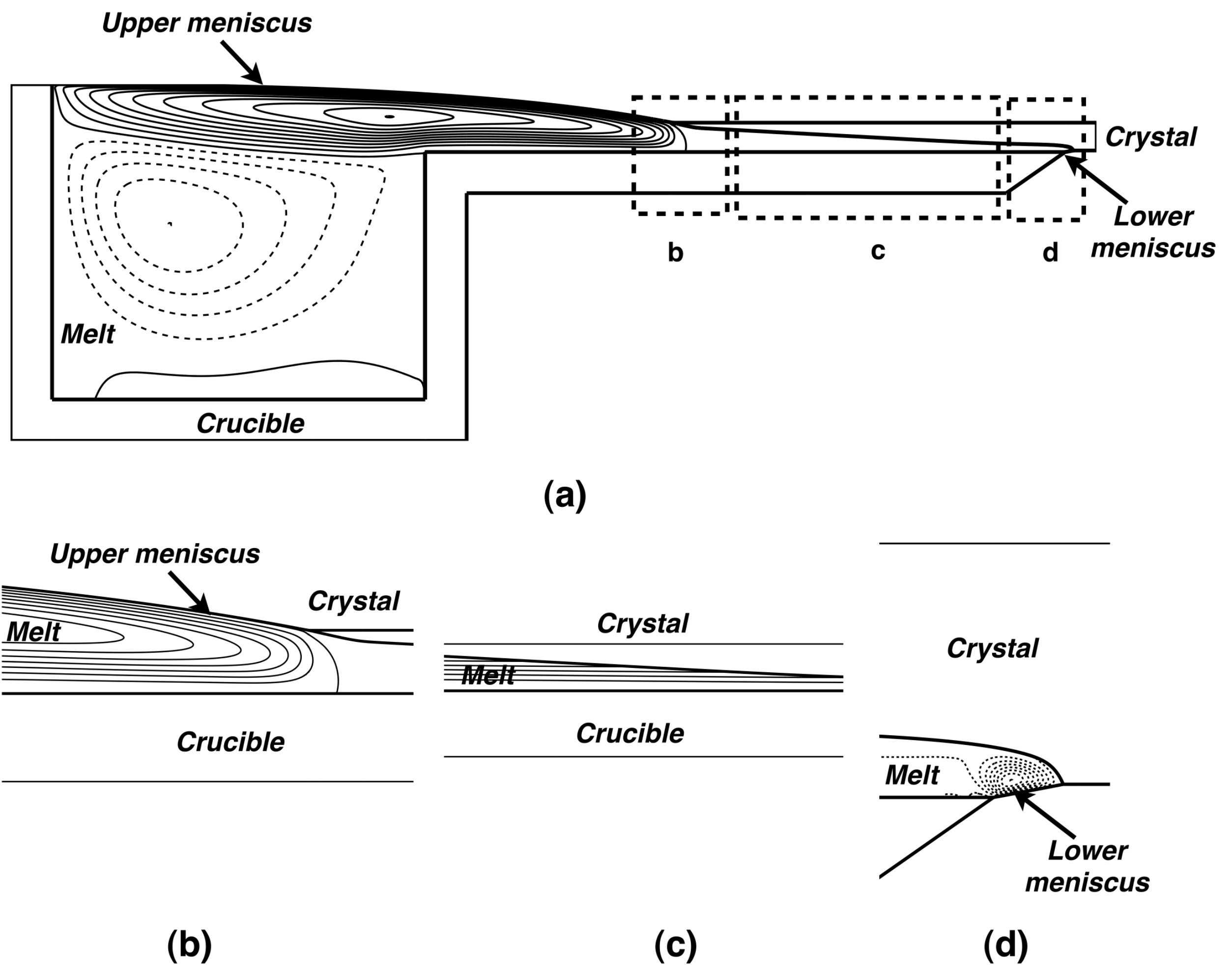

Figure 4.5: Stream function contours in the melt domain with a flow rate of 1.72 mm^2/s between consecutive streamlines. Solid and dashed streamlines indicate vortices turning in the clockwise and counter-clockwise directions, respectively. Enlarged views: (b) near the ribbon tip, flow rate between streamlines is 1.75 mm^2/s; (c) near growth interface, flow rate between streamlines is 0.056 mm^2/s; and (d) near exit meniscus, flow rate between streamlines is 0.051 mm^2/s.

which is nearly straight and quite short, approximately 0.2 mm, under the base-case operating conditions. This meniscus also connects to the lower surface of the growing crystal at the specified growth angle of $\theta_g = 11°$. The lower meniscus warrants special attention, since it must support the weight of the melt drawn over the lip of the crucible via surface tension, and it must remain pinned to the crucible edge, as specified by the Gibbs criterion, eq. (2.10). To accommodate a larger range of pinning angles, we have prescribed a crucible corner with with a dihedral angle of $\phi = 35°$ in our base-case configuration. Pinning is examined in more detail as a failure mechanism during HRG in the next chapter on stability analysis.

4.2 Pull rate limitations

One of the primary motivations for the HRG process is its potential for achieving much faster growth rates than vertical ribbon-growth methods. Here, we examine the behavior of our model for changes in the pulling rate, keeping all other parameters the same as used in the base-case computations of the prior section.

4.2.1 Pull rate, ribbon thickness, and solution multiplicity

Higher pull rates result in greater rates of latent heat release at the growth interface. This alters the thermal field in the system, affecting the interfacial shapes and reducing crystal thickness. The solid curve of Figure 4.6a shows the ribbon thickness, t, as a function of pull rate, V_g. As the pull rate is increased from 4 cm/min to 6.9 cm/min, the ribbon thickness decreases from 698 μm to 378 μm. The dashed curve of Figure 4.6 plots the relationship between pull rate and ribbon thickness derived in early analyses of ribbon growth [89, 14, 19].

$$V_g = \gamma^*(L/t), \tag{4.1}$$

where $\gamma^* = (k_c G_c - k_m G_m)/\rho_c \Delta H_f$ includes G_c and G_m, the gradients in the crystal and melt at the solidification interface, respectively. This relationship is simply the heat

flux balance, Eq. 2.6, integrated over the interface under assumed conditions of constant thermal gradients. We have positioned the dashed curve by plotting the V_g relationship of Eq. 4.1, matching it to our base-case model results (with $V_g = 4.4$ cm/min and a t =674 μm). This simple relationship is in qualitative agreement with our detailed model results, reinforcing the notion that the dominant effects in determining ribbon thickness arise from geometry and latent heat.

However, there is a significant difference between these two curves of ribbon thickness versus pull rate. Zoutendyk's analysis implies that the relationship between crystal thickness and pull rate should hold for all values of pull rate, yet this behavior is not predicted by our numerical model. Namely, the solid curve in Figure 4.6a terminates at maximum pull rate of approximately 6.9 cm/min. This behavior becomes clearer when other measures of the system are plotted as functions of pull rate. Figures 4.6b and c plot growth interface length, L, wedge factor, L/t, and lower meniscus length as the pull rate is varied. From these curves it is clear that the system exhibits a limit point at $V_g = 6.9$ cm/min and that there are multiple solutions at pull rates lower than this.

The existence of such limiting pull rates and multiple solution branches has been reported for other meniscus-defined crystal growth systems as well, such as the EFG process [90, 91, 92, 93], Czochralski growth [94, 95, 96], and the micro-pull-down method [97]. The physical origin of the limit points in these systems is attributed to the interaction among interface shapes and latent heat generation. For example, in the HRG system considered here, increases in the pull rate extend the growth interface length while simultaneously decreasing the crystal thickness, thus elevating the wedge factor and generating higher interfacial area to compensate for the greater latent heat release. However, these changes in geometry cannot indefinitely be sustained and a limit point arises. Consider the two states labeled as P1 and P2 in Figure 4.6c. Each state is a valid solution to the quasi-steady thermal-capillary model for a pull rate of $V_g = 5$ cm/min. However, as indicated by the system geometries shown in Figure 4.6d, the two states exhibit very different geometries. While both systems have very similar crystal

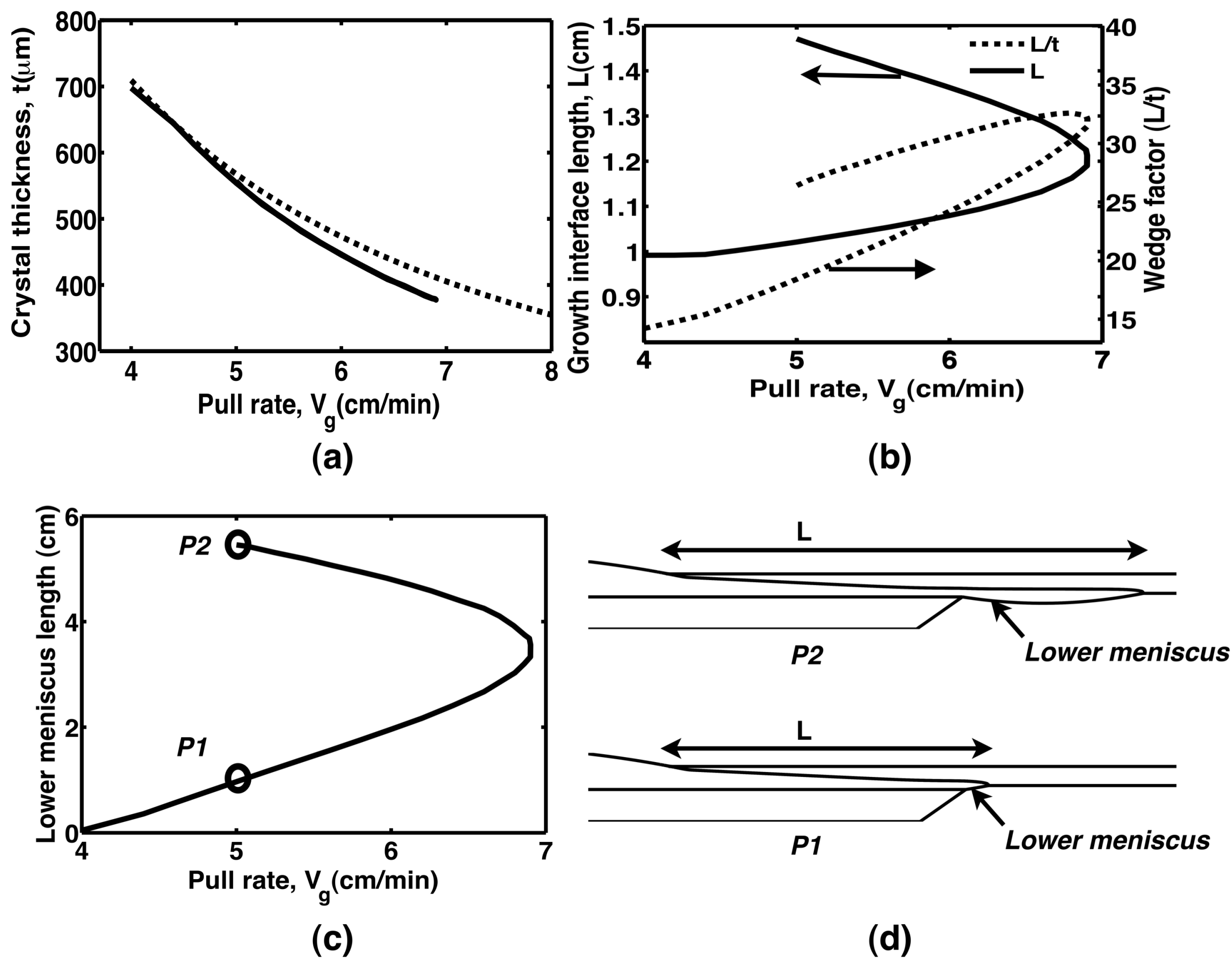

Figure 4.6: (a) Crystal thickness plotted as a function of pull-rate and compared with the prediction from idealized heat transfer analysis of Zoutendyk [19]. (b) Bifurcation into multiple branches presented in projections of growth interface length and wedge factor plotted as a function of pull rate. (c) Bifurcation plot in the projection of lower meniscus length versus pull rate. (d) Enlarged view near the growth interface for $P1$ and $P2$ showing the contrasting interfacial shapes.

thicknesses, the solution on the upper branch has an extended wedge length, L, and an exaggerated lower meniscus length.

4.2.2 Stability

The limit point and multiple solution branches discussed above typify classical bifurcation behavior arising from nonlinear interactions and have important physical implications. First, we expect that one branch of the computed quasi-steady solutions will be temporally stable and that the other will be unstable. For solutions that are temporally stable, small perturbations will be damped and the system will naturally return to the quasi-steady state. Perturbations to states on the unstable solution branch will drive the system away from them. Thus, only the stable branch represents operating states that are readily achieved and maintained during operation. Second, perhaps even more importantly, the limit point represents the maximum feasible pull rate attainable for this system; there are no stable operating states for higher pull rates. However, we will demonstrate, in calculations described in the next section, that this limit point can be shifted to larger values for different system designs.

The temporal stability of our quasi-steady solutions can be determined by performing transient simulations using the time-dependent formulation of the thermal-capillary model (including replenishment to keep the melt level constant in the crucible). The solutions on the lower branch of Figure 4.6c are probed via two simulations that employ the quasi-steady solution at a pull rate of $V_g = 4$ cm/min as an initial condition. The change of ribbon thickness with respect to time is plotted in Figure 4.7a for these two cases, one with a step increase in pull rate of $V_g = 4.2$ cm/min applied initially and another with a step change to $V_g = 5$ cm/min. Both cases show the system settling into new, quasi-steady states after about a minute of operation time. These new states also match the crystal thicknesses, 670 μm and 520 μm, predicted from quasi-steady-state analysis for the corresponding new pull rates of $V_g = 4.2$ cm/min and $V_g = 5$ cm/min. This confirms that the lower branch comprises solutions that are temporally stable.

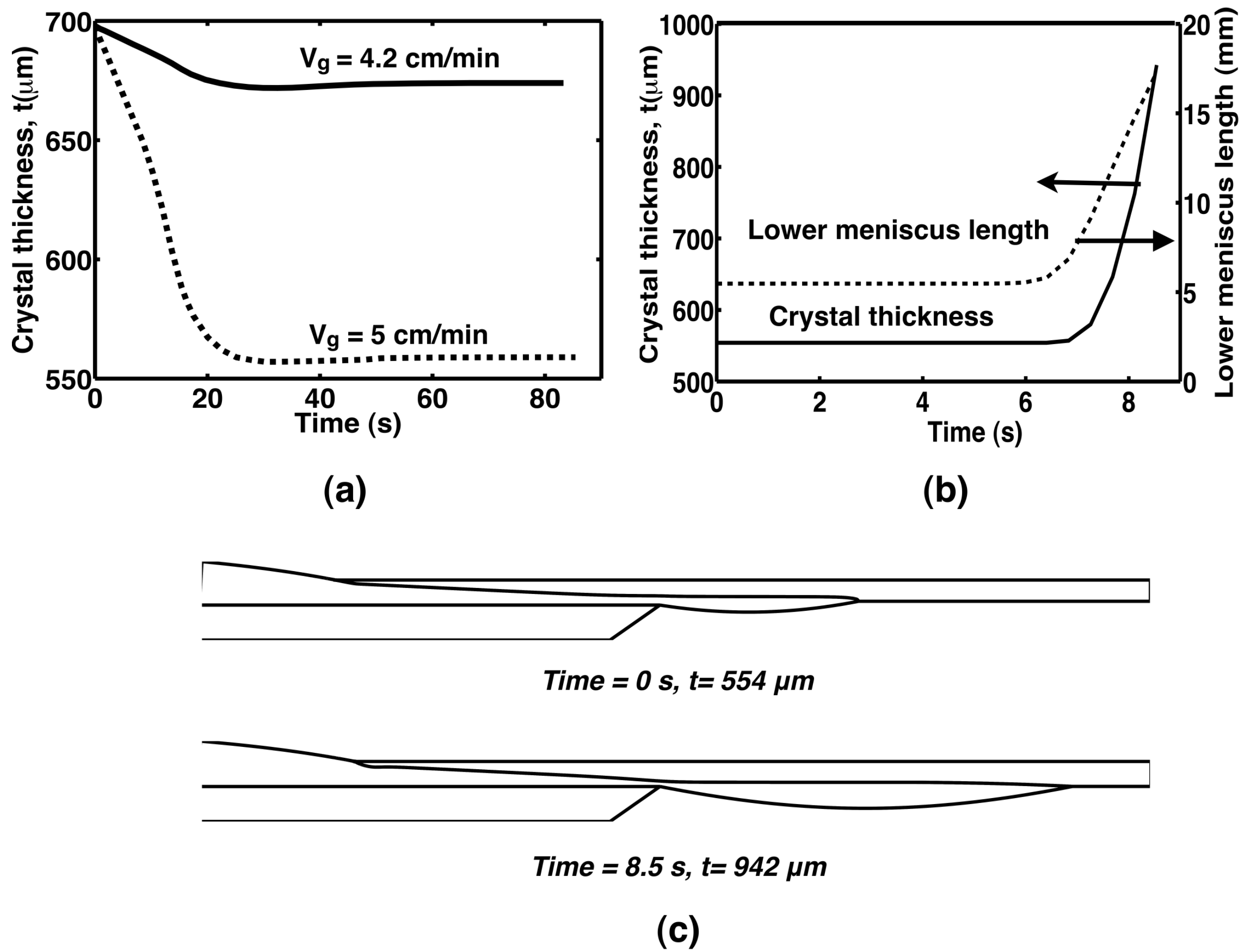

Figure 4.7: (a) Time evolution of states on lower solution branch of prior figure after a step disturbance in pull rate at time $t = 0$. (b) Time integration of state $P2$ on upper solution branch of prior figure, without any initial perturbation. (c) Enlarged view near the growth interface during the evolution of simulation starting with state $P2$ on upper solution branch at $t = 0$ and $t = 8.5$ s.

A transient analysis is also performed for the other quasi-steady solution P2, at $V_g = 5$ cm/min, on the upper branch of Figure 4.6c. For this simulation, the state $P2$ is applied as an initial condition, and time integration is carried without forcing any disturbance on the system. The simulation results plotted in Figure 4.7b indicate that the system deviates from its state after just a few seconds of operation time (here, round-off error provides a perturbation to the system). The crystal thickness and lower meniscus length undergo a steep increase until the simulation fails. The interfacial shapes shown in Figure 4.7c suggest a break-down of the lower meniscus, resulting in spilling over of the melt from the crucible as a failure mode and demonstrating that the upper branch states are unstable.

4.3 Achieving higher pull rates

The postulated base case discussed above exhibited a growth rate limit of 6.9 cm/min, a value far lower than has been reported for HRG systems in practice. Here, we investigate how system design can affect the ability to achieve faster growth rates.

The key idea behind HRG and high growth rates is achieving a very large melt-solid interface area to dissipate the latent heat of solidification. In our two-dimensional consideration of the HRG system, interface area is directly proportional to the wedge factor, (L/t). The system design considered thus far produces a solidification interface length of approximately $L = 1$ cm with ribbon thickness of order $t = 500$ μm, yielding a wedge factor of $(L/t) \approx 20$. In contrast, Kudo [14] experimentally demonstrated polycrystalline silicon growth rates of up to 85 cm/min with a crystal thickness of 200 μm. The solidification interface was spread over a length of 12 cm, forming a wedge factor of $(L/t) \approx 600$.

To extend the solidification interfacial area further in our system, we elongated the cantilevered shelf of the crucible while keeping all other parameters constant. The crystal thickness computed for these systems is plotted as a function of pull rate in

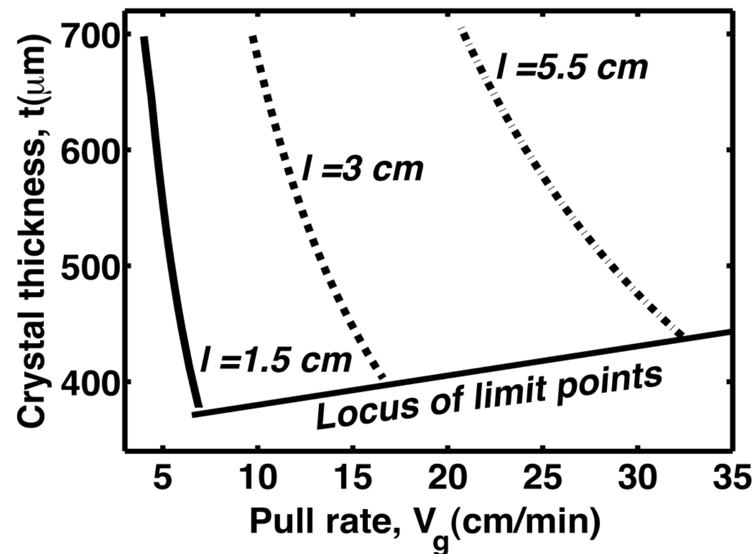

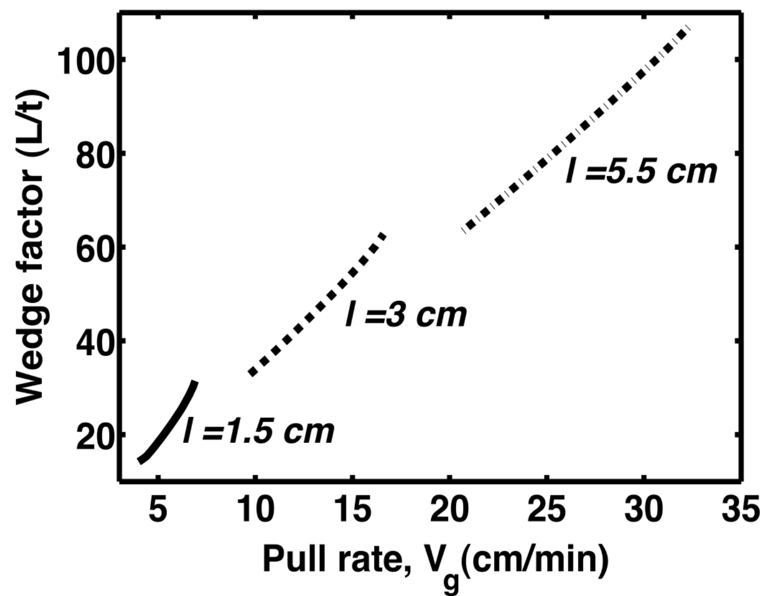

Figure 4.8: (a) Crystal thickness plotted as a function of pull rate for three different crucible cantilever shelf lengths. (b) Wedge factor versus pull rate for the three different cases.

Figure 4.8a, where the behavior of the base-case configuration of shelf length, $l = 1.5$ cm, is compared with two additional configurations with shelf lengths of $l = 3$ cm and 5.5 cm. Quasi-steady operating states from only the stable branches of the solution curves are displayed. Each curve shows a decrease in ribbon thickness with increasing pull rate; however, the new configurations with extended interfaces are able to reach pull rates as high as $V_g = 16.6$ cm/min for $l = 3$ cm and $V_g = 32.4$ cm/min for $l = 5.5$ cm. The locus of limit points depicted in Figure 4.8a represents the maximum pull rates attainable in this system as the shelf length is extended. Figure 4.8b shows the wedge factors for these systems as pull rate is varied. For the longer shelf lengths, the wedge factor varies almost linearly with pull rate, consistent with the scaling predicted by eq. (4.1) of Zoutendyk [19].

4.4 Conclusions

We have presented the development of a mathematical model of the HRG system that rigorously couples heat transfer, fluid flow, and interfacial phenomena associated with capillarity and crystal growth, and, for the first time, have successfully solved this model via a finite element method. This thermal-capillary analysis is applied to assess growth behavior as a function of system geometry and applied pull rate.

Our base-case simulation shows many of the salient features of the HRG system. For example, achieving horizontal growth with an extended solidification interface requires a heat transfer environment achieved in this system by the combination of active cooling at the solidifying tip, a cantilevered crucible shelf extension, and an after-heater. This combination produces conditions favoring the dissipation of latent heat from the interface primarily in the vertical direction, perpendicular to the pulling direction of the ribbon. Compared to the vertical EFG process [50], which is typically limited to growth rates of 2–3 cm/min and operates under thermal gradients as high as 500–1,000 K/cm, the HRG system modeled here achieves substantially faster growth rates under

lower thermal gradients, thus showing the promise of this approach.

Our base-case simulation also reveals the presence of strong flows, driven primarily by Marangoni forces, along the upper meniscus. Owing to the small crucible size considered here, buoyancy-driven flows are rather weak, and, overall, convection does not strongly affect heat transfer through the melt. The upper and lower meniscus shapes were shaped by surface tension, gravity, and the requisite growth angle at the triple phase line (TPL). To meet these requirements, the mean level of the upper meniscus lies slightly above the ribbon and curves downward to meet it at the TPL. The lower meniscus, much shorter and nearly straight, prevents the freezing of the crystal onto the lip of the crucible.

Our model predicts a decrease in ribbon thickness with increasing pull rate, consistent with the prior analyses of Zoutendyk [19] and others. However, our nonlinear, thermal-capillary model exhibits a maximum pull rate that is manifest as a limit point in quasi-steady solutions. Through transient analysis of states along both solution branches, we demonstrate that one branch represents operating states that are temporally stable to disturbances, while the other solution branch is made up of unstable states. Our analyses also indicate that the likely failure mechanism for the unstable states is a breakage of the lower meniscus, a result that is consistent with one of the failure mechanisms reported in HRG experiments [14]. Finally, we demonstrate that suitable system design changes that promote a more extended solidification interface, with a correspondingly greater wedge factor, shift the growth rate limit point to larger values and allow for stable growth at faster rates.

Overall, our results are consistent with prior HRG experimental development [14]. For example, our model shows the primary importance of thermal design; achieving the wedge-shaped solidification interface in stable operating states required a careful balance among tip cooling, lower meniscus heating, and ribbon after heating effects. In addition, our analyses demonstrated that fast growth requires large wedge factors and that growth rates are limited by nonlinear interactions manifested by physical failure

mechanisms. We further explore instabilities and failure mechanisms of the HRG system in the following chapter.

We believe that the thermal-capillary model results presented here provide a fundamental basis for understanding the horizontal ribbon growth of silicon. With further analysis, we believe that process improvements will be identified that may simultaneously enable fast growth while circumventing the many failure mechanisms inherent in this promising system.

Chapter 5

Stability Limits

The stability limits are further probed here for the same system considered in the previous chapter that is representative of the experimental system at Energy Materials Research. We first examine the nature of steady operating states as a function of pull rate, keeping all other parameters fixed and providing for melt replenishment. We follow with additional examples of instabilities related to pull angle and melt height and finish with a transient computation showing the need for melt replenishment.

5.1 Limits with respect to pull rate

A typical quasi-steady operating state of our HRG model is depicted in Figure 4.3 and Figure 4.5, where the system geometry, temperature field, and melt flows are shown for a pull rate of $V_g = 4.4$ cm/min. The thermal field shows heating through the crucible, with cooling along the upper surface and along the cantilever shelf. The effects of cooling along the upper ribbon surface are evident. Convection in the upper region of the melt is driven by the combined effects of buoyancy and Marangoni forces, driving the relatively stronger upper flow cell in the clockwise direction. The underlying recirculation vortex rotates in the opposite direction, driven by forces exerted by the upper cell and buoyant forces. The sole streamline connecting to the bottom of the crucible shows the influence

of the make-up flow through the crucible bottom needed for melt replenishment under steady operating conditions.

One of the most significant predictions of the thermal capillary model concerns the response of the ribbon thickness with respect to varying pull rates. Keeping all other parameters constant, the crystal thickness decreases with increasing pull rates, in response to the greater amount of latent heat released at the solidification interface. This effect is shown in Figure 4.6 where each point along the curves represents a solution to the quasi- steady-state model. However, there exists a limiting pull rate beyond which no steady-state solutions exist, which is revealed by a limit point bifurcation and a second solution branch. These two branches are not easily seen in the representation shown in Figure 4.6a, since the two branches nearly overlay each other. When a different projection of the solutions is employed, such as the plotting of the wedge factor (L/t), where L is a measure of the length of the interface and t is the ribbon thickness, versus pull rate in Figure 4.6b, the two solution branches are apparent. Transient analysis conducted indicate that the lower branch represents a family of temporally stable solutions, while the upper branch is unstable. In the ensuing sections, we further examine the nature of operating states as a function of pull rate along this stable lower branch of our quasi-steady, thermal-capillary model.

5.1.1 Crystal freezing onto crucible

Figure 1.11a shows Kudos illustration of what he referred to as bridging between the seed and crucible. We interpret this as a problem of the crystal freezing onto the crucible, and we observe that this limit is approached in our model system when the pull rate is decreased. Under these conditions, a decreasing pull rate corresponds with decreasing the rate of latent heat release. This results in an increase in the thickness of the growing ribbon, as shown by the solid curve in Figure 5.1a (which represents the same states as in Figure 4.6a), and an accompanying shortening of the lower meniscus, as indicated by the dashed line. As the pull rate is decreased, the solidification front approaches the

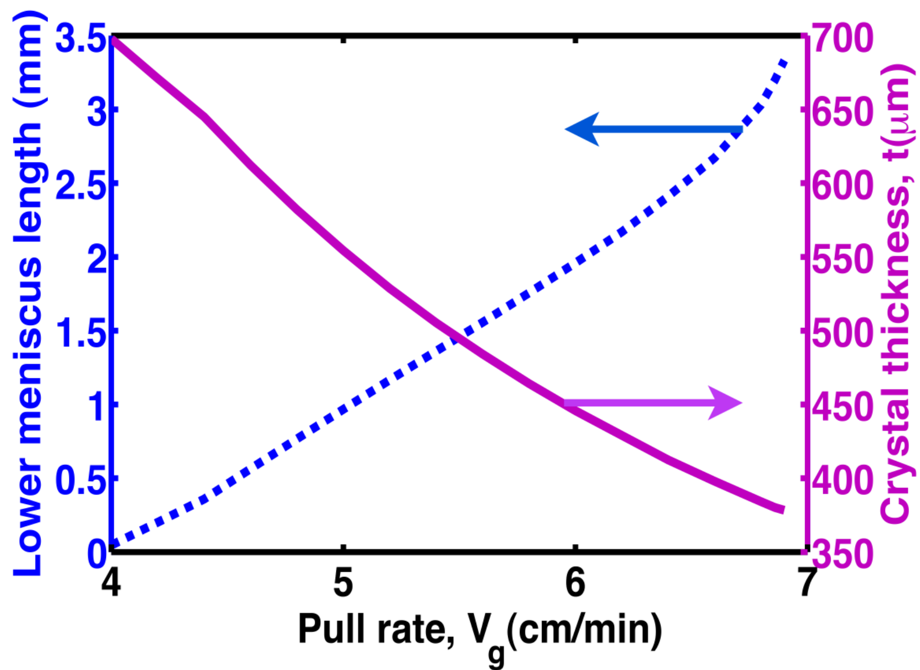

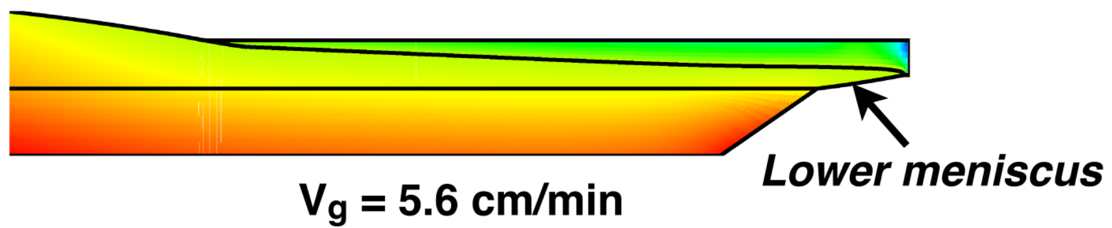

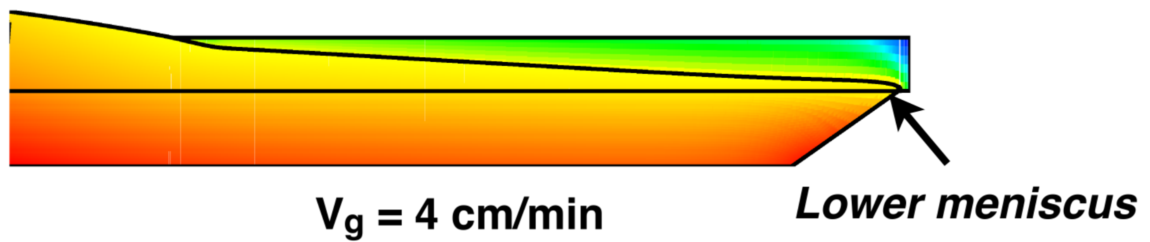

Figure 5.1: Variation of lower meniscus length(dashed curve) and crystal thickness(solid curve) with pull rate (b) Interfacial shapes for pull rates of $V_g = 5.6$ cm/min and $V_g = 4$ cm/min respectively, showing the contracting lower meniscus shape

crucible lip and eventually freezes onto it at approximately $V_g = 4$ cm/min.

This behavior is illustrated in Figure 5.1b showing plots of interfacial shapes obtained for two simulations, at $V_g = 5.6$ cm/min and $V_g = 4$ cm/min. Notice how the meniscus length contracts as the pull rate decreases. This failure mode imposes a lower limit on the pull rate for any particular heat transfer design.

5.1.2 Growth beyond the limiting pull rate

Our thermal-capillary model predicts that there are no steady states beyond the limiting pull rate of $V_g = 6.9$ cm/min for the base-case HRG system under consideration here. We test this assertion here via a transient simulation, where the steady operating state at $V_g = 6.9$ cm/min is subjected at time zero to an increase in pull rate of $V_g = 7.2$ cm/min, a value beyond the limit point exhibited by the quasi-steady-state calculations.

Figure 5.2a shows the crystal thickness and wedge factor as functions of time. After the increase in pull rate at t=0, the ribbon starts to slightly thin as expected, due to the increased growth rate and release of latent heat, and the wedge factor slightly increases. However, after approximately 20s, these quantities suddenly reverse their behavior and diverge.

An examination of the interface geometries, shown in Figure 5.2b, provides clues about the system behavior. First, compare the solidification interface shape between the initial state and that shown for t = 24 s. While the initial state displays the expected wedge-shaped interface, the solid-liquid interface curves sharply downward in the later state. Even more significant is the shape of the lower meniscus, which extends significantly in length at later times. Eventually, the meniscus is too long to support the overlying melt and breaks. Thus, there is no stable steady state for pull rates beyond the limiting value. This result is consistent with the states predicted for the unstable solution branch, which also exhibited very extended lower meniscus shapes, as discussed in Section 4.2.2.

While it is tempting to draw a correspondence of these unstable, extended meniscus

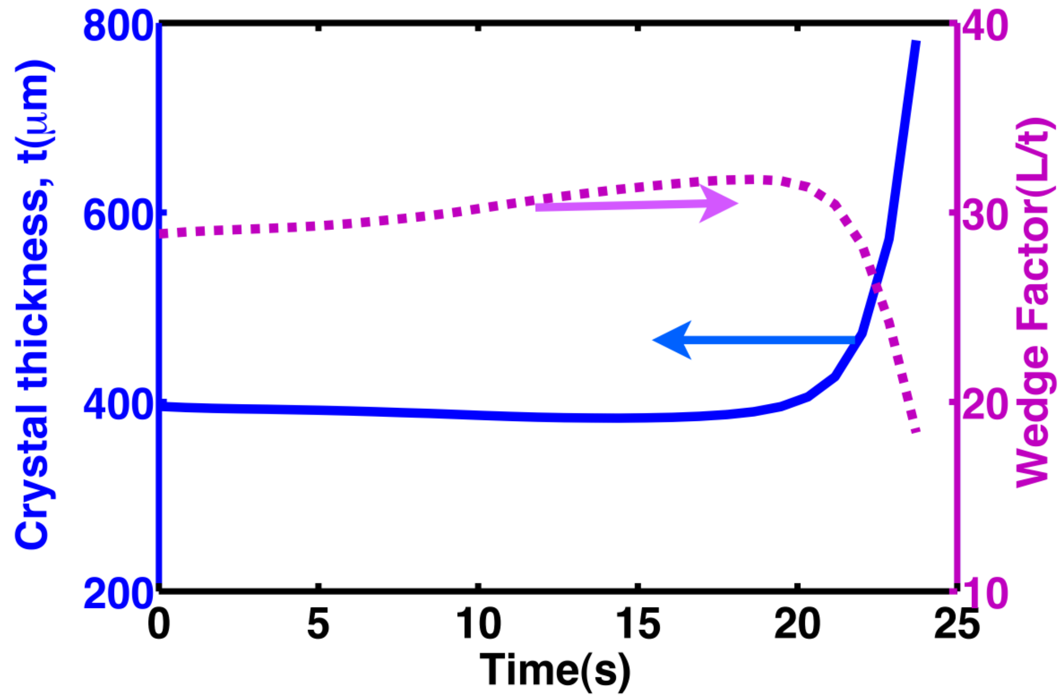

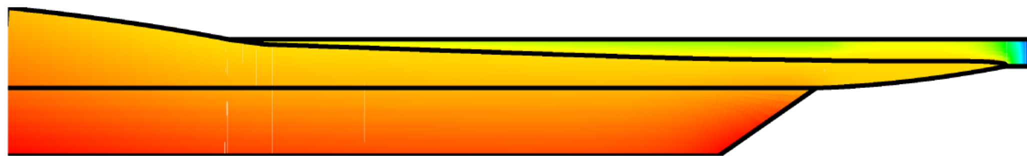

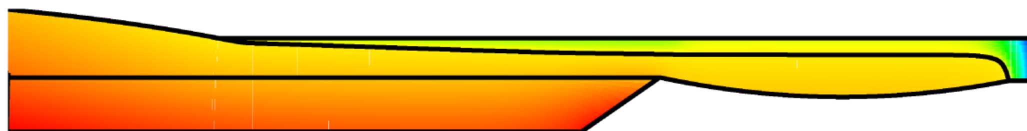

Figure 5.2: (a) Evolution of crystal thickness(solid curve) and wedge factor(dashed curve) with time after a step change in pull rate from $V_g = 6.9$ cm/min to $V_g = 7.2$ cm/min, which is beyond the thermal-capillary limit (b) Evolution of interfacial shapes with time

shapes at pull rates beyond the limit point with the melt spilling problem reported by Kudo (see Figure 1.11b), we believe that a more likely explanation lies in a wetting instability known as the Gibbs limit, which we examine in the following section.

5.1.3 Spilling of the lower meniscus

Our thermal-capillary model assumes that the lower meniscus remains pinned at the crucible edge under all conditions, forming an arbitrary contact angle. In fact, there is a unique equilibrium wetting angle, a material property, for a specific liquid on a specified solid, which we denote as θ_e. Let us carry out a thought experiment to reconcile these two different views.

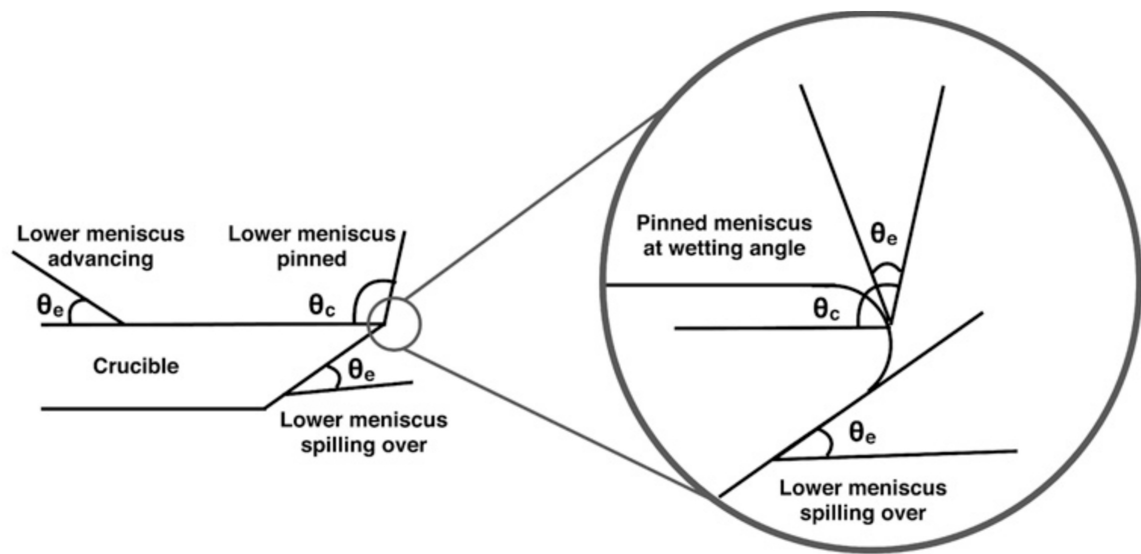

Figure 5.3: Schematic of wetting and pinning of the lower meniscus along the crucible and crucible edge; see text for explanation.

First, consider that there is just enough liquid to wet but not completely cover the crucible lip. We would expect that the liquid would form an angle θ_e, as indicated schematically on the left of Figure 5.3. As we supply more liquid, we would expect this wetting interface to advance toward the edge of the crucible. When the liquid reaches

the edge of the crucible, it stops and pins itself, taking on an apparent angle different from the equilibrium angle, namely θ_C. However, as pointed out lucidly in [27,18], the microscopic radius of curvature at sharp edges allows the meniscus to take on a range of apparent contact angles θ_C, that still locally satisfy the local equilibrium wetting angle θ_e, tangent to the actual surface; see the blow-up image on the right of Figure 5.3. In fact, local equilibrium is satisfied at the edge, pinning it macroscopically, until the angle attains a value such that θ_e is formed with respect to the other solid surface, thus allowing the meniscus to advance across this surface and causing the liquid to spill over the edge.

The range of stable, apparent contact angles allowed at an edge is given mathematically by the condition

$$\theta_e < \theta_C < 180 - \phi + \theta_e, \tag{5.1}$$

where ϕ is the dihedral angle formed at the corner when two solid surfaces meet. For silicon melt wetting a graphite crucible (actually silicon wetting a silicon carbide layer that covers the wetted graphite) with a corner dihedral angle of $\phi = 35^0$, as considered in our base case system, these limits correspond to $30^0 < \theta_C < 175^0$.

Returning to our model predictions, Figure 5.4a shows the shape of the lower meniscus, where x denotes distance away from the crucible edge, for different pull rates. Note that shape of the meniscus changes with pull rate and that the apparent contact angle increases with higher pull rates. The apparent contact angle is plotted as a function of pull rate in Figure 5.4b. The predicted states violate the Gibbs limit at a critical pull rate of $V_g = 6.2$ cm/min, thereby rendering all the states beyond this pull rate unstable to the wetting instability. Thus, our model predicts the melt spilling problem elucidated by Kudo[14], especially plaguing the process at higher growth rates. Significantly, this stability limit occurs at a pull rate lower than the limit point predicted by our model, thus narrowing the window in pull rate for stable process operation.

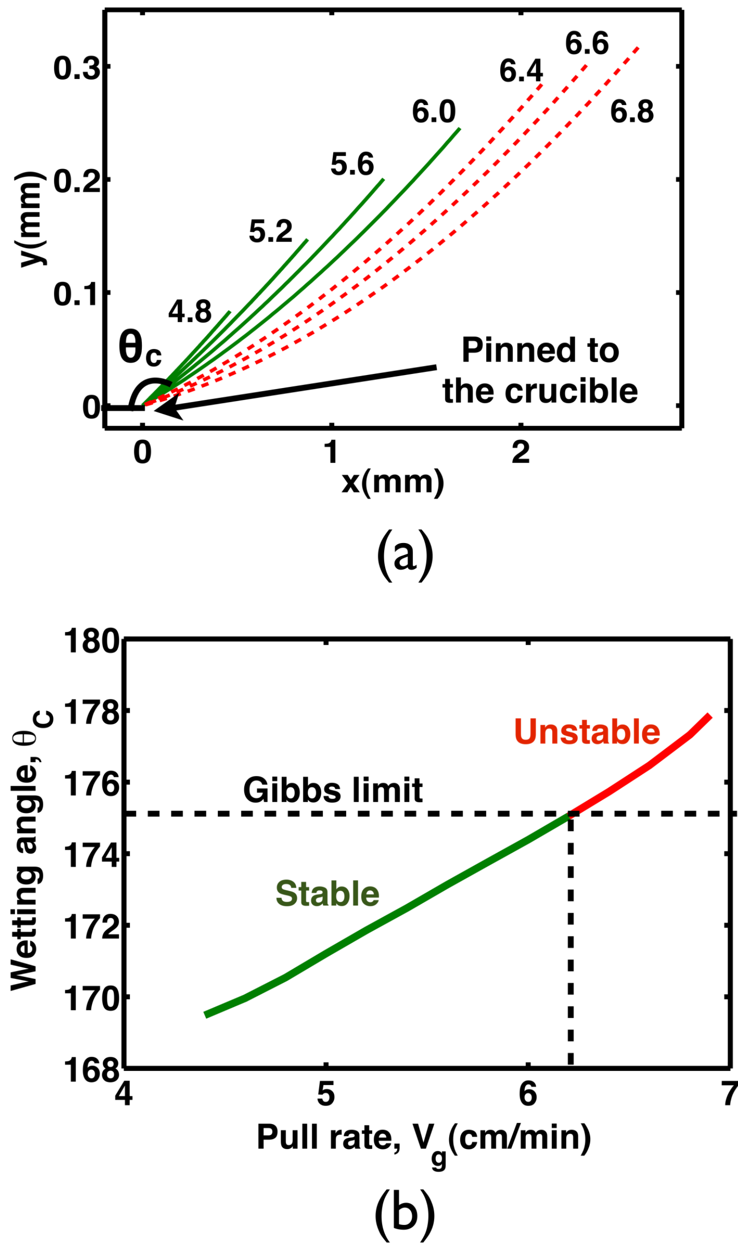

Figure 5.4: (a) Shapes of the lower meniscus for different pull rates from $V_g = 4.8$ cm/min to $V_g = 6.8$ cm/min. Stable shapes are indicated by the solid curves; unstable shapes are indicted by dashed curves. (c) Contact angle as a function of pull rate, marked with regions of stability according to Gibbs limit.

5.1.4 Melt under-cooling at the ribbon tip

The thermal environment of the HRG system is designed to enhance the vertical flow of heat, across the thickness of the ribbon and transverse to the direction of pulling. A natural outcome of this is a small horizontal thermal gradient, and this aspect of heat transfer becomes critically important at the first-to-freeze tip of the ribbon.

In Figure 5.5, we consider the surface temperature of the HRG system, as defined along the path marked with arrows in the upper schematic. In the lower plot, temperature is plotted as a function of distance along the melt and crystal surfaces near the ribbon tip for three different pull rates. Consider first the profile for the pull rate of $V_g = 4.4$ cm/min. Here, the temperature along the surface of the melt is above the melting point and decreases as the ribbon tip is approached. The solid-liquid interface is located precisely at the melting point temperature, where the slope of the profile changes due to the discontinuity in thermal conductivity between melt and solid and the release of latent heat. As the pull rate is increased, more latent heat is released, the ribbon tip shifts toward the right, and, most importantly, the thermal gradient in the melt decreases. All of these effects are readily apparent for the case of $V_g = 5.3$ cm/min in Figure 5.5.

Significantly, the thermal gradient along the melt surface approaches zero at the solid-liquid interface at the pull rate of $V_g = 5.3$ cm/min. Beyond this pull rate, negative thermal gradients develop in the melt in front of the ribbon tip, and the temperature falls below the melting temperature, giving rise to an undercooled region as highlighted in Figure 5.5. The undercooled melt in this region is thermodynamically unstable and will, at some point, produce a burst of crystallization. This is exactly the observation of polycrystalline growth observed by Kudo, shown in Figure 1.11c.

Interestingly, such negative thermal gradients and undercooled regions near the growth interface have been observed in several other ribbon growth processes. Thomas and Brown predicted melt supercooling to occur in vertical EFG systems at higher

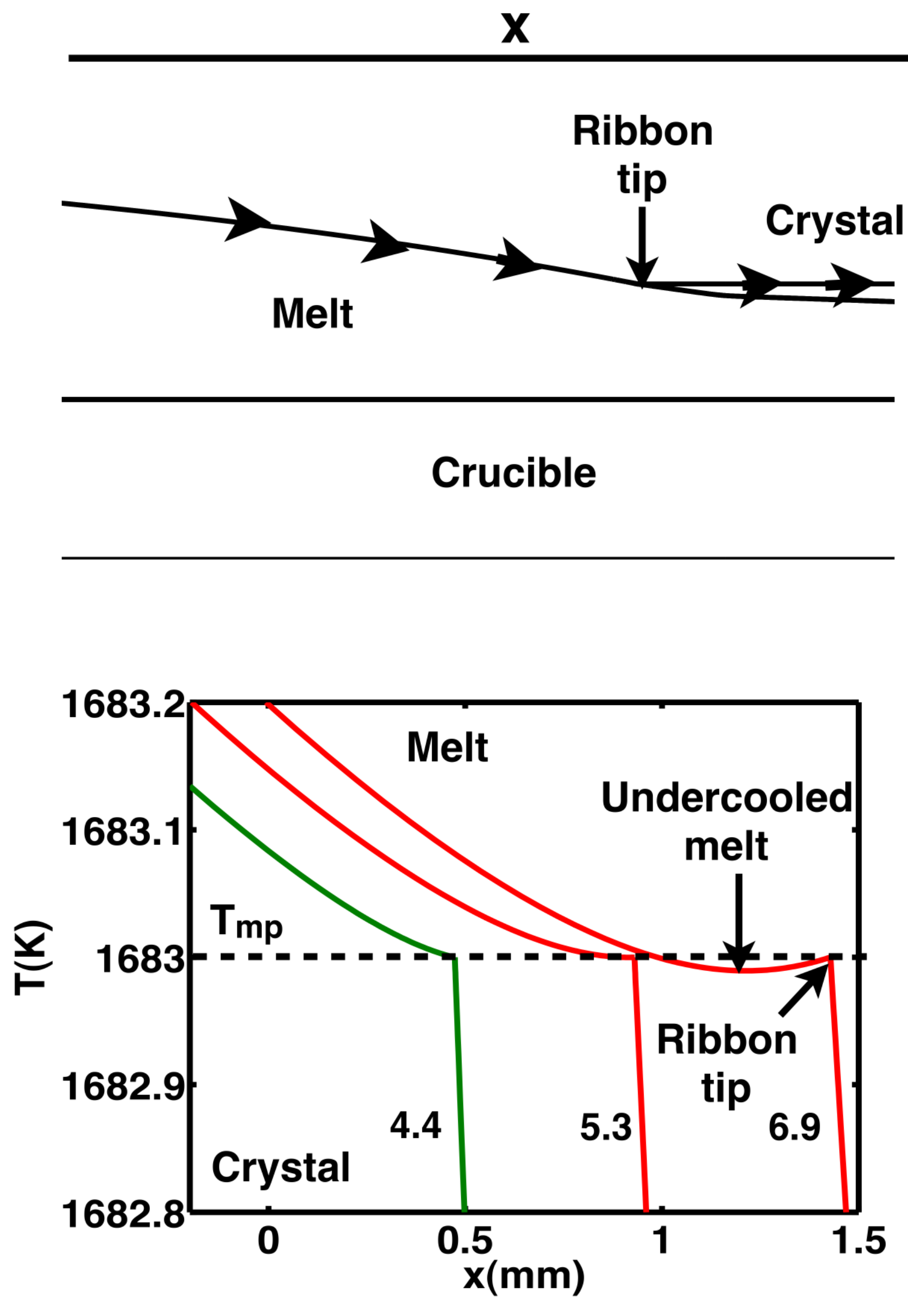

Figure 5.5: Surface temperature profile along the upper meniscus and crystal surface, near the ribbon tip (above), plotted for three different pull rates of V_g = 4.4 cm/min, 5.3 cm/min, and 6.9 cm/min, showing regions of undercooled melt at higher growth rates (below).

growth rates [90]. Dendritic growth forms have been observed in silicon ribbon growth on substrate (RGS) and laser remelting systems, and these results have been attributed to fast growth and melt undercooling [20, 98, 99]. More recently, Tokairin et al. [100] observed unstable solidification of silicon in a small-scale, film growth system and attributed this behavior to undercooled liquid adjacent to the solidification interface at higher growth rates.

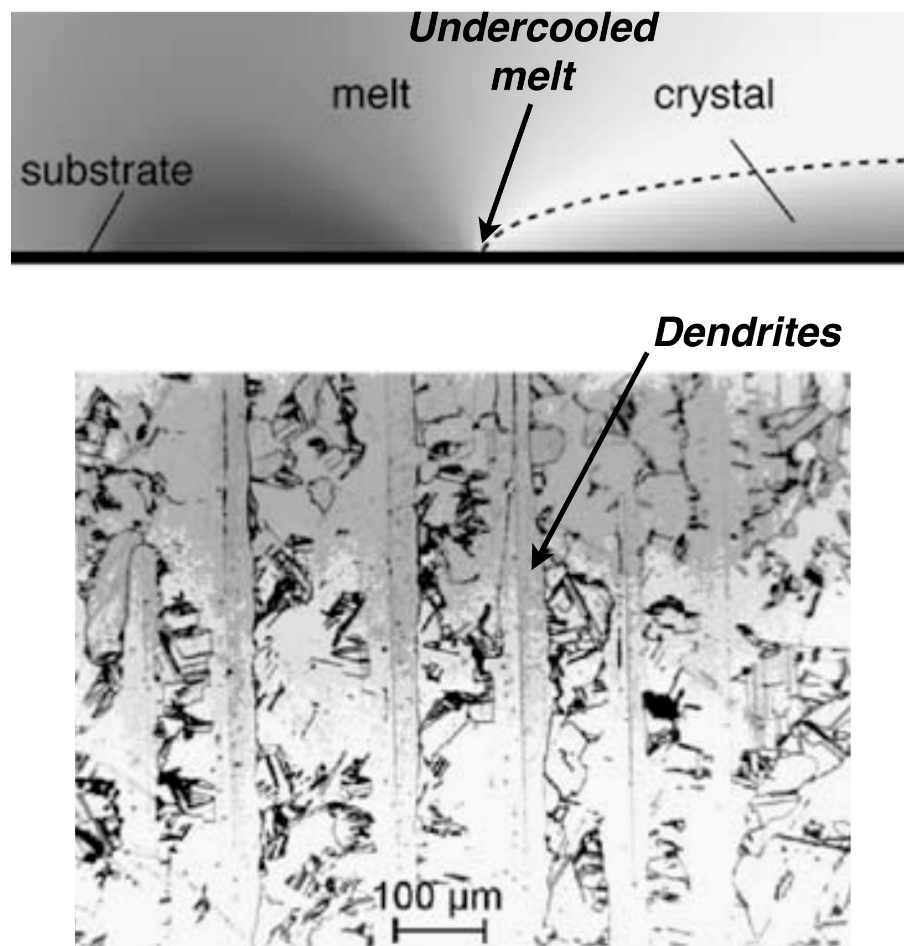

Figure 5.6: Evidence of dendrites on a RGS grown ribbon from an undercooled melt [20]

5.2 Limits due to pull angle and melt height

In the previous sections, we have presented steady-state operating limits that arise when the pull rate is changed while keeping all other parameters constant. It is important to realize that, due to strong coupling of nonlinear phenomena in the HRG system, changing virtually any parameter will also give rise to operating limits. In the following sections, we discuss the effect of pull angle and melt height at a constant pull rate of V_g = 4.4 cm/min.

5.2.1 Pull angle

Although HRG process involves pulling the ribbon horizontally, there have been several investigations exploring the possible advantages of an inclined pulling mechanism. LASS (low angle silicon sheet) growth is one such process, very similar to the HRG process, where silicon ribbons are produced by pulling at a small positive angle to the horizontal [101, 102, 103].

Our thermal-capillary model reveals limit-point bifurcation behavior with respect to pull angle, with a limiting value of 1.3^0 and multiple solution branches, as shown in Figure 5.7a, where the lower meniscus length is plotted as a function of pull angle. From our knowledge of the stability characteristics of the horizontal pulling case, we can assert that the solution branch denoted with a solid line is stable. Increasing the pull angle elongates the lower meniscus, without affecting the crystal thickness significantly, thus pushing the solidification interface upward and away from the cantilever shelf. This predicted behavior is consistent with Kudos recommendation of inclined pulling mechanism (IPM) as a potential solution to counter the crystal-crucible bridge formation problem, especially during the seeding stages of growth where the pull rates have to be essentially low [14].

Similar to the limits discussed in the prior sections, the states along this stable solution branch are bounded by points that mark the onset of crystal-crucible bridge

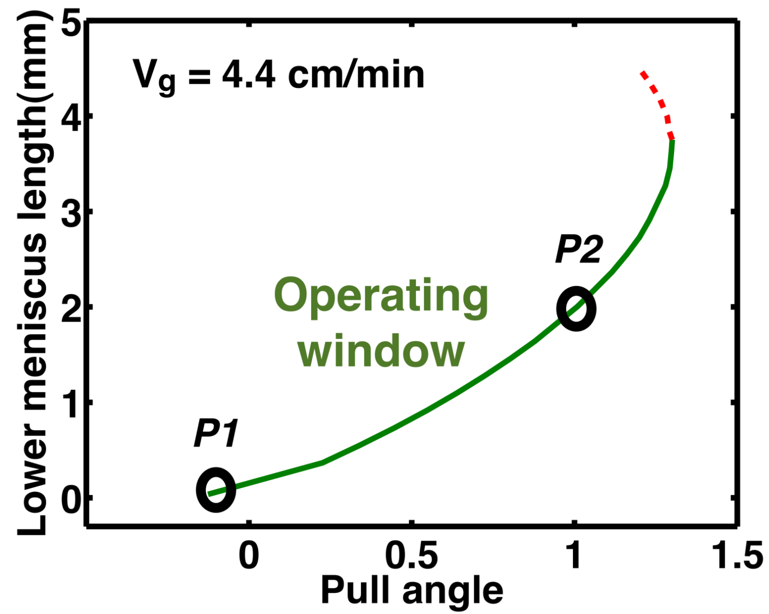

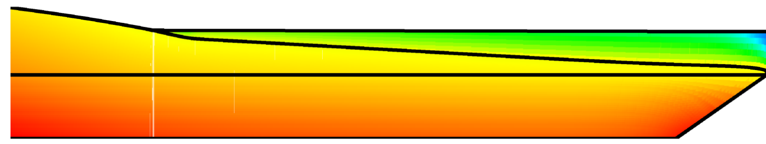

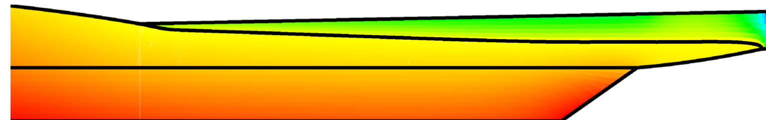

Figure 5.7: Stability limits exist for the variations of other parameters. (a) Lower meniscus length plotted as a function of pull angle. (b) Interfacial shapes corresponding to the stability limits at P1 and P2 in (a).

formation and melt spill over due to Gibbs limit violation, marked by points P1 and P2, respectively, in Figure 5.7a. The geometry of these limiting states are illustrated in Figure 5.7b. The very small range of pull angles allowed for stable steady-state operation suggests that the precise control of this parameter is important for real-world systems.

5.2.2 Melt height and batch operation

The level of the melt height is a parameter with respect to steady-state growth with melt replenishment, and the response of the process to this parameter is examined in Figure 5.8a and b. The system behavior is very similar to that exhibited in the prior section, leading to a small range of stable operating states bounded by crystal-crucible freezing (P1) and meniscus spilling (P2).

This sensitivity to melt height is reflected in the batch operation of the HRG system without melt replenishment. We investigate this behavior by replacing the make-up flow boundary condition at the crucible bottom with a no-slip velocity condition to investigate the batch mode. We assume that the quasi-steady state system with $V_g = 5$ cm/min is operating and that melt replenishment is turned off at time zero. The temporal evolution of the process is computed by time integration of the thermal-capillary model, and results are shown in Figure 5.9.

As growth proceeds, the melt height drops due to the silicon removed by the pulled ribbon. The falling melt level drags the solidification interface down, towards the cantilever shelf, thereby thinning the emerging ribbon steadily with the progress of time. Both of these effects are plotted in 5.9a. The interfacial shapes, plotted in 5.9b, show the exit meniscus contracting and the solidification interface approaching the crucible. Freezing of the ribbon to the crucible terminates the batch operation after about 25 s of growth.

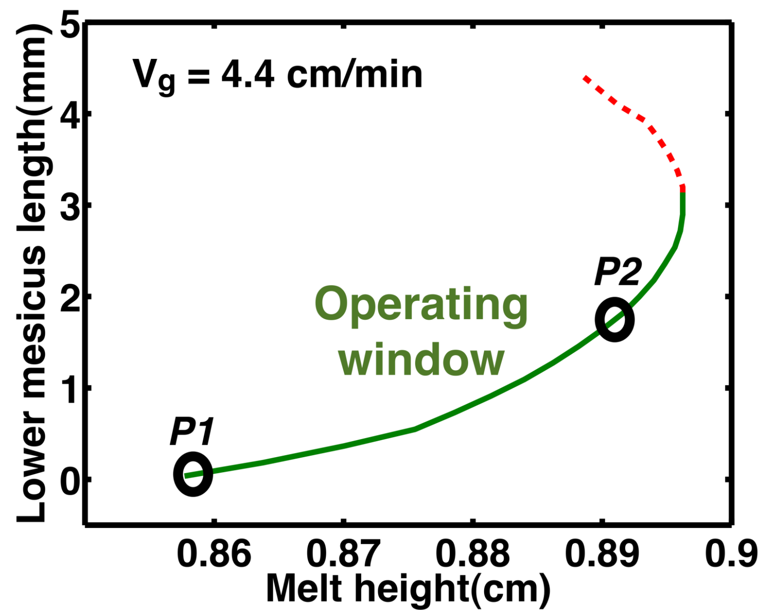

(c)

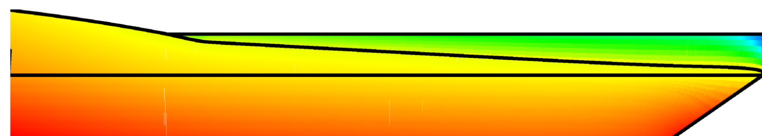

P1: Crystal freezing onto crucible

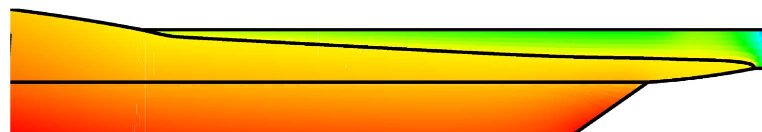

P2: Spilling over of lower meniscus

(d)

Figure 5.8: Stability limits exist for the variations of other parameters. (a) Lower meniscus length plotted as a function of melt height. (b) Interfacial shapes corresponding to the stability limits at P1 and P2 in (a).

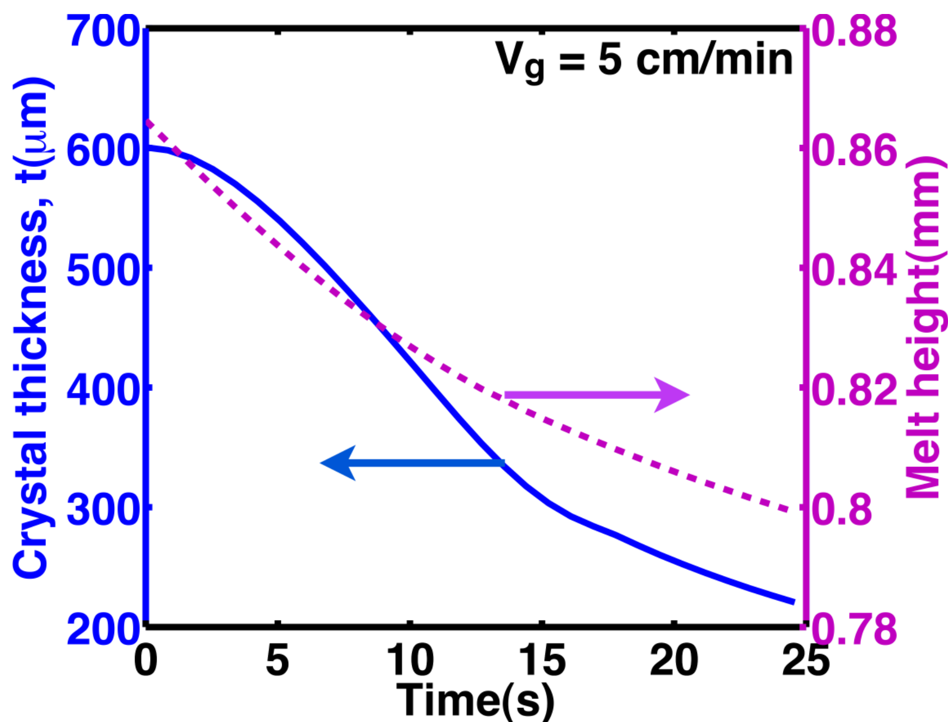

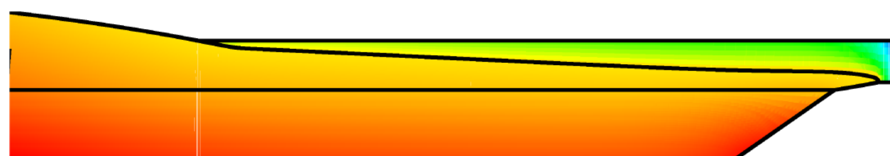

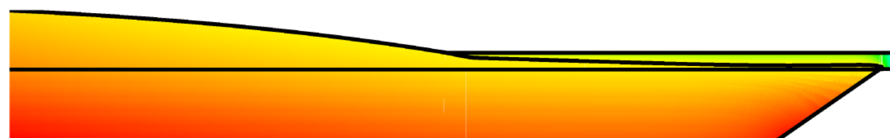

Figure 5.9: (a) Plot of crystal thickness(solid curve) and melt height(dashed curve) with time during a batch simulation of the process at $V_g = 5$ cm/min (b) Evolution of interfacial shapes with time

5.3 Conclusions

We have applied the rigorous, thermal-capillary model developed in Chapter 2 to discover and better understand stability limits of the HRG process with respect to several operating parameters. Significantly, our model predicts all of the major problems identified by Kudo[14]-bridging, spilling, and polycrystalline growth. Importantly, our analysis also reveals the physical mechanisms underlying these limits and additional interactions among other parameters that may limit the attainment of stable growth states.

While our original analysis of this system revealed limit-point bifurcations and multiple solutions with different stabilities, a key conclusion from the present study is that there are additional phenomena that limit stable, steady-state growth to a much narrower set of operating parameters. Indeed, we present a revised picture of the much smaller operating window allowing stable growth in Figure 5.10 for this HRG system, where crystal thickness is plotted as a function of pull rate. This operating window is bounded at low growth rates by crystal-crucible freezing (bridging) and at higher growth rates by the underlying limit point of the steady-state solutions, the violation of the Gibbs limit for the lower meniscus (resulting in spilling of the melt), and the melt undercooling phenomenon (which will result in poly- crystalline growth at the ribbon tip). We believe that these mechanisms that limit system operation will be generic to all HRG systems.

Other analyses presented here show that growth limits are also encountered by changes in other operating parameters, such as pull angle and melt height. The ambient temperature of the heaters and coolers, such as cantilever shelf heater, crucible heater, after heater, and passive radiative coolers, are also found to give rise to similar operating windows.

Clearly, the horizontal ribbon growth process holds great promise for achieving very fast growth rates. However, this promise must be tempered by an awareness of the

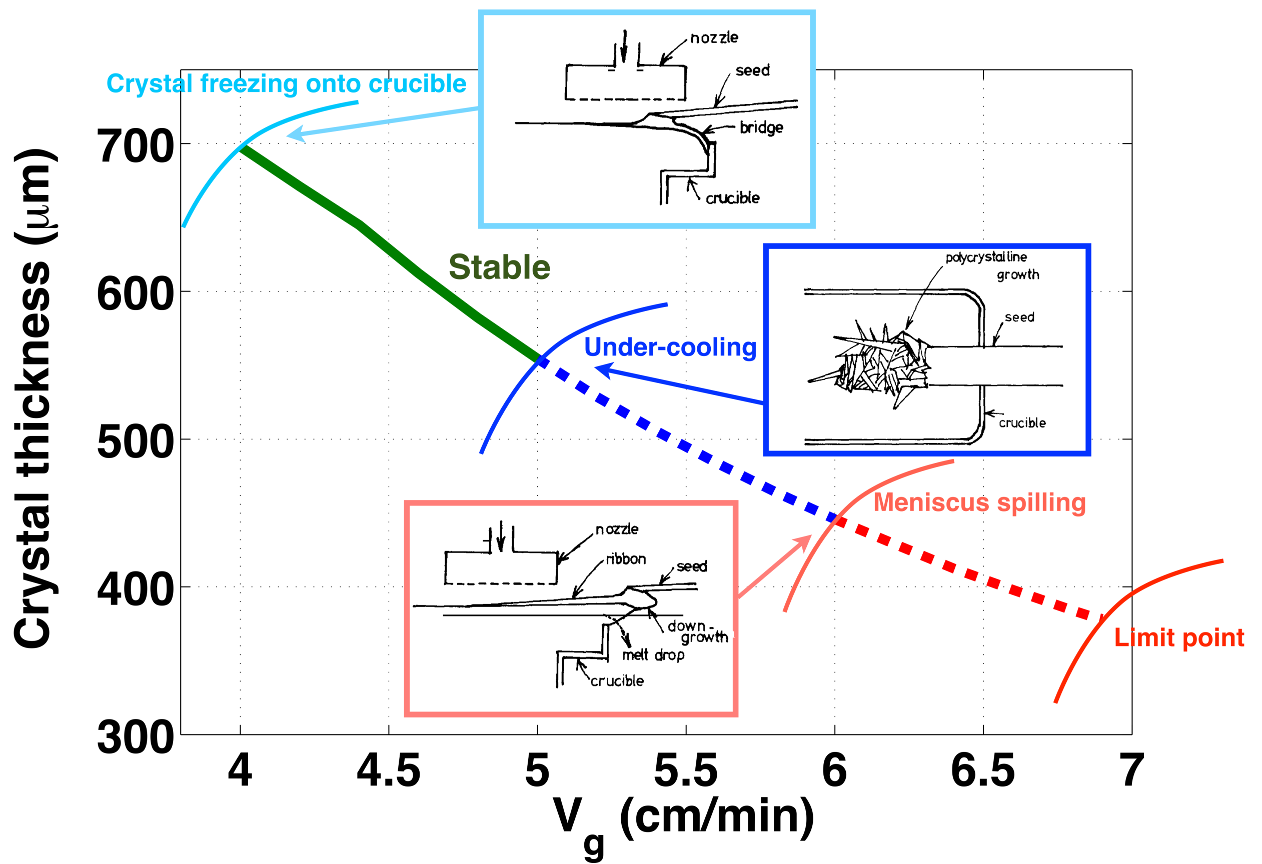

Figure 5.10: Stability limits and operating window with respect to pull rate

many instabilities that limit stable operation to relatively narrow operating windows in parameter space. For example, the model system considered here would need to be optimized for higher growth rates and smaller crystal thicknesses to be commercially viable. We have already discussed possible means of system design by optimizing various process parameters to reach such goals. Toward development of the HRG method, we propose that rigorous computational models capable of predicting failure modes and analyzing design changes to achieve stable operation will be invaluable.

Chapter 6

Segregation Analysis

So far we have developed and applied a comprehensive multi-physics thermal-capillary model to study the characteristics and underlying challenges of the HRG system[104, 105]. Our model results demonstrated the feasibility of the process, subject to suitable heat transfer design, and revealed existence of limiting growth rates and multiple branches of steady states that correspond to stable and unstable behavior. The model further predicted occurrence of various failure events such as bridging of crystal onto the crucible, spilling of melt from the crucible, and the undercooling at the ribbon tip, that are consistent with prior experimental observations, thereby identifying narrow operating windows, in multi-dimensional parameter space, immune to these destabilizing failure modes. Although this modeling effort is deemed successful in predicting failure modes and analyzing design changes to achieve stable operation of the system, it however, is oblivious to the quality of the growing crystal.

Depending on the growth technique, Si crystals can possess high concentrations of impurities such as B, C, O, P, metal impurities etc and can have crystallographic defects such as clusters of voids and interstitials, dislocations, grain boundaries, twinning planes, stacking faults etc. The presence of these impurities and defects deteriorate the quality of the crystal and their interactions can adversely affect the performance of the

photovoltaic Si devices. Carbon and oxygen impurities usually result from the interactions of melt with graphite heaters and quartz crucibles respectively and if present in excessive concentrations in the crystal, they form precipitates of SiC[106] and SiO_2[32]. Group III atoms such as B, Al, Ga and Group V atoms such as P, As are intentionally added as substitutional dopants to produce p-type and n-type silicon. However, excessive dopant concentrations can again result in precipitates and formation of complexes with other impurities. The precipitates of metallic impurities such as Fe, Ni, Cu, Cr, Co and Mo are commonly observed in crystals grown from low-cost solar-grade silicon feedstock[107, 108, 109]. The precipitates of these super-saturated impurities may lead to the formation of structural defects which may then act as nucleation sites for further interactions with impurities[110, 111]. Overall, these interactions lead to recombination centers for minority charge carriers reducing their life time and concomitantly the cell efficiency.

Toward deepening our understanding of the horizontal ribbon growth process, this study aims to clarify how dopants and impurities are redistributed into the growing ribbon. The segregation of dopants and impurities has been modeled in the past for vertical EFG systems. Kalejs [112] first studied impurity redistribution during vertical silicon ribbon growth via numerical solution of the convection-diffusion equation in a geometry representative of an EFG system. Ettouney *et al.* [92] considered aluminum segregation during the edge-defined film-fed growth of silicon sheets via a thermal-capillary analysis similar to the approach employed here. Later analyses by Kalejs and co-workers refined the understanding of segregation in vertical growth systems [113, 114, 65]. Braescu and co-workers numerically modeled segregation occurring in thin, cylindrical rods of silicon [115] and small-diameter fibers of oxides [116] grown via EFG methods. Smirnova *et al.* [117] employed experiments and modeling to understand redistribution of impurities during EFG silicon crystal growth. To our knowledge, there has been no prior analysis of segregation in horizontal ribbon growth systems.

Our modeling approach is outlined in the following section, followed by a discussion

of several representative cases. We find that the unusual geometry of the HRG system, in particular its extended solidification interface, leads to unexpected concentration profiles in the ribbon. We find that solute redistribution in this system is quite inhomogeneous; however, the particular segregation profiles arising in HRG may be beneficial.

6.1 Thermal-capillary, species segregation model

A two-dimensional schematic representation of the HRG system with the melt-crystal-crucible domains, arrangement of heating and cooling mechanisms, make-up flow for melt and other design details are already clearly presented. The thermal-capillary model rigorously accounts for mass, momentum and energy conservation equations while simultaneously accounting for capillary physics of the menisci, solidification at the interface and self-consistent determination of ribbon thickness.

For the segregation analysis of interest here, we solve for species conservation in the melt domain, using the geometry and velocity field provided by the thermal-capillary analysis. We assume that there is no effect of species concentration on melt density nor an effect of concentration on the solidification temperature of the melt. Including solutal buoyancy and concentration-dependent melting temperature are readily handled within the framework of our model; however, we consider only the simpler, decoupled case in this study.

Thus, we solve for an additional conservation equation for a dilute, single species in the melt.

$$\frac{\partial c}{\partial t} + \mathbf{u} \cdot \nabla c = D \ \nabla^2 c \tag{6.1}$$

where c is the concentration of the species in the melt, $\mathbf{u}$ is the melt velocity, and D is the diffusivity of the species in the melt. This equation accounts for solute transport mechanisms, where convection, on the left-hand side of the above equation, is balanced by diffusion processes, shown on the right-hand side of eqn. (6.1).

At the solidification interface, an equilibrium relationship is applied between concentration of the species in the melt, c, and that of the crystal, c_s, as follows:

$$c_s = kc \tag{6.2}$$

where k is the equilibrium partition or distribution coefficient. This equation serves to set the concentration in the solid, c_s, at the solidification interface. We ignore any redistribution of the solute in the solid by solid-state diffusion. This is a reasonable approach, since, in high speed growth techniques such as HRG, the cooling times of the ribbon are of the order of few seconds, and solute distributions are expected to be quickly frozen-in by the rapid drop in temperature.

When eqn. (6.2) is incorporated into a species flux balance across the solidification interface, the following boundary condition arises:

$$-D(\mathbf{n} \cdot \nabla c) = c\ (\rho_s/\rho_m - k)\ \mathbf{n} \cdot (V_g \mathbf{e}_x + \dot{\mathbf{x}}), \tag{6.3}$$

where $\mathbf{n}$ is a unit vector normal to the interface, ρ_s and ρ_m are the densities of the solid and liquid, respectively, V_g is the horizontal pull rate (which is identical to the crystal growth velocity under steady-state conditions), and $\mathbf{e}_x$ is the unit coordinate vector in the horizontal direction (which characterizes the direction of pulling of the sheet), and $\dot{\mathbf{x}}$ is the rate at which the interface moves with respect to the fixed coordinates. Under quasi-steady growth conditions, described by the operation of the system under melt replenishment, the interface is motionless in the coordinate frame, and $\dot{\mathbf{x}} = 0$.

To complete the specification of the species transport problem, we consider two different sets of boundary conditions. One case considers the case of no interactions of the melt with the crucible and no transport of the species to or from the surrounding gaseous atmosphere of the growth system. While this is a reasonable assumption for many chemical species, it certainly cannot be applied universally. For example, this condition does not hold for reactive species such as carbon and oxygen, and quantitative predictions would require consideration of whole-furnace transport and reaction; see for

example [118]. Nevertheless, we proceed for this simplified case by specifying no-flux conditions,

$$\mathbf{n} \cdot \nabla c = 0, \text{ along crucible walls and menisci,} \tag{6.4}$$

where $\mathbf{n}$ is a unit vector normal to the boundary and directed outward from the melt. We account for melt replenishment by setting the additional boundary condition of,

$$c = c_0, \text{ along crucible bottom,} \tag{6.5}$$

where c_0 represents the impurity concentration of the melt in-flow. This approach will be used for most of the results presented here.

In addition, in Section 6.6, we will consider a case for crucible-melt interaction that specifies the species concentration to be at its saturation point along the crucible and with no exchange across the melt menisci. This would correspond to a worst-case scenario, such as might exist for carbon if the crucible were graphite and without a liner. The study of carbon transport, supersaturation, and silicon carbide particle formation during EFG silicon growth has been studied using a similar approach by Rajendran *et al.* [114]. We model this case by specifying no-flux conditions,

$$\mathbf{n} \cdot \nabla c = 0, \text{ along the menisci,} \tag{6.6}$$

along with setting,

$$c = c_{sat}, \text{ along crucible walls and bottom,} \tag{6.7}$$

6.2 Quasi-steady base case

For the system geometry, parameters and properties given in previous chapters, base-case computation was performed with an applied pull rate of $V_g = 4.4$ cm/min and the emerging ribbon thickness is found to be $t_0 = 674\mu m$. A mesh comprising 46,242 elements was employed for all calculations presented here, giving rise to a total of 745,464 unknowns. This mesh contained elements substantially finer than those employed in

our prior computations, owing to the challenge presented by accurate computation of the convection-dominated mass transport that is characteristic of melt crystal growth segregation. Great care has been taken to address this issue by choosing a highly resolved mesh along with grading of the mesh to compress elements toward the melt-crystal interface, where sharp concentration boundary layers arise.

To compute segregation of a solute or impurity in this system, we assume a partition coefficient of $k = 0.07$ and a diffusivity of $D = 4.85 \times 10^{-5}\text{cm}^2/\text{s}$. While these values are representative of carbon in silicon [119, 120], they are employed here in the context of understanding the general characteristics of segregation in this system. A discussion of carbon segregation in particular is presented in Section 6.6, where the effects of crucible dissolution are considered. For the base case and ensuing computations (except the aforementioned case considered in Section 6.6), we consider steady-steady growth with no crucible wall interactions, so the boundary conditions specified by eqns. (6.4) and. (6.5) are applied.

At the global level, the solute concentration field is nearly uniform throughout the melt, as shown by Figure 6.1a, where almost the entire melt is seen to be at a concentration c_0. However, significant variations of composition are observed upon closer examination of the melt under the solidification interface, shown by the expanded views (and different color scales) of Figures 6.1b and c. Because of the partitioning between solid and liquid, solute is rejected during growth, resulting in higher concentrations in the melt immediately adjacent to the interface. Under most of the interface the melt flow is quite weak, and the excess solute diffuses away, establishing a classical diffusion layer normal to the interface; see Figure 6.1b. However, the Marangoni flow near the lower meniscus is strong enough to promote significant convective mixing, which disrupts the diffusion layer in this region; see Figure 6.1c.

The combination of interface shape, solute rejection, diffusion, and flow interact to produce an extremely nonuniform distribution of the solute in the growing ribbon. Figure 6.2a plots the resulting composition of the solid across the thickness of the crystal,

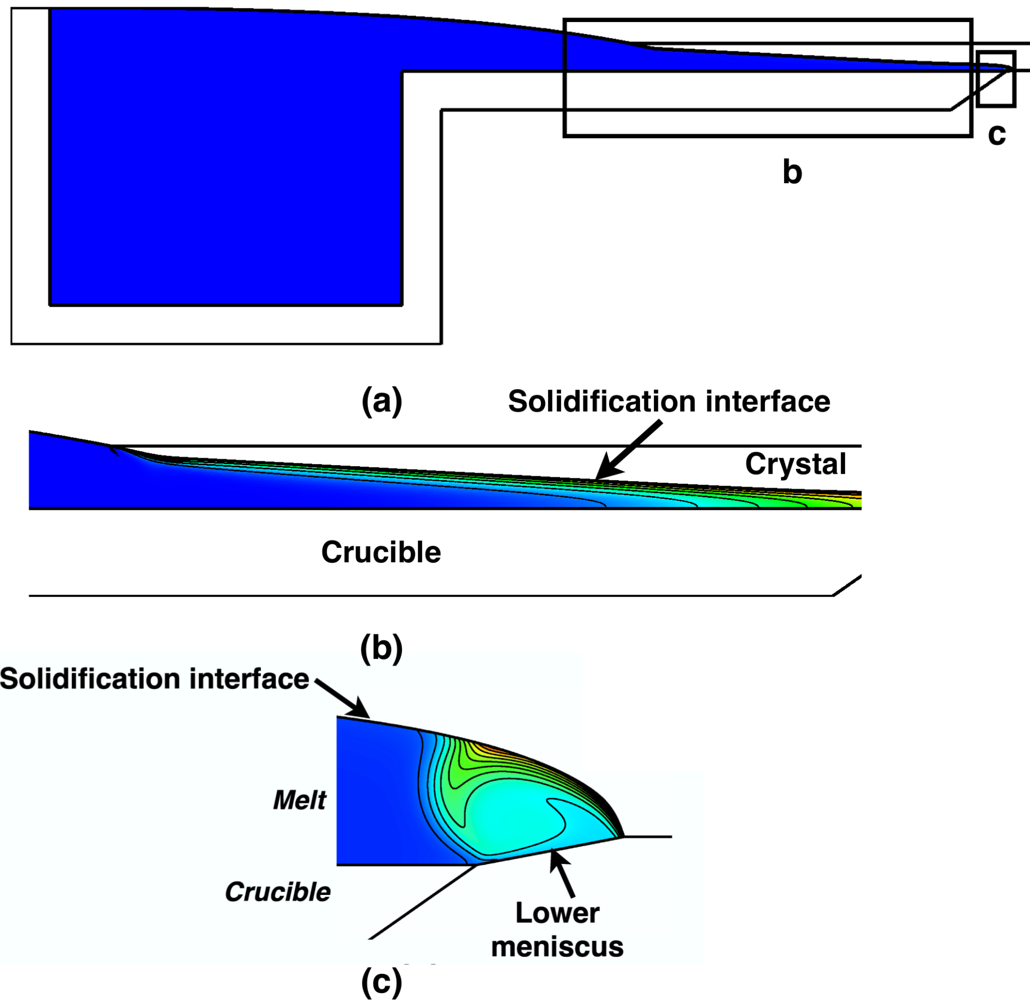

Figure 6.1: (a) Global representation shows a nearly constant composition field through the melt. (b) Expanded view of melt composition under the solidification interface; maximum concentration is $c_{max} = 4.52c_0$, minimum concentration is $c_{min} = c_0$, and contour spacing is $\Delta c = 0.58c_0$. (c) Expanded view of melt composition near lower meniscus; maximum concentration is c_{max} =94.3c_0, minimum concentration is $c_{min} = 3.64c_0$, and contour spacing is $\Delta c = 9.1c_0$.

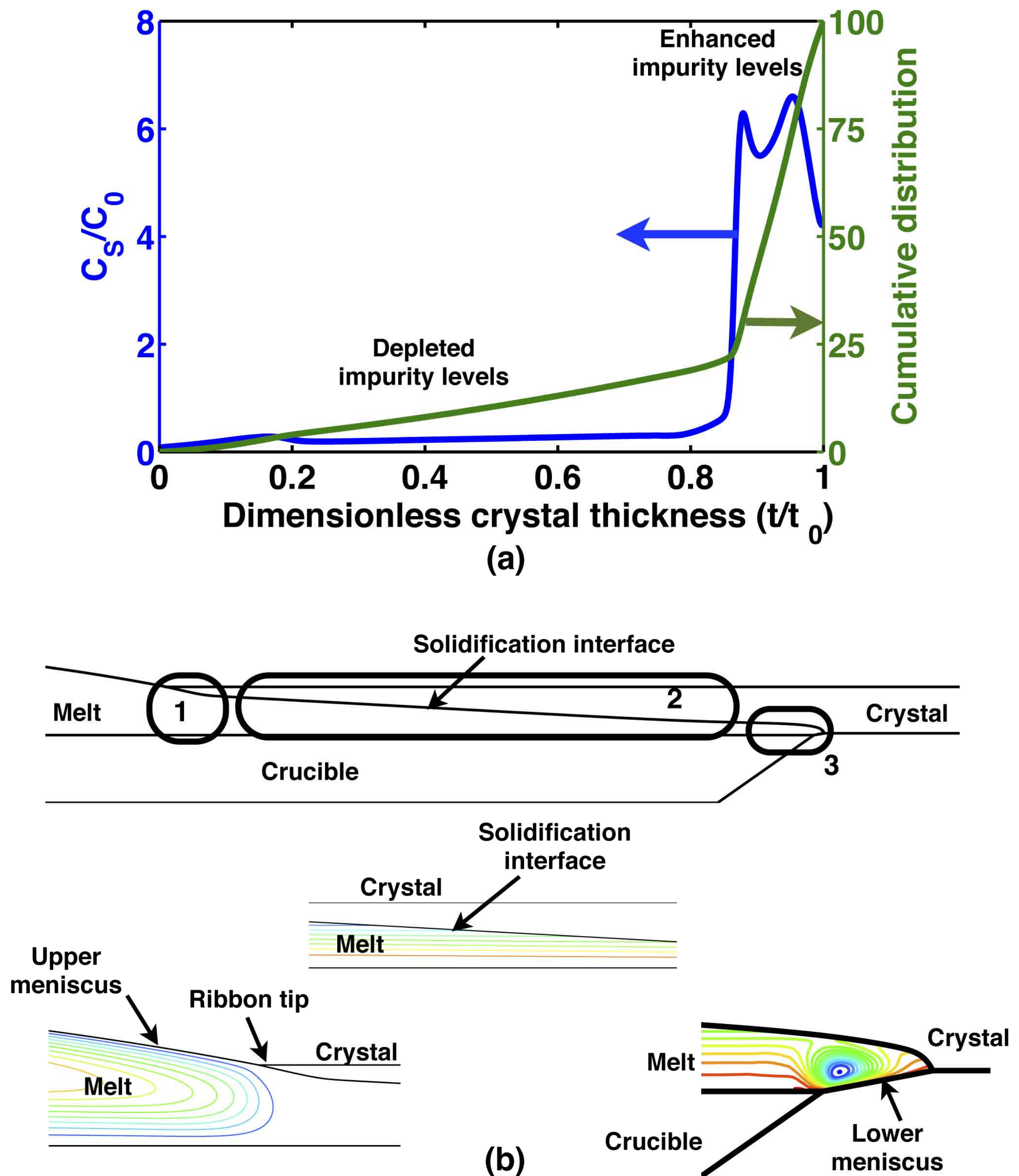

Figure 6.2: (a) Solute concentration and cumulative distribution of solute in crystal are plotted as a function of crystal thickness; t=0 refers to the top crystal surface and t=t_0 refers to the bottom crystal surface. (b) Depiction of streamlines of melt flow in various zones under the solidifying crystal.

showing both the local solute concentration and the cumulative amount of solute in the ribbon. The majority of the upper thickness of the crystal is relatively depleted of solute, with c_s/c_0 values below 0.35, whereas solute concentration rises sharply in the narrow bottom portion of the crystal resulting in enhanced impurity levels. The cumulative distribution of solute in the crystal, calculated by integrating the concentration field from top to bottom, is also plotted in Figure 6.2a. Only 25% of the total amount of solute in the ribbon is trapped in the top 87% of the crystal, with the remaining solute concentrated in the bottom 13% of the crystal thickness.

These redistribution effects can be explained by the importance of convective transport within the melt near the solidification interface. Three important zones with different flow influences are depicted in Figure 6.2b. A strong clockwise rotating vortex, setup by Marangoni forces along the upper meniscus, influences mixing near the interface in the highlighted zone 1, near the ribbon tip, and gives rise to the small local maximum in solute concentration. Solidification flow is the dominant flow mechanism in zone 2, as indicated by the streamlines parallel to the pulling direction under the solidification interface. This very weak and almost uniform flow is nearly orthogonal to the diffusion layer and only minimally affects it, thus resulting in a nearly constant solute level incorporated into the ribbon through this zone. The melt narrows as the crucible edge is approached, and the diffusion layer begins to interact more strongly with the wall. In the confined geometry, it is difficult for the rejected solute to diffuse away from the interface. Furthermore, the counter-clockwise rotating Marangoni flow cell, generated by the lower meniscus in zone 3, strongly mixes the diffusion layer and is responsible for the sharp rise in solute concentration.

A direct correspondence is found between the tangential melt velocity near the solidification interface and the solute profile through the ribbon. A steady-state diffusion layer of thickness of D/V_g forms ahead of the solidification interface as a result of segregation for the case of purely diffusive transport [121]. For the base case conditions considered here, at an operating horizontal pull rate of $V_g = 4.4$ cm/min, this diffusion

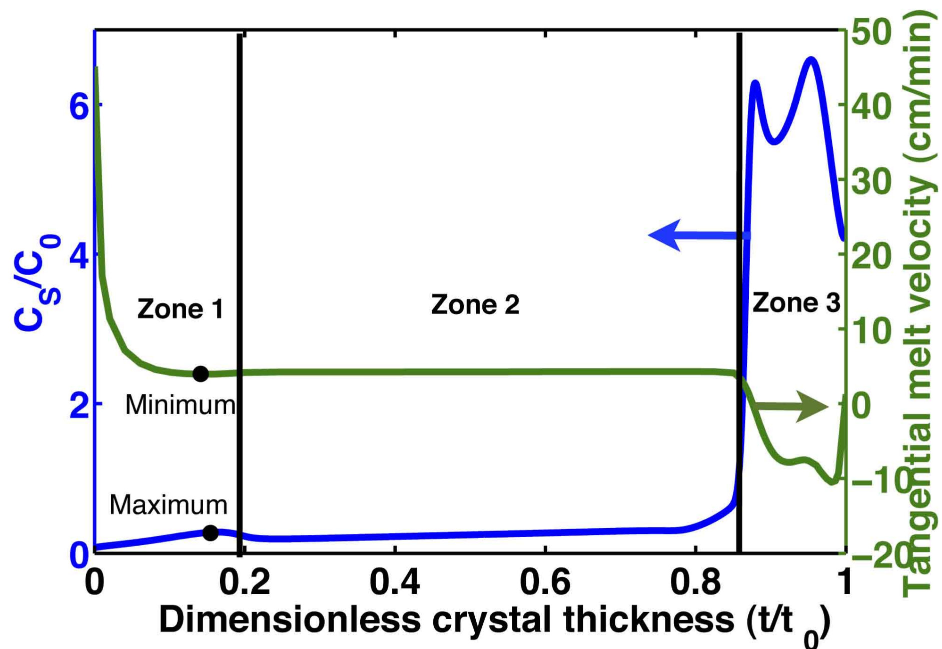

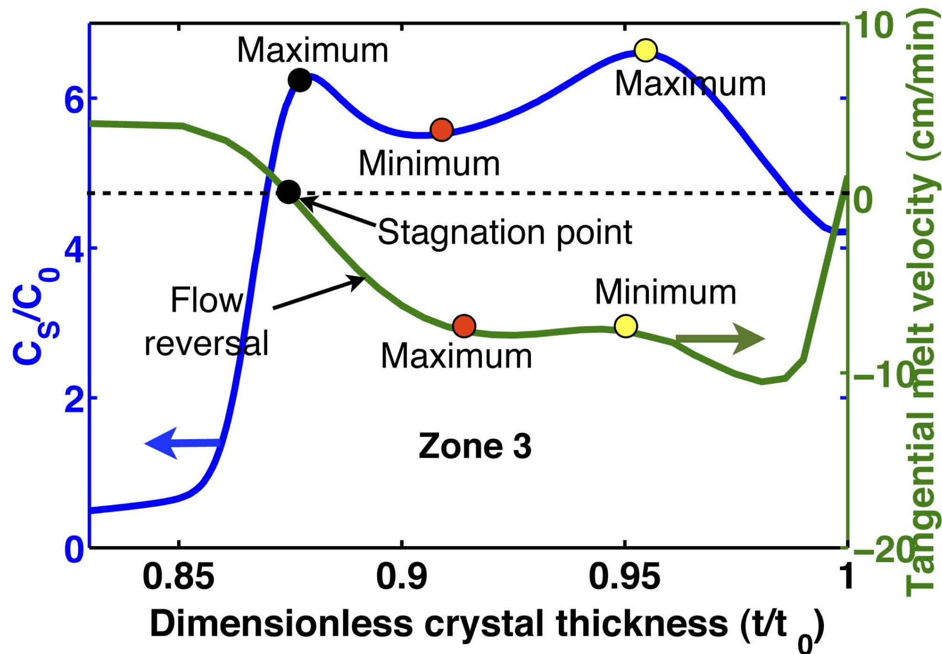

Figure 6.3: (a) Solute concentration and tangential melt velocity close to the interface are plotted as a function of crystal thickness. Zone numbers refer to regions identified in previous figure. (b) Solute concentration and tangential melt velocity close to the interface are plotted as a function of crystal thickness in zone 3, near the bottom of the ribbon and the lower meniscus.

layer thickness is estimated to be 6.6 μm. Figure 6.3 shows the relationship between the carbon redistribution profile and the tangential melt velocity (i.e., that component parallel to the solidification interface), plotted in this figure along a path parallel to and at a distance of 5 μm normal to the interface (i.e., within the diffusion layer). Since the impurities are convected from regions of high melt velocities to low, we expect an inverse relationship between these quantities. This is illustrated by the plots of Figure 6.3, where solute concentration in the ribbon and tangential melt velocity are both plotted as functions of distance through the crystal thickness (note that distance through the crystal , t/t_0, maps directly to the distance along the interface). Zones 1, 2, and 3 correspond to the flow regions identified in Figure 6.2b.

Figure 6.3a shows both concentration and tangential melt velocity across the entire thickness. In zone 1, the tangential melt velocity peaks at the ribbon tip (corresponding to the lowest solute concentration) and, as the influence of the Marangoni flow wanes, falls precipitously going through a local minimum (giving rise to a small local maximum in solute concentration). The tangential melt flow is dominated by solidification flow and nearly constant through zone 2, and the solute level is also nearly constant. There is dramatic change in zone 3, and the details of both profiles are shown over an expanded distance scale in Figure 6.3b. The counter-clockwise rotating Marangoni flow cell, generated by the lower meniscus, produces significant mixing of the solute in the melt (see also the local concentration field depicted in Figure 6.1c). The complicated shape of the concentration profile in zone 3 can directly be explained by the underlying tangential melt flow. As the solidification flow in zone 2 transitions into the Marangoni flow cell in zone 3, it gives rise to a stagnation point and a corresponding local maximum in the concentration field. Beyond the flow stagnation point, the magnitude of the tangential flow in the rotating cell first increases and then decreases, and the solute concentration inversely tracks these changes, with a local minimum followed by a peak maximum.

6.3 Transient simulation

The time-dependent formulation of the thermal-capillary model (along with melt replenishment) is employed to follow the temporal evolution of carbon impurity redistribution, under similar operating conditions as in 6.2. The melt is assumed to have an uniform initial carbon concentration of c_0 under static operating condition, with a step change in pull rate, $V_P = 4.4$ cm/min, at time t=0. The evolution of concentration field near the interface region, shown in Figure 6.4, shows a rise in carbon levels at the interface due to the rejection of impurities with the progress of solidification and further accumulation in the lower meniscus region, conforming with the results from quasi-steady analysis and further elucidating the convective flow effects on impurity redistribution. Evolution of the impurity profiles along the top, centre and bottom portions of the crystal, plotted in Figure 6.5, indicate longer transients along the bottom portion of the crystal due to the cumulative effect of the transported rejected impurities by the solidification flow towards the lower meniscus region.

6.4 Effect of solute properties

The equilibrium partition coefficient, k, dictates the incorporation of the solute into the crystal at the interface; see eqns. (6.2) and (6.3). Most impurities of interest for silicon, except for oxygen, have partition coefficients less than unity, so segregation results in the rejection of the solute at the growth interface. The redistribution of the rejected solute via diffusion and convection in the melt results in a non-homogeneous distribution of the solute through the grown crystal. Figure 6.6 shows the solute concentration profile through the ribbon thickness under steady-state HRG growth for several different values of the partition coefficient, with all other parameters unchanged from the base case. As k approaches unity, less solute is rejected and there is less redistribution across the growth interface. Thus, compared to the base case of $k = 0.07$, the solute concentration profile becomes more uniform for $k = 0.7$. For smaller values of the partition coefficient,

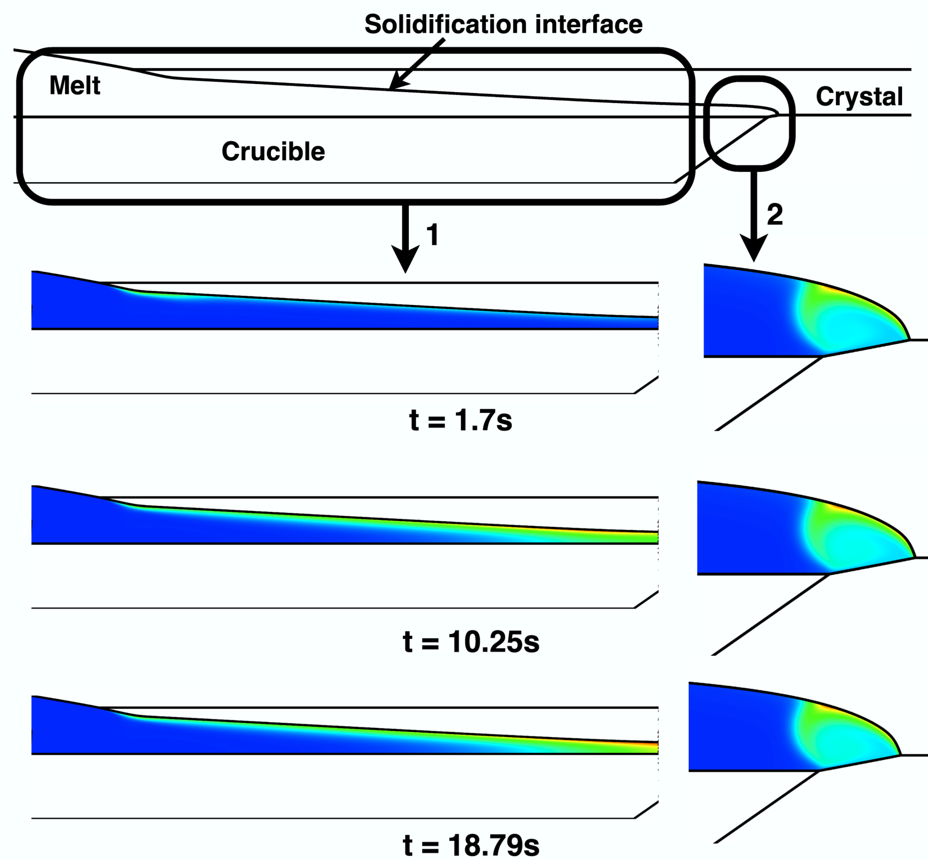

Figure 6.4: Temporal evolution of the concentration field near the solidification interface region: t = 1.7s - 1. Max $c = 4.05c_0$, Min $c = c_0$ 2. Max $c = 18.2c_0$, Min $c = 1.08c_0$; t= 10.25 s - 1. Max $c = 4.2c_0$, Min $c = c_0$ 2. Max $c = 60.7c_0$, Min $c = 2.68c_0$; t = 18.79s - 1. Max $c = 4.35c_0$, Min $c = c_0$ 2. Max $c = 94.2c_0$, Min $c = 3.64c_0$

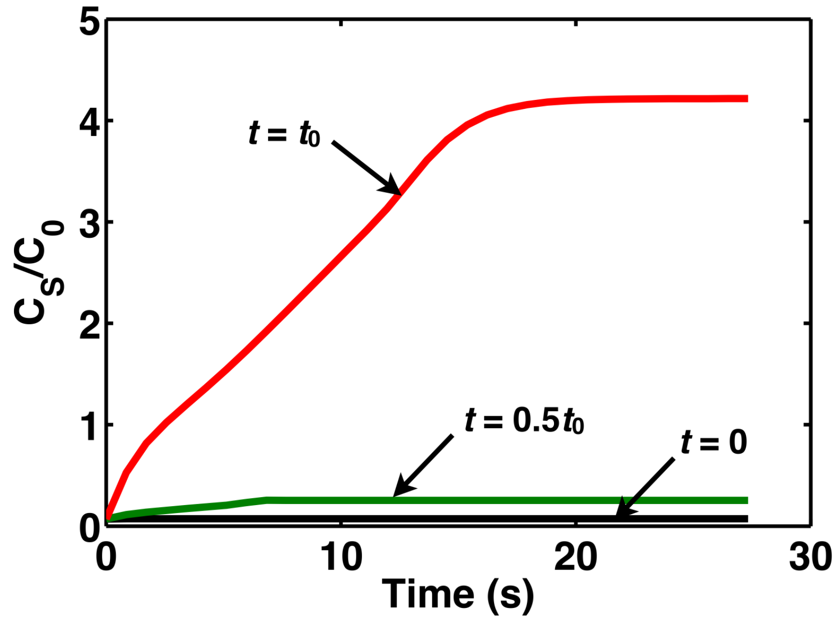

Figure 6.5: Temporal evolution of the impurity profile at various crystal portions along $t = 0$(top), $t = t_0/2$(center) and $t = t_0$(bottom)

the non-uniformity of the solute profile is magnified, as evidenced by the $k = 0.007$ case shown in Figure 6.6.

The diffusivity of the solute in the melt, D, affects the balance between diffusion and convection during growth and segregation, thus affecting the solute concentration profile in the ribbon. Figure 6.7 shows steady-state solute concentration profiles in the crystal, for solutes with different diffusivities in the melt (all for the case of $k = 0.07$ and the base case parameters). Faster diffusion (as occurs for larger diffusivities) in the melt acts to counter the redistribution driven by convection and results in smoother, more uniform concentration profiles in the crystal.

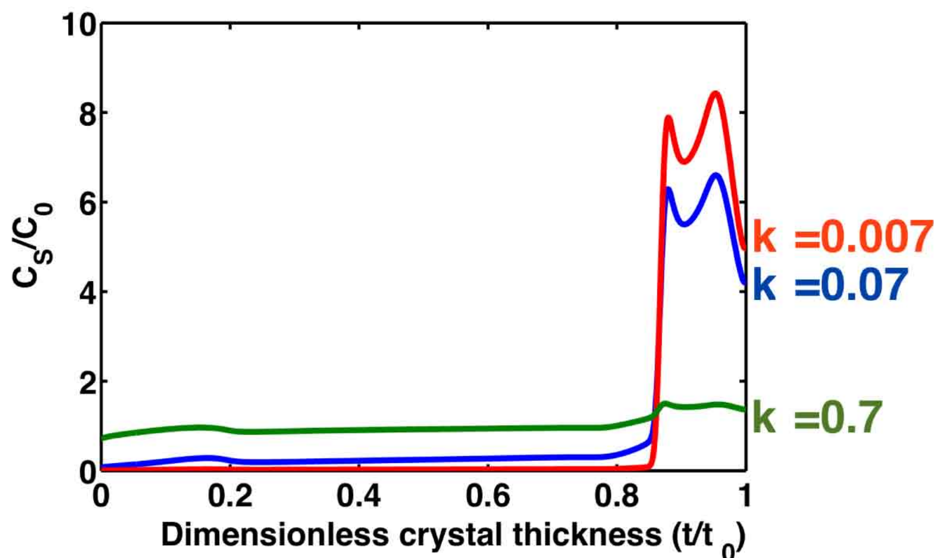

Figure 6.6: Solute concentration is plotted as a function of crystal thickness for different equilibrium partition coefficients.

6.5 Effect of pull rate

Figure 6.8a shows effects of the pull rate, V_g, on the steady-state solute concentration profile through the ribbon thickness, when all other parameters remain fixed at those used in the base case. A faster pull rate results in a faster rate of solidification and more solute rejection at the interface. In addition, a faster pull rate drives a stronger solidification flow in zone 2, which more strongly sweeps the rejected solute towards zone 3, thereby further elevating the accumulated levels of impurities in the lower meniscus region. As a result, faster pull rates result in a higher maximum concentration in the ribbon, and this maximum is shifted toward the bottom of the ribbon. The increase in maximum concentration scales nonlinearly with pull rate, as shown by a plot of maximum to minimum concentrations in the crystal versus pull rate in Figure 6.8b.

In addition to the increase in concentration maximum, both of the faster pull rates considered here change the shape of the solute profile through the ribbon, as seen by

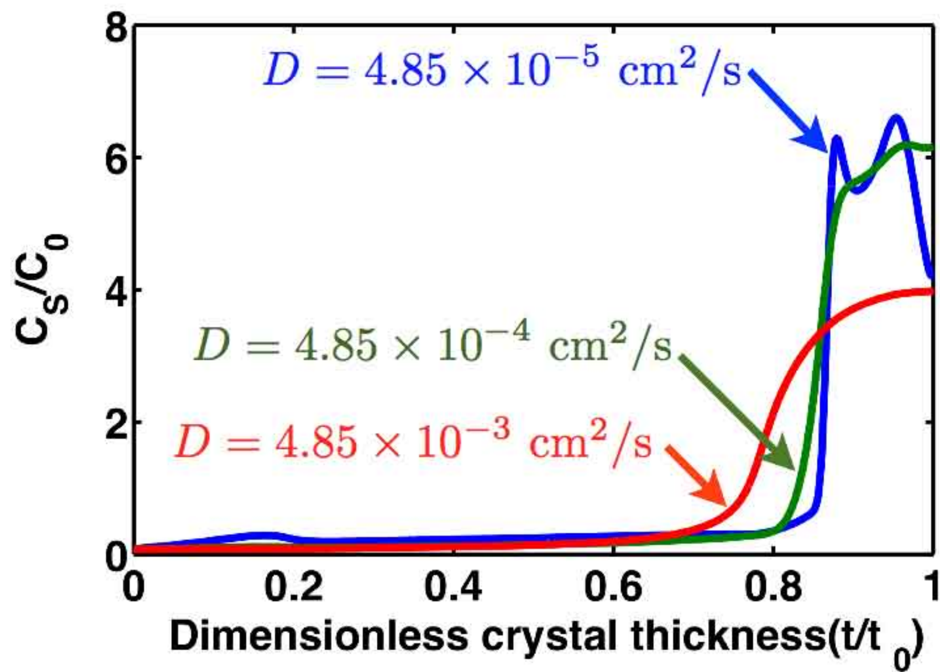

Figure 6.7: Solute concentration is plotted as a function of crystal thickness for different solute diffusion coefficients in the melt.

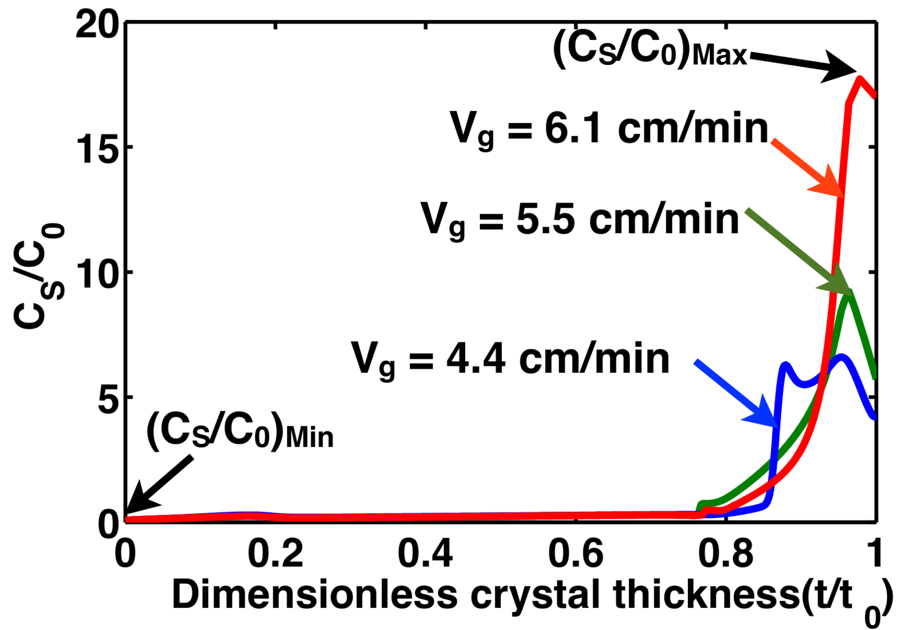

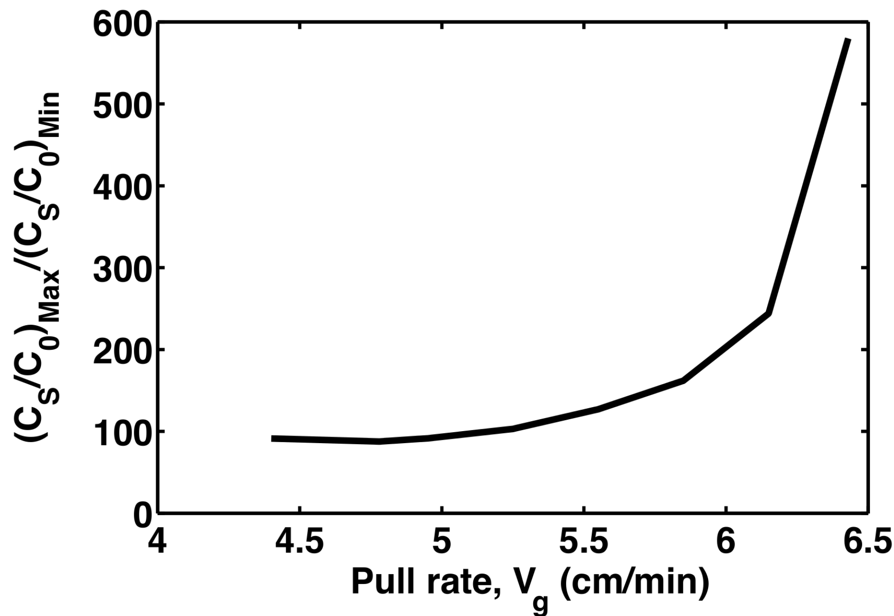

Figure 6.8: (a) Solute concentration is plotted as a function of crystal thickness for three different pull rates (b) The ratio of maximum to minimum solute concentration in grown crystal, which signifies the extent of redistribution, is plotted as a function of pull rate.

the by the disappearance of the double-peaked profile that appears for the base case of $V_g = 4.4$ cm/min in Figure 6.8a. This effect is explained by an elongation of the lower meniscus and a corresponding increase in strength of the Marangoni vortex as pull rate is increased—effects that progressively smooth the concentration profile in zone 3.

6.6 Limiting behaviors for carbon segregation

Carbon is of particular interest in silicon ribbon growth systems. In particular, dissolution of the graphite die used in vertical EFG systems results in very high levels of carbon incorporation into the ribbon [55, 112, 65] and also leads to problems caused by silicon carbide particles that nucleate in regions of the melt that are supersaturated with carbon [114]. Here, we apply our thermal-capillary model to consider two wall interaction behaviors to investigate limiting carbon segregation cases in the HRG process.

Our original base case, discussed previously in Section 6.2, presented the scenario where the impurity does not interact with the crucible walls. In this case, a no-flux boundary condition, corresponding to eqn. (6.4), was applied along all walls and menisci, and the concentration of impurity, c_0, was specified in the replenishment flow into the crucible via eqn. (6.5). Using a partition coefficient of $k = 0.07$, which is representative of that for carbon, the predicted composition of carbon in the ribbon was shown in Figure 6.2a. The other limiting case to be considered here corresponds to rapid and complete reaction of silicon with a graphite crucible, giving rise to a saturation condition at the crucible wall. This is accomplished by applying the no-flux condition along the menisci, eqn. (6.6), with an assumption of a constant carbon saturation level, with $c_0 = c_{sat}$, along every portion of crucible wall, as represented by eqn. (6.7). Note that we do not account for the possibility of silicon carbide particle nucleation in supersaturated melt.

Figure 6.9 compares the melt concentration fields for these two cases. The case of the non-interacting crucible is shown in Figure 6.9a, while that for the case of saturated

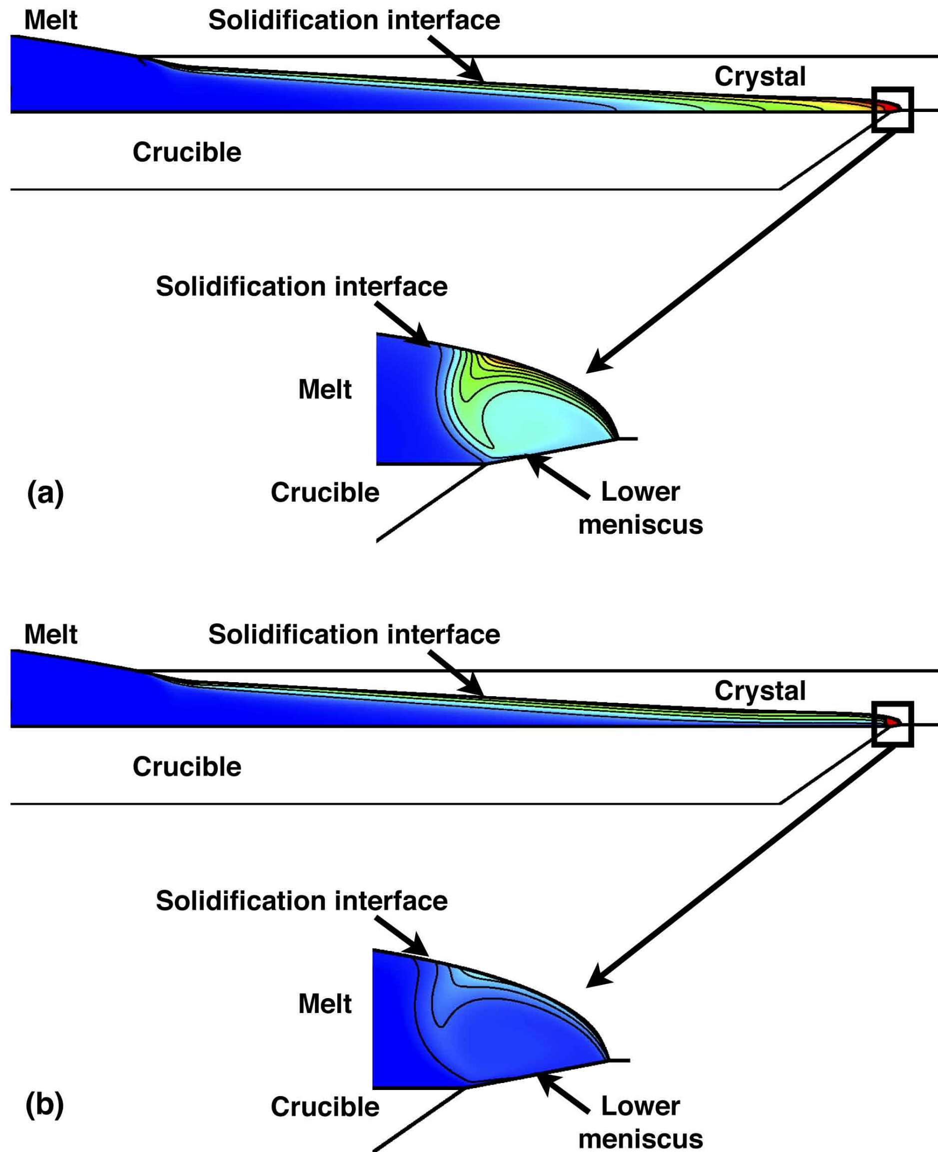

Figure 6.9: (a) Carbon redistribution for the case of the non-interacting crucible. Above: Concentration field in the melt near the solidification interface; maximum concentration is $c_{max} = 4.52c_0$, minimum concentration is $c_{min} = c_0$, and contour spacing is $\Delta c = 0.58c_0$. Below: Melt composition near lower meniscus; maximum concentration is $c_{max} = 94.3c_0$, minimum concentration is $c_{min} = 3.64c_0$, and contour spacing is $\Delta c = 5.5c_0$. (b) Carbon redistribution for the case of the crucible wall at saturation. Above: Concentration field in the melt near the solidification interface; maximum concentration is $c_{max} = 4.52c_{sat}$, minimum concentration is $c_{min} = c_{sat}$, and contour spacing is $\Delta c = 0.58c_{sat}$. Below: Melt composition near lower meniscus; maximum concentration is $c_{max} = 28.8c_{sat}$, minimum concentration is $c_{min} = 3.64c_{sat}$, and contour spacing is $\Delta c = 5.5c_{sat}$.

crucible walls is shown in Figure 6.9(b). Note that the color scales in these plots are arbitrary and meant only to convey the form of the concentration fields through the melt. The major difference in these fields is shown by the behavior of the diffusion layer under the crystal, particularly from about two-thirds of the distance from the tip to the end of the interface near the lower meniscus. In the non-interacting crucible case, the solute concentration contours curve at the lower crucible surface, reflecting the no-flux condition, and the overall carbon concentration increases as solute is trapped under the interface. The saturation condition keeps the melt composition much more uniform in the interacting crucible case, since $c_0 = c_{sat}$ is enforced along the crucible surface. In fact, under this worst-case scenario, the melt becomes supersaturated as carbon is rejected from the growing crystal. As carbon continues to accumulate under the interface, the saturation condition implies that carbon is actually being deposited onto the crucible wall from the melt under the growing crystal. In both cases, the Marangoni flow along the lower meniscus mixes the impurity near the bottom of the ribbon.

Figure 6.10 compares the predicted compositional profile for these two cases. Here, we have arbitrarily chosen the inlet composition of the melt for the non-interacting, no-flux case to be $c_0 = 0.1c_{sat}$, reflecting a case where carbon contamination is low in the melt, as might be the case when a silica liner is used. Any other inlet concentration will simply scale the existing curve accordingly. The case of the saturated walls, labeled $c = c_{sat}$ in the plot, indicates very high levels of carbon in the ribbon. The concentration profiles for both cases display very nearly the same shape, with relatively uniform levels across much of the thickness, accompanied by a much larger increase in the bottom portion of the ribbon.

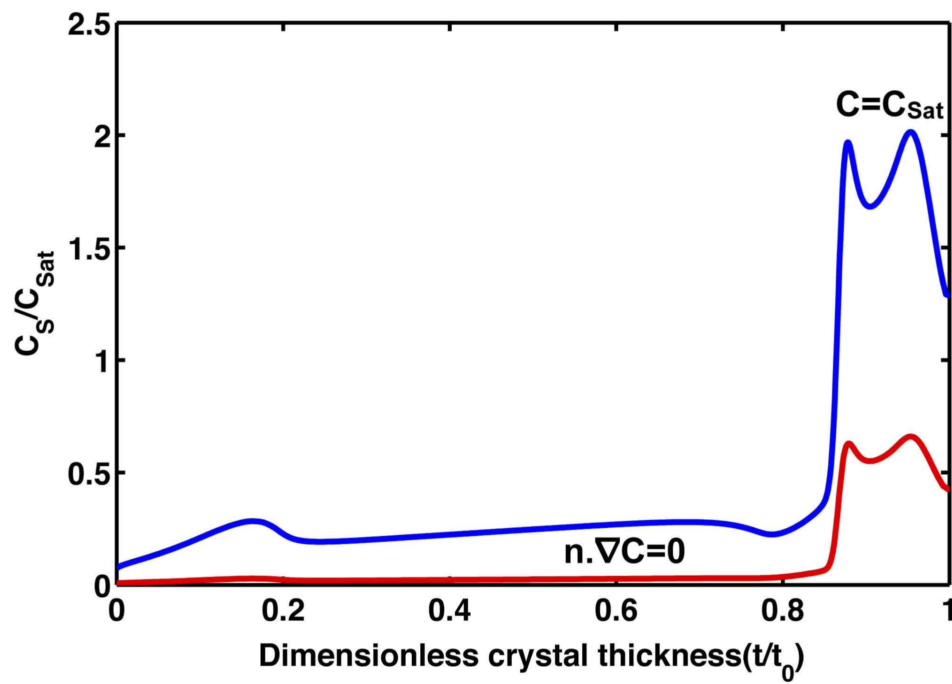

Figure 6.10: Carbon impurity concentration profile across the ribbon thickness for the limiting cases of a non-interacting crucible and a crucible at the saturation limit, labeled as $\mathbf{n} \cdot \nabla \mathbf{c} = \mathbf{0}$ and $c = c_{sat}$, respectively.

6.7 Conclusions

We have computed solute segregation and crystal composition expected for the steady-state operation of the horizontal ribbon growth of silicon. The redistribution of solute into the growing ribbon reveals a surprisingly non-uniform pattern. The solute level in the upper portion of the ribbon is relatively uniform, while lower portion of ribbon is significantly enriched. Under the base-case conditions considered here, over 75% of the total amount of solute in the ribbon is concentrated in the bottom 13% of the crystal thickness.

This redistribution is explained by convective flow patterns in the melt adjacent to the solidification interface. Along most of the interface, the melt flows horizontally, in the same direction as pulling and driven by the density difference between solid and liquid. However, with the deeply wedge-shaped crystal, the growth interface is nearly horizontal and the diffusion layer caused by solute segregation is oriented nearly vertically. The direction of the convective flux driven by the horizontal crystallization flow is nearly orthogonal to the direction of diffusion, thus very little impact is seen on segregation along most of the interface and the composition of the growing crystal is nearly uniform. However, the slight wedge angle does allow some rejected solute to be swept toward the lower meniscus, and the Marangoni vortex along that meniscus mixes the accumulated solute, giving rise to a sharp rise in concentration at the bottom of the ribbon.

Changes in distribution coefficient and solute diffusivity in the melt have expected outcomes. Namely, the solute distribution throughout the melt and grown crystal become more homogeneous as the distribution coefficient approaches unity and for higher values of melt diffusion coefficient. More interestingly, solute redistribution becomes progressively more inhomogeneous as the pull rate is increased. The nonlinear increase of c_{max}/c_{min} in the crystal with pull rate reflects the corresponding nonlinear changes in crystal thickness, lower meniscus length, and Marangoni flows that arise at higher

pull rates.

Paradoxically, the significant inhomogeneity of the ribbon composition that results from segregation may be an advantage of the HRG system. Namely, the upper portion of the grown ribbon is very uniform in composition, and most of the segregated solute is deposited in the bottom portion of the crystal. A device fabricated on the top side of the ribbon should benefit from the superior electrical characteristics of this relatively uniform region. Alternatively, impurities will preferentially segregate to the bottom portion of the crystal. This region, with enhanced impurity levels, may be removed during the post-growth processing operations; however, this would result in kerf losses and associated decreases in yield.

Specifically with respect to carbon, limiting-case computations show possibly beneficial behaviors. For the case of a non-interacting crucible, low carbon levels are expected for the ribbon as long as inlet contamination is low (and other paths for carbon incorporation into the melt are minimized). For growth from a carbon crucible without a liner, supersaturation will occur in the melt due to crucible dissolution and carbon rejection at the solidification interface. Similar to EFG processes [113, 114, 65], we would expect silicon carbide particles to nucleate under such conditions. Particles would be expected to interfere primarily near the lower meniscus, where carbon supersaturation is highest and where they would be swept by melt flow. This outcome is potentially less damaging than the plugging of the capillary flow channel in the die of vertical EFG processes by SiC particles [114]. In addition, the above-discussed, inhomogeneous segregation patterns will purify the upper portion of the grown ribbon with respect to carbon contamination. Further analyses are needed to more fully ascertain the behavior of carbon incorporation in a real HRG system.

Computational modeling has provided and will continue to provide a more complete understanding of the horizontal ribbon growth process. We believe that such approaches, combined with rational experiments, will provide a path to develop and optimize this process.

Chapter 7

Concluding Remarks

7.1 Thesis summary

The goal of the research presented in this thesis is directed at advancing the design of ribbon growth processes for solar silicon wafer production, and help these techniques compete with the conventional crystal growth processes. Vertical Ribbon Growth (VRG) techniques emerged in the market primarily to bypass the uneconomical kerf losses associated with ingot techniques such as Czochralski. However, these techniques could not succeed in the market due to slow material production rates and poor quality of the crystal, as they suffer from high levels of impurity contamination and large thermal stresses. Here, we assessed the potential of the Horizontal Ribbon Growth (HRG) process that promises to overcome many of the limitations inherent to VRG techniques. Despite ongoing research efforts since 1970, there has been little to no success towards commercializing the technique due to a host of challenges that disrupt the stable operation of the HRG process. Through computational modeling of the continuum transport processes, we developed a fundamental understanding of these failure modes and provided insights into evolving a design that can counter such effects.

In Chapter 2, we described the development of a rigorous thermal-capillary model to

study the coupled phenomena of heat transfer and interfacial phenomena (solidification and capillarity) in the HRG process. This model accounts for heat transfer in the melt-crystal-crucible domains with radiative heat loss from high temperature surfaces, melt convection due to buoyancy and surface-tension forces, and the self-consistent determination of melt-crystal, melt-ambient and crystal-ambient interface shapes. The model is implemented through a finite element based in-house software, Cats2D, and details of the solution procedure are presented in Chapter 3

In chapter 4, we applied the thermal-capillary model to a base-case HRG system to reveal its salient features. By employing a combination of active cooling at the solidifying tip, a cantilevered crucible shelf extension, and an after-heater, the model results demonstrated the formation of an extended wedge shaped solidification interface. This feature enabled the HRG system to dissipate latent heat from the interface primarily in a direction perpendicular to the pulling direction of the ribbon, allowing the system to achieve substantially faster growth rates under lower thermal gradients. In addition, the model also revealed existence of strong flows driven by the Marangoni and buoyancy forces as well as determine the shapes of upper and lower menisci that in effect shape the growing ribbon.

One of the significant predictions of the model is the non-linear bifurcation behavior of ribbon thickness with respect to pull rate, with the existence of multiple branches of solution and a limiting point beyond which quasi-steady solutions do not exist. Through transient analysis of states along both solution branches, we demonstrated that one branch represents operating states that are temporally stable to disturbances, while the other solution branch is made up of unstable states. Our analyses also indicated that the likely failure mechanism for the unstable states is a breakage of the lower meniscus, a result that is consistent with one of the failure mechanisms reported in HRG experiments [14]. Finally, we demonstrated that suitable system design changes that promote a more extended solidification interface, with a correspondingly greater wedge factor, shift the growth rate limit point to larger values and allow for stable growth at faster rates.

In chapter 5, we further explored instabilities and failure mechanisms of the HRG process with respect to several operating parameters. Significantly, our model predicted all of the major problems identified by Kudo[14]-bridging, spilling, and polycrystalline growth. Importantly, our analysis also revealed the physical mechanisms underlying these limits and additional interactions among other parameters that may limit the attainment of stable growth states. We predicted an operating window that is bounded at low growth rates by crystal-crucible freezing (bridging) and at higher growth rates by the underlying limit point of the steady-state solutions, the violation of the Gibbs limit for the lower meniscus (resulting in spilling of the melt), and the melt undercooling phenomenon (which will result in polycrystalline growth at the ribbon tip). We believe that these mechanisms that limit system operation will be generic to all HRG systems. Other analyses presented here show that growth limits are also encountered by changes in other operating parameters, such as pull angle and melt height. The ambient temperature of the heaters and coolers, such as cantilever shelf heater, crucible heater, after heater, and passive radiative coolers, are also found to give rise to similar operating windows.

In chapter 6, the thermal-capillary model is coupled with a solute transport model, accounting for convection and diffusion mechanisms in melt and segregation phenomenon at the interface, to predict the composition of the growing crystal. The redistribution of solute into the growing ribbon reveals a surprisingly non-uniform pattern with the solute level in the upper portion of the ribbon relatively uniform, while lower portion of ribbon is significantly enriched. This redistribution is explained by convective flow patterns in the melt adjacent to the solidification interface. Changes in distribution coefficient and solute diffusivity in the melt have expected outcomes. Namely, the solute distribution throughout the melt and grown crystal become more homogeneous as the distribution coefficient approaches unity and for higher values of melt diffusion coefficient. More interestingly, solute redistribution becomes progressively more inhomogeneous as the pull

rate is increased. Paradoxically, the significant inhomogeneity of the ribbon composition that results from segregation may be an advantage of the HRG system. Namely, the upper portion of the grown ribbon is very uniform in composition, and most of the segregated solute is deposited in the bottom portion of the crystal. A device fabricated on the top side of the ribbon should benefit from the superior electrical characteristics of this relatively uniform region. Alternatively, impurities will preferentially segregate to the bottom portion of the crystal. This region, with enhanced impurity levels, may be removed during the post-growth processing operations; however, this would result in kerf losses and associated decreases in yield.

7.2 Directions for future research

7.2.1 Coupled global modeling

The local thermal-capillary model, implemented by our in-house Cats2D software, accurately represents heat transfer, melt flow and the complicated dynamics and interactions of the various interfaces involved in the local HRG system (comprised of melt, crystal and the crucible). It, however, treats furnace heat transfer in an idealized fashion by modeling radiation to a specified ambient temperature using the Stefan-Boltzmann law. Such idealizations can limit the reliability of the quantitative model predictions and does not provide insights into designing an industrial furnace that can achieve HRG configuration.

A rigorous furnace heat transfer model should calculate radiative heat exchange between high temperature surfaces according to the enclosure theory making use of diffuse-grey approximation [122]. Within the enclosure, radiation from a surface to all other surfaces and radiation arriving from all other surfaces to a surface should be accounted for via the classical net radiation approach. These radiative fluxes between surfaces depend not only on the surface temperature and their radiation properites, but also on the geometry and how the surfaces view each other, as determined by the view

factors.

This inherently makes global modeling a multi-scale challenge with relevant length scales ranging from furnace dimensions (∼meters) to the characteristic length scales of the associated local transport phenomena (∼few hundred microns). A *monolithic* modeling approach attempts to represent all chosen physical phenomena spanning over the range of length scales in the entire domain in a single, large mathematical model [123]. This provides a mathematically self-consistent and algorithmically robust approach, however, is challenging to develop and program, tends to be computationally expensive, system specific and difficult to modify. Indeed several specialized codes have been developed for the global simulation of crystal growth systems and in particular CZ system, such as CGSim by STR Group Ltd. [124, 125, 126]; CrysMAS/STHAMAS from Fraunhofer Institute of Integrated Systems and Device Technology [127]; and FEMAG-CZ from FEMAGSoft S.A. [128, 129], which are commercially available for the industry. These codes model CZ system in an axisymmetric approximation and account for turbulent melt and gas convection in the rotating geometry; conjugated radiative, convective and conductive heat transport; release of the latent heat during solidification and crystal-melt interface deformations. While these commercial codes accurately represent furnace heat transfer, they do not treat the local thermal-capillary physics as rigorously as our in-house Cats2D software. Since these commercial codes do not offer the flexibility to implement additional physics by adding new mathematical models, we choose to rely on our in-house Cats2D software for local transport and capillary physics modeling.

An alternative approach is to partition the geometry into non-overlapping subdomains, each comprising of particular physical phenomena, and then solve each subdomain problem by employing existing specialized softwares well suited for the task. An appropriate coupling approach then needs to be adapted for the softwares to interact with each other at the interface of the subdomains. Such a *modular* coupling approach has also been adapted in several prior efforts to study melt crystal growth systems. Baumgartl *et al.* [130] applied temperature conditions from a global heat transport

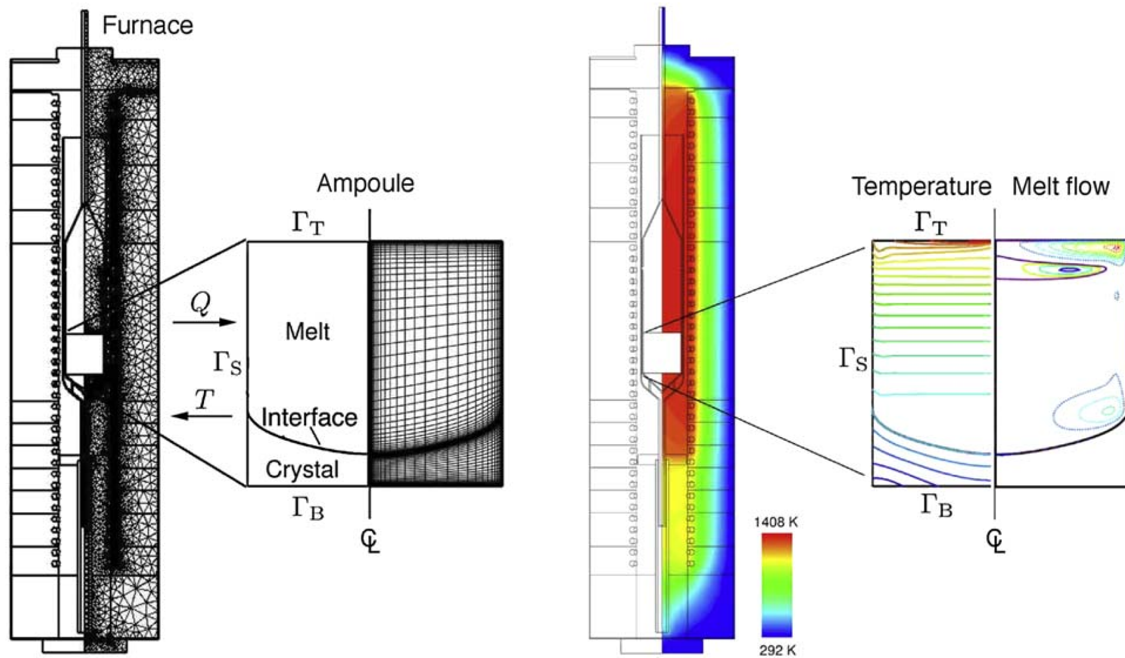

Figure 7.1: Melt crystal growth in an electrodynamic gradient freeze furnace is represented using coupled models. (a) Matching temperature and heat flux boundary conditions are exchanged between a finite volume furnace model and a finite element model of ampoule contents. (b) Temperature in the furnace is computed by CrysMAS, and temperature and melt flow in the ampoule are computed by Cats2D (adapted from [21])

simulation to compute melt convection in a Czochralski crystal growth process whereas Virbulis *et al.* [131] employed FEMAG and the commercial code CFD-ACE in a coupled manner to analyze silicon CZ flow. Lukanin *et al.* [132] described the coupling of a two-dimensional global heat transfer analysis with three-dimensional turbulent flow computations for silicon Czochralski growth. Yeckel *et al.* [133, 134] have also applied two-dimensional furnace heat transfer analyses to provide boundary conditions for three-dimensional local computations. However, all the aforementioned modeling efforts follow a one-way coupling approach by supplying the temperature boundary conditions borrowed from furnace heat transfer computations to the local model. This inherently ignores the effect of local factors such as melt convection and latent heat generation at the melt-crystal interface on the furnace heat load, thus necessitating the development of a two-way coupling approach for a fully self-consistent solution of the model.

Derby *et al.* [21, 135, 136, 137] presented a multi-scale model with two-way coupling to study crystal growth in an industrial electrodynamic gradient freeze furnace, shown in Fig 7.1. The furnace scale model is based on the commercial finite volume-based heat transfer analysis code CrysMAS, that is coupled to the local model in the growth ampoule handled by Cats2D code. Coupling is achieved by exchanging temperature and flux data between the codes in a way that enforces matching conditions at the coupling boundary between the subdomains. Such coupling poses significant challenges in terms of convergence, and Derby *et al.* have evaluated various iterative solution strategies for their convergence characteristics. Block Gauss-Seidel (BGS) iteration is a simple back-and-forth scheme where the furnace problem will be solved first subject to some initial conditions of temperature and flux along the coupling boundary and the updated values are passed to the ampoule subproblem. The iteration is then completed by solving the ampoule subproblem providing new estimates at the coupling boundary for the furnace subproblem and the procedure is repeated till convergence. However, this scheme is found to diverge in most cases and Derby *et al.* recommend using the Approximate Block Newton (ABN) scheme for more robust convergence. A detailed description of

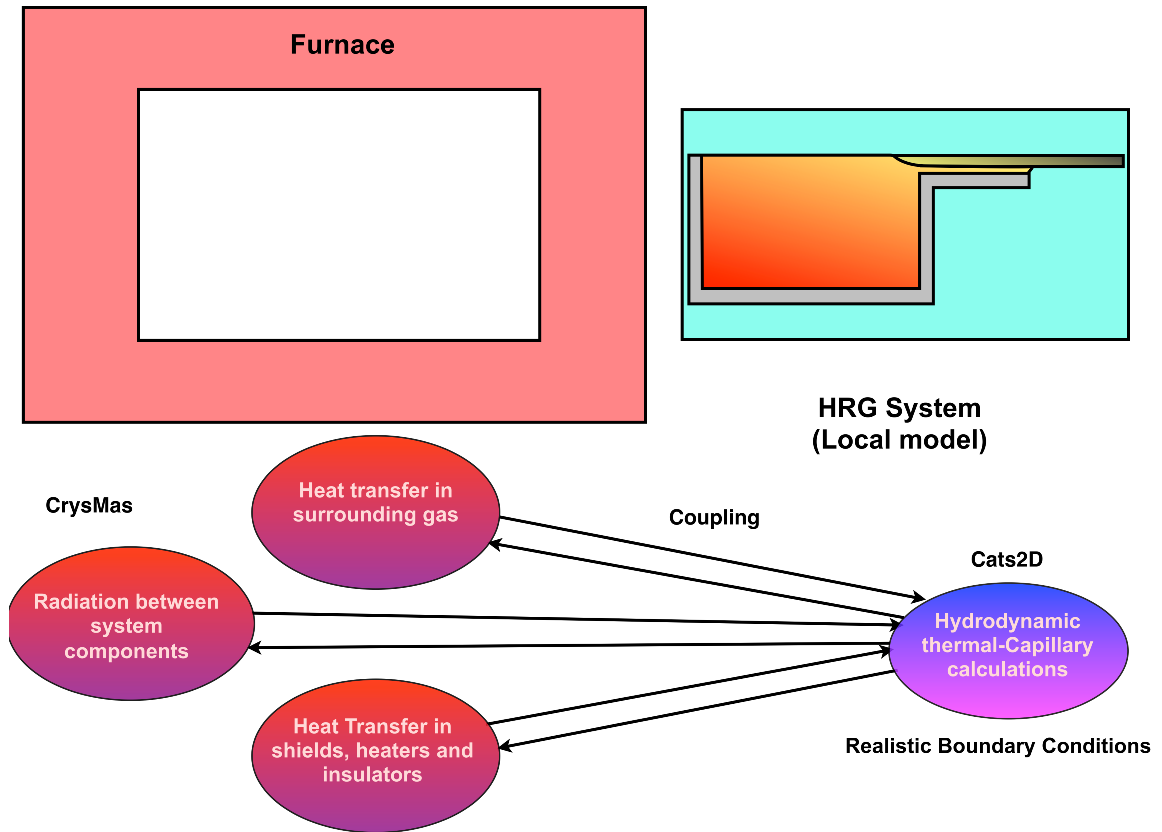

Figure 7.2: Schematic showing the division of the global system into subdomains comprising of the furnace design and the local HRG system. Furnace heat transfer will be modeled by the CrysMAS software while the local thermal-capillary physics will be modeled by the in-house Cats2D software with two-way modular coupling between the codes

the ABN iterative scheme and its implementation to couple any two black-box solvers is presented in [21, 135]. Such a coupling approach can further be developed and adopted to perform global modeling for designing an industrial scale HRG system. A schematic of the proposed coupling approach for the HRG system is shown in Fig 7.2.

7.2.2 Process instabilities

A deeper understanding of instabilities of the HRG system is essential to develop processing strategies that can ameliorate their effects, particularly the tip undercooling and lower meniscus instability mechanisms.

Tip undercooling

This is perhaps the most important of the process instabilities exhibited by the HRG process, since it is the first instability triggered by increasing growth rate. Achieving a sufficiently high growth rate is essential for reducing production costs. In addition, the mechanism driving this instability is puzzling. That undercooling of the melt arises as more latent heat is generated by faster growth is counterintuitive. A deeper understanding of the heat flows that lead to this phenomenon is essential. Future work needs to focus on understanding the fundamental mechanisms behind undercooling, and design strategies to minimize these effects should be pursued. The coupled model described earlier can be employed to assess strategies to change heat transfer via furnace design.

In addition, the mean curvature of the interface can influence the equilibrium thermodynamics of solidification, according to the Gibbs-Thomson effect, and the functional dependance follows as:

$$\frac{T_i}{T_{mp}} = 1 - \frac{\sigma_{sl}\mathcal{H}}{\rho_s \Delta H_f}, \tag{7.1}$$

where T_{mp} is the planar melting temperature of the material, $\mathcal{H}$ is the mean curvature of the interface, σ_{sl} is the surface energy of the interface, ρ_s is the density of the solid and

ΔH_f is the latent heat. Given that the tip region of the solidification interface in the HRG configuration exhibits significant curvature, the Gibbs-Thomson effect could have important ramifications of either augmenting or countering the undercooling instability. However, our current thermal-capillary model currently neglects this effect and needs to be accounted for by developing the model further.

Another approximation in the thermal-capillary model that needs to be revisited is that the melt-crystal interface lies along the equilibrium melting-point isotherm. This is a valid assumption so long as the solidification at the interface is not limited by kinetics, which is reasonable for most melt crystal growth systems. However, this assumption begins to break down at sufficiently high growth rates, typically greater than several meters per second for silicon; see, e.g, [138]. Based on past experiments, we expect the maximum growth velocities in the HRG system to be less than one meter per minute; nevertheless, solidification kinetics should still be carefully considered at the ribbon tip.

Melt spilling

The instability arising from Gibbs limit of pinning leads to a breakage or spill-over of the lower meniscus. This is the next mechanism, after tip undercooling, that limits the attaining of higher growth rates. Unlike tip undercooling, however, the mechanisms behind this instability are quite evident, having simply to do with geometry and wetting angles. Nevertheless, further computations need to be carried out to assess different design strategies to counter this limit.

First, the effect of equilibrium wetting angle and the shape of the lower crucible lip should be examined by considering the use of a crucible liner of different material and different crucible geometries. Further, the effects of pulling the crystal at an upward angle with respect to the melt can be considered, as was done in the low-angle silicon sheet (LASS) growth process [101, 102]. Changing the angle of pulling will change the apparent pinning angle of the relatively short lower meniscus thus affecting this instability. The model developed here can also be applied to asses the particularly

interesting design put forth by Varian Semiconductor Equipment, which employs a weir-like geometry that allows the silicon to spill continuously over the lower crucible lip [22]; see the process schematic in Fig 7.3 that shows the spilling and recirculation of liquid silicon.

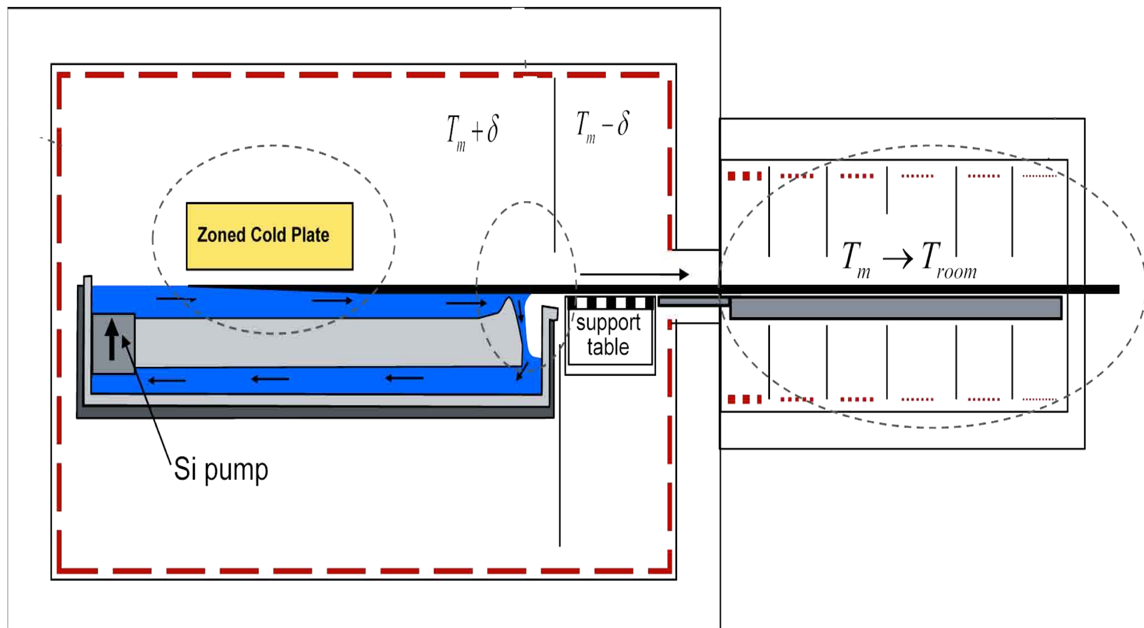

Figure 7.3: The Floating Silicon Method (FSM), under development of Varian Semiconductor Equipment, grows silicon ribbon in a horizontal orientation, from [22]

Morphological instabilities

Morphological instabilities can arise from rejected impurities at the solidification interface that, via the compositional dependence of the thermodynamic melting point, locally supercool the melt. This well-known phenomenon is known as constitutional supercooling, explained schematically in Fig 7.4. As discussed in Chapter 6, the local melt flow patterns near the solidification interface in the HRG system result in redistribution of impurities with a majority of the impurities being trapped in the lower meniscus

region. Although this has been presented as an inherent advantage of the process where a major portion of the growing crystal will be relatively free of impurities, it however, simultaneously presents a significant danger of constitutional supercooling due to high impurity concentrations in the lower meniscus region. New studies should be directed at predicting and understanding conditions under which a growing, stable melt-solid interface breaks down via constitutional supercooling to produce multi-crystalline material. Such conditions were studied in the earlier approximate model of HRG by Glicksman and Voorhees [68].

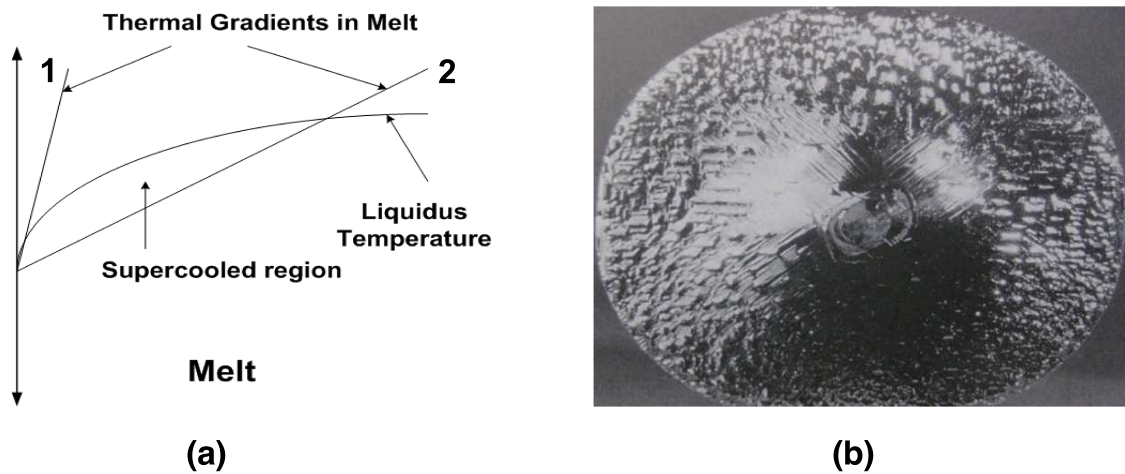

Figure 7.4: (a) Typical liquidus temperature distribution in the presence of impurities and thermal gradients in melt near the growth interface: Scenario 2 corresponds to shallow gradients with melt temperatures falling below the liquidus temperature resulting in supercooled region. (b) Cellular structures developed on the interface during melt crystal growth of Ga doped Ge under the conditions of morphological instability [23]

7.2.3 Thermal-stress analysis

As already mentioned, the evolution of ribbon growth technologies is severely challenged by the induced thermal stresses that deteriorate the quality of the growing crystal via plastic deformation, as well as promote fracture and buckling of the crystal. To alleviate

these adverse effects, it is essential to develop a better understanding of the nature of the thermal stresses in a ribbon growth environment. Several previous efforts were directed at studying such effects in the EFG growth, to varying degree of accuracies, ranging from simple thermo-elastic analytical and numerical approaches [52] to modeling growing silicon ribbon as a visco-plastic material [49, 51, 139, 140, 141].

Especially such an analysis will be critical for achieving higher growth rates in HRG system via the design of an efficient after-heater system to minimize thermal stresses upon cooling of the grown ribbon. We will address thermal stress via the calculation of linear elastic phenomena in the proposed research, and suitable after-heater designs will be put forth. Towards this end, reasonable progress has already been made in terms of model development and implementation which is summarized below, followed by directions for a more thorough analysis in the future.

Current progress

During the ribbon growth, non-uniform thermal gradients develop in the ribbon depending on the cooling mechanisms employed. As adjacent ribbon elements contract differently, proportional to their own temperature fall, they restrain each other's contraction giving rise to build up of thermal-stresses in the ribbon. The evolution of such stresses and displacements in the ribbon can be, to a first order approximation, modeled by the linear-elastic small deformation theory. Moreover, since the width dimension of the HRG ribbon is very large in comparison to its thickness, the problem can be treated satisfactorily by a two-dimensional plane strain approximation. Plane strain is defined to be a state of strain in which the normal strain to the plane as well as the shear strain components perpendicular to the plane are taken to be zero. Alternatively, this corresponds to a state in which the applied loads act in the plane and do not vary in the direction perpendicular to the plane (width dimension), while there can exist a non-zero out of plane resultant stress component. With these treatments, given a temperature field, it is possible to calculate thermal stresses for a linear-elastic solid, in

static equilibrium, according to the following equation:

$$\nabla \cdot (\nabla \mathbf{u}_d + (\nabla \mathbf{u}_d)^T) + (\mu \nabla \mathbf{u}_d - \epsilon (T - T_0)\mathbf{I}) = 0, \tag{7.2}$$

where $\mathbf{u}_d$ is the displacement vector, $\mu = 2\lambda/((1-2\lambda))$, $\epsilon = 2\beta(1+\lambda)/(1-2\lambda)$, λ is the Poisson's ratio, β is the thermal-expansion coefficient of silicon crystal, $\mathbf{I}$ is the identity tensor and T_0 is the reference temperature.

Despite continuous pulling of the ribbon, instantaneous development of the stress and displacement fields allow for a quasi-steady formulation of the problem. At the uptake end of the crystal, with an attached pulling mechanism, the displacements are constrained to be zero. The bottom surface of the growing ribbon is assumed to be supported on either a conveyer belt or rollers and the normal component of the displacement is constrained to be zero. Zero displacement condition is imposed on the solidification interface as it is constrained to be located along the melting point isotherm. The ribbon top surface is taken to be in a stress-free state. The numerical discretization of the governing equation and the solution process is analogous to that described in Chapter 3.

The thermal-stress analysis is performed on the base case system presented in chapter 4, with an applied pull rate of V_g =4.4 cm/min and with corresponding thermal gradients in the growing ribbon shown in Fig 4.4. The Poisson's ratio of the silicon crystal, λ, is assumed to be 0.25 , the thermal-expansion coefficient, β, is taken to be 4x10^{-6} K^{-1} and the modulus of elasticity, G, is 1.17x10^{11} N/m^2. The preliminary analysis conducted here suggests that the maximum stress occurs in the region where the two-dimensional temperature field near the solidification interface transitions into one-dimensional field in the rest of the crystal, as shown by the Von-Mises stress field depicted in Fig 7.5.

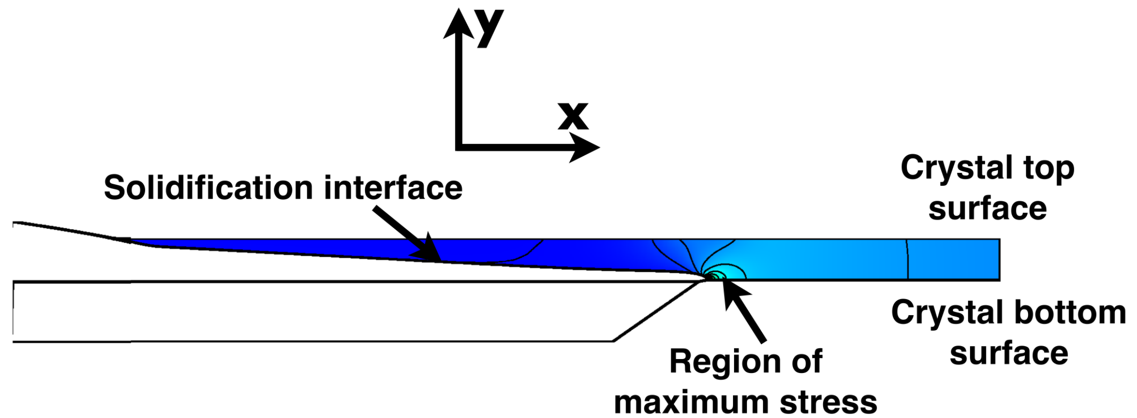

Figure 7.5: Von-Mises stress field in the crystal: Min σ/G = -3.04x10^{-5}, Max σ/G = 1.99x10^{-2}, $\Delta\sigma$/G = 9.9x10^{-4}

Future direction

The higher propensity of wider ribbons to undergo buckling remains one of the major impediments to promising growth of ribbon techniques [46, 50]. The wide ribbon effects, due to the presence of free surface ribbon edges, cannot be captured by the simple two-dimensional plane strain formulation developed earlier. However, in an EFG system, where thermal gradients are predominantly in the axial direction and reasonably negligible in the thickness direction, Gurtler *et al.* [52] were able to employ a linear-elastic two-dimensional plane stress formulation, in the plane perpendicular to the thickness direction, to study the edge effects in wide ribbons. By imposing thermal profiles that vary only along axial direction, their analysis showed that the stress distribution in the ribbon still evolves to present two-dimensional characteristics, varying in the width dimension, due to edge effects. In addition, they showed that the stress levels rise as the sheet width is increased. By applying elastic instability theory, they predicted that the critical stress for buckling falls with ribbon width and proposed hypothetical axial thermal profile designs that would alleviate such effects. However, such a plane stress

analysis cannot be directly applied to the HRG system as significant thermal gradients exist in the thickness direction, especially in the growth region, as discussed in Chapter 4. Thus, development of a three-dimensional thermal-stress model is essential, with thermal profiles borrowed from 2D thermal-capillary analysis, for a deeper understanding of thermal stress instabilities.

Further, it has been shown that silicon crystals undergo plastic deformation at high temperatures ($>1000^0$C) [142, 143] with relatively low yield stresses, and cannot be modeled as a perfectly elastic material during the ribbon growth process. During plastic deformation, residual thermal stresses in the crystal are relieved by the movement and multiplication of dislocations. This becomes an important issue since high residual stresses and dislocation densities diminish the performance and reliability of electronic devices. In the pioneering work of Haasen *et al.* [144, 145, 146] and Sumino *et al.* [147, 148] to describe the macroscopic plastic behavior of silicon crystals, they developed a model, based on experimental and theoretical considerations, that relates the stress-strain characteristics of the material to temperature, strain rate and the value of the dislocation density. By employing this model, where dislocation density becomes an internal variable, Tsai *et al.* [49, 51, 139, 140, 141] performed extensive analysis of EFG ribbons to optimize thermal profiles in the growing ribbon to minimize residual stresses and to restrain the evolution of dislocation densities. Such an analysis can be extended to predict dislocation densities in HRG ribbons. Pursuing the proposed research ideas here would significantly advance the design of the HRG system to achieve higher quality, wider ribbons at higher throughputs while mitigating the thermal-stress effects and instabilities.

References

[1] IRENA, Renewable energy technologies: Coat analysis series, Solar photovoltaics, Volume 1: Power sector, Issue 4/5, Tech. rep. (June, 2012).

[2] S. Mehta, P. Maycock, The PV supply chain: Manufacturing, technologies, costs, Tech. rep., Greentech Media Research and PV Energy Systems (1974).

[3] W. Zuhlehner, D. Huber, Czochralski grown silicon, in: Crystals 8, Springer-Verlag, Berlin, 1982.

[4] T. Hibiya, K. Hoshikawa, Silicon, in: P. Capper (Ed.), Bulk crystal growth of electronic, optical and optoelectronic materials, John Wiley & Sons, Ltd, Chichester, UK, 2005, pp. 1–42.

[5] H. J. Scheel, The development of crystal growth technology, in: H. J. Scheel, T. Fukuda (Eds.), Crystal growth technology, John Wiley & Sons, Ltd, Chichester, UK, 2004.

[6] P. Dold, Analysis of microsegregation in RF-heated float zone growth of silicon - comparison to the radiation-heated process, J. Crystal Growth 261 (2004) 1–10.

[7] PVTech, Solar shakeout: GT advanced technologies to exit DSS furnace business. URL http://www.pv-tech.org/news/solar_shakeout_gt_advanced_technologies_to_exit_dss_furnace_business

[8] ALGOR, Algor FEA helps engineers energize solar cells.
URL `http://www.algor.com/news_pub/cust_app/SPI_minicaster/default.asp`

[9] R. G. Seidensticker, R. H. Hopkins, Silicon ribbon growth by the dendritic web process, J. Crystal Growth 50 (1980) 221–235.

[10] J. I. Hanoka, An overview of silicon ribbon growth technology, Solar Energy Materials & Solar Cells 65 (2001) 231–237.

[11] H. E. Bates, D. N. Jewett, A. L. Mlavsky, V. E. White, Thick film silicon growth techniques, Tech. rep., Tyco Laboratories, Inc. (1974).

[12] B. H. Mackintosh, A. Seidl, M. Ouellette, B. Bathey, D. Yates, J. P. Kalejs, Large silicon crystal hollow-tube growth by the edge-defined film-fed growth(EFG) method, J. Cryst. Growth 287 (2006) 428–432.

[13] T. F. Ciszek, Edge-defined, film-fed growth(EFG) of silicon ribbons, Mat. Res. Bull. 7 (1972) 731–738.

[14] B. Kudo, Improvements in the horizontal ribbon growth technique for single crystal silicon, J. Cryst. Growth 50 (1980) 247–259.

[15] C. E. Bleil, A new method for growing crystal ribbons, J. Cryst. Growth 5 (1969) 99–104.

[16] A. Burgers, P. Manshanden, A. Gutjahr, L. Laas, A. Schöonecker, S. Seren, G. Hahn, Record 13% efficiency screen printed silicon solar cells on ribbon growth on substrate(RGS) material, in: Proceedings of the 21st European Photovoltaic Solar Energy Conference and Exhibition, 4-8 sep. 2006.

[17] J. S. Lee, B. Y. Jang, Y. S. Ahn, Effect of processing parameters on thickness of columnar structured silicon wafers directly grown from silicon melts, International Journal of Photoenergy 2012 (2011) 1–6.

[18] A. Yeckel, R. T. Goodwin, Cats2D (Crystallization and Transport Simulator) user manual (2010).
URL `http://www.msi.umn.edu/~yeckel/cats2d.html`

[19] J. A. Zoutendyk, Theoretical analysis of heat flow in horizontal ribbon growth from a melt, J. Appl. Phys. 49 (1978) 3927–3932.

[20] I. Steinbach, H. U. Hofs, Micro-structural analysis of the crystallization of silicon ribbons produced by the RGS process, in: Proceedings of 26th IEEE Photovoltaics Specialists Conference, 1997, pp. 91–93.

[21] A. Yeckel, L. Lun, J. J. Derby, Multi-scale crystal growth computations via an approximate block Newton method, J. Cryst. Growth. 312 (2010) 1463–1467.

[22] Floating Silicon Method (FSM), DOE Office of Energy Efficiency and Renewable Energy (EERE) grant to Varian Semiconductor Equipment Associates, Inc.

[23] D. T. J. Hurle, Crystal pulling from the melt, Springer Verlag, Berlin, 1993.

[24] N. S. Lewis, G. Crabtree, A. J. Nozik, M. R. Wasielewski, P. Alivisatos, Basic research needs for solar energy utilization: Report of the basic energy sciences workshop on solar energy utilization, office of Science, U. S. Department of Energy (2005).

[25] T. Surek, Crystal growth and materials research in photovoltaics: Progress and challenges, J. Cryst. Growth 275 (2005) 292–304.

[26] C. A. Wolden, J. Kurtin, J. B. Baxter, I. Repins, S. E. Shaheen, J. T. Torvik, A. A. Rockett, V. M. Fthenakis, E. S. Aydil, Photovoltaic manufacturing: Present status, future prospects and research needs, NSF PV Workshop 2010.

[27] Solarbuzz, Annual world PV market review, Tech. rep., Port Washington, NY (April, 2011).

[28] T. Surek, Progress in U.S.photovoltaics: Looking back 30 years and looking ahead 20, in: Proceedings of Third World Conference on Photovoltaic Energy Conversion, May 11-18, 2003, pp. Paper No. 8PL–E3–01.

[29] W. C. Dash, Growth of silicon crystals free from dislocations, J. Appl. Phys. 30 (1959) 459–475.

[30] P. Mints, Solar Ooutlook, Navigant Consulting (March 4, 2011).

[31] M. A. Green, K. Emery, Y. Hishikawa, W. Warta, E. D. Dunlop, Solar cell efficiency tables(version 41), Progress in Photovoltaics: Research and Applications 21 (2013) 1–11.

[32] D. Karg, G. Pensl, M. Schulz, C. Hössler, W. Koch, Oxygen-related defect centers in solar-grade, multi crystalline silicon. A reservoir of lifetime killers, Phys. Status Solidi(b) 222 (2000) 379.

[33] A. Rudevičs, A. Muižnieks, G. Ratnieks, A. Möuhlbauer, T. Wetzel, Numerical study of transient behaviour of molten zone during industrial FZ process for large silicon crystal growth, J. Crystal Growth 266 (2004) 54–59.

[34] M. A. Green, The path to 25% silicon solar cell efficiency: Hhistory of silicon cell evolution, Progress in photovoltaics: Rresearch and applications 17 (2009) 183–189.

[35] A. M. Whitepaper, Wafer wire sawing economics and total cost of ownership optimization (2011).

[36] H. J. Möller, C. Funke, M. Rhino, S. Scholz, Multicrystalline silicon for solar cells, Thin Solid Films 487 (2005) 179–187.

[37] A. D. Little, Proceedings of 16th European photovoltaic solar energy conference, James & James Ltd., London, 2000, p. 9.

[38] E. A. Alsema, M. J. de Wild-Scholten, Environmental life cycle assessment of advanced silicon solar cell technologies, in: Proceedings of 19th Eutopian photovoltaic solar energy conference, June 7-11, 2004, p. 840.

[39] S. N. Dermatis, J. J. W. Faust, Semiconductor sheets for the manufacture of semiconductor devices, IEEE Trans. Commun. Electron. 82 (1963) 94–98.

[40] T. F. Ciszek, Melt growth of crystalline silicon tubes by a capillary action shaping technique, phys. star. sol. (a) 32 (1975) 521–527.

[41] T. Surek, B. Chalmers, A. I. Mlavsky, The edge-defined film-fed growth of controlled shape crystals, J. Crystal Growth 42 (1977) 453–465.

[42] K. V. Ravi, The growth of EFG silicon ribbons, J. Crystal Growth 39 (1977) 1–16.

[43] J. Cao, EFG manufacturing line technical progress and module cost reductions under the PVMaT program, in: Proceedings of 26th IEEE PVSC, Anaheim, 1997, p. 1077.

[44] T. F. Ciszek, Techniques for the crystal growth of silicon ingots and ribbons, J. Cryst. Growth 66 (1984) 655–672.

[45] R. O. Bell, J. P. Kalejs, Growth of silicon sheets for photovoltaic applications, J. Mater. Res. 13 (1998) 2732–2739.

[46] J. P. Kalejs, B. H. Mackintosh, T. Surek, High speed EFG of wide silicon ribbon, J. Cryst. Growth 50 (1980) 175–192.

[47] J. Katcki, A review of structural defect generation mechanisms in EFG ribbons, J. Cryst. Growth 82 (1987) 197–202.

[48] I. Yonenaga, K. Sumino, Dislocation dynamics in the plastic deformation of silicon crystals, pys. star. sol. (a) 50 (1978) 685–693.

[49] O. W. Dillon, C. T. Tsai, R. J. D. Angelis, Dislocation dynamics during the growth of silicon ribbon, J. Appl. Phys. 60 (1986) 1784–1792.

[50] J. Kalejs, W. Schmidt, I. Schwirtlich, W. Hoffmann, Challenges for EFG ribbon technology on the path to large scale manufacturing, in: Photovoltaic Specialists Conference, 2005. Conference Record of the Thirty-first IEEE, 3-7 Jan. 2005, pp. 1301–1304.

[51] C. T. Tsai, J. O. W. Dillon, Dislocation dynamics and the viscoplastic buckling of dendrite web type silicon ribbon, J. Cryst. Growth 82 (1987) 695–708.

[52] R. W. Gurtler, Nature of thermal stresses and potential for reduced thermal buckling of thin silicon ribbon grown at high speed, J. Cryst. Growth 50 (1987) 695–708.

[53] A. Blake, Practical Stress Analysis in Engineering Design, CRC Press, 1989.

[54] C. V. H. N. Rao, M. C. Cretella, F. V. Wald, K. V. Ravi, Imperfections and impurities in EFG silicon ribbons, J. Crystal Growth 50 (1980) 311–319.

[55] H. J. . Möller, Carbon-induced twinning in multicrystalline silicon, Solid State Phenom. 95 (2003) 181–186.

[56] P. D. Thomas, R. A. Brown, Rate limits in silicon sheet growth: The connections between vertical and horizontal methods, J. Cryst. Growth 82 (1987) 1–9.

[57] W. Shockley, Process for growing single crystals, US patent 3031275 (1962).

[58] C. E. Bleil, Horizontal growth of crystal ribbons, US patent 3681033 (1972).

[59] B. Kudo, Lateral pulling growth of crystal ribbons, US patent 4226834 (1980).

[60] D. N. Jewett, H. E. Bates, J. W. Loher, in: J. Dismukes, E. Sirtl, P. Rai-Choudhury, L. P. Hunt (Eds.), Proc. 3rd Symp. on Materials and New Processing

Technologies for Photovoltaics, Electrochemical Society, Princeton, NJ, 1982, p. 320.

[61] S. Ranjan, S. Balaji, R. A. Panella, B. E. Ydstie, Silicon solar cell production, Computers & Chemical Engineering 35 (8) (2011) 1439 – 1453.

[62] H. Lange, I. A. Schwirtlich, Ribbon growth on substrate (RGS): A new approach to high speed growth of silicon ribbons for photovoltaics, J. Cryst. Growth 104 (1990) 108–112.

[63] T. Surek, Theory of shape stability in crystal growth from the melt, J. Appl. Phys. 47 (1976) 4384–4393.

[64] V. A. Tatarchenko, Capillary shaping in crystal growth from melts: I. Theory, J, Cryst. Growth 37 (1977) 272–284.

[65] J. P. Kalejs, Modeling contributions in commercialization of silicon ribbon growth from the melt, J. Cryst. Growth 230 (2001) 10–21.

[66] J. J. Derby, R. A. Brown, On the dynamics of czochralski crystal growth, J. Crystal Growth 83 (1987) 137–151.

[67] J. A. Zoutendyk, Analysis of forced convective heat flow effects in horizontal ribbon growth from the melt, J. Cryst. Growth. 50 (1980) 83–93.

[68] M. E. Glicksman, P. W. Voorhees, Analysis of morphologically stable horizontal ribbon growth, J. Electron. Mater. 12 (1983) 161–179.

[69] C. A. Rhodes, M. M. Sarraf, C. H. Liu, Investigation of the meniscus stability in horizontal crystal ribbon growth, J. Cryst. Growth. 50 (1980) 94–101.

[70] A. Yeckel, J. J. Derby, Computer modeling of crystal growth, in: Bulk crystal growth of electronic, optical and optoelectronic materials, John Wiley & Sons, West Sussex, UK, 2005, pp. 73–119.

[71] J. Derby, Modeling and bulk crystal growth processes: What is to be learned?, in: M. Wang, K. Tsukamoto, D. Wu (Eds.), Selected Topics on Crystal Growth: 14th International Summer School on Crystal Growth, Vol. 1270 of AIP Conference Proceedings, AIP, Melville, New York, 2010, pp. 221–246.

[72] N. Eustathopoulos, B. Drevet, S. Brandon, A. Virozub, Basic principles of capillarity in relation to crystal growth, in: T. Duffar (Ed.), Crystal Growth Processes Based on Capillarity: Czochralski, Floating Zone and Crucible Techniques, John Wiley & Sons, Ltd, New York, 2010, pp. 1–49.

[73] A. Virozub, I. G. Rasin, S. Brandon, Journal of Crystal Growth 310 (24) (2008) 5416 – 5422.

[74] H. A. Bumstead, Scientific papers of J. Willard Gibbs: Vol 1:Thermodynamics, Dover, New York, 1979.

[75] T. Surek, B. Chalmers, A. I. Mlavsky, The Edge-Defined Film-Fed Growth of controlled shape crystals, J. Crystal Growth 42 (1977) 453–465.

[76] B. Yanga, L. L. Zheng, B. Mackintosh, D. Yates, J. Kalejs, Meniscus dynamics and melt solidification in the EFG silicon tube growth process, J. Crystal Growth 293 (2006) 509–516.

[77] T. Surek, B. Chalmers, The direction of growth of the surface of a crystal in contact with its melt, J. Cryst. Growth. 29 (1975) 1–11.

[78] T. Surek, The meniscus angle in germanium crystal growth from melt, Scripta Met. 10 (1976) 425–431.

[79] P. M. Gresho, R. L. Sani, Incompressible flow and the finite element method, John Wilea and Sons, Inc., New York, 1998.

[80] T. J. R. Hughes, The finite element method: Lin ear static and dynamic finite element analysis, Dover, New York, 2000.

[81] J. N. Reddy, An Introduction to the Finite Element Method, McGraw Hill Eduration, New York, 2005.

[82] B. A. Finlayson, L. E. Scriven, The method of weighted residuals and its relation to certain variational principles for the analysis of transport processes, Chem. Eng. Sci. 20 (1965) 395–404.

[83] A. Jeffrey, Handbook of mathematical formulas and integrals, Academic Press, New York, 1995.

[84] J. M. de Santos, Two-phase cocurrent downflow through constricted passages, Ph.D. thesis, University of Minnesota (1991).

[85] J. F. Thompson, Z. U. A. Warsi, C. W. Mastin, Numerical grid generation, Elsevier, New York, 1985.

[86] P. Hood, Frontal solution program for unsymmetric matrices, Int. J. Numer. Methods. Eng. 10 (1976) 379–399.

[87] H. B. Keller, Applications of bifurcation theory, Academic Press, New York, 1995.

[88] L. C. Musson, Two-layer slot coating, Ph.D. thesis, University of Minnesota (2001).

[89] B. Chalmers, High speed growth of sheet crystals, J. Cryst. Growth. 70 (1984) 3–10.

[90] H. M. Ettouney, R. A. Brown, J. P. Kalejs, Analysis of operating limits in Edge-defined Film-fed Growth, J. Cryst Growth. 62 (1983) 230–246.

[91] P. D. Thomas, H. M. Ettouney, R. A. Brown, A thermal-capillary mechanism for a growth rate limit in Edge-defined Film-fed Growth of silicon sheets, J. Cryst. Growth. 76 (1986) 339–351.

[92] H. M. Ettouney, R. A. Brown, J. P. Kalejs, Comparison of finite element calculations and experimental measurements in Edge-defined Film-fed Growth of silicon sheets, J. Cryst. Growth. 70 (1984) 306–313.

[93] P. D. Thomas, R. A. Brown, Rate limits in silicon sheet growth: the connections between vertical and horizontal methods, J. Cryst Growth. 82 (1987) 1–9.

[94] J. J. Derby, R. A. Brown, On the dynamics of Czochralski growth, J. Crystal Growth. 83 (1987) 137–151.

[95] W. Zhou, D. E. Bornside, R. A. Brown, Dynamic simulation of Czochralski crystal growth using an integrated thermal-capillary model, J. Cryst. Growth. 137 (1994) 26–31.

[96] J. J. Derby, L. J. Atherton, P. D. Thomas, R. A. Brown, Finite-element methods for analysis of the dynamics and control of Czochraski crystal growth, J. Sci. Computing 2 (1987) 297–343.

[97] G. Samanta, A. Yeckel, P. Daggolu, H. Fang, E. D. Bourret-Courchesne, J. J. Derby, Analysis of limits for sapphire growth in a micro-pulling-down system, J. Crystal Growth 335 (2011) 148–159.

[98] M. Apel, D. Franke, I. Steinbach, Simulation of the crystallization of silicon ribbons on substrate, Solar Energy Materials and Solar Cells 72 (2002) 201–208.

[99] P. Y. Pichon, Personal communication (2012).

[100] M. Tokairin, K. Fujiwara, K. Kutsukake, N. Usami, K. Nakajima, Formation mechanism of a faceted interface: in situ observation of the Si(100) crystalmelt interface during crystal growth, Physical Review B 80 80 (2009) 174108.

[101] H. Bates, D. N. Jewett, High rate growth of silicon ribbon by low angle crystal growth high rate growth of silicon ribbon by low angle crystal growth, in: Conference Record of the 16th IEEE photovoltaics specialists conference, Institute of Electrical and Electronics Engineers, Inc., New York, 1981, pp. 255–256.

[102] D. N. Jewett, H. E. Bates, J. W. Locher, Progress in growth of silicon ribbon by a low angle, high rate process, in: Conference Record of the 16th IEEE photovoltaics specialists conference, 1982.

[103] D. N. Jewett, M. A. Harverd, Method and apparatus for producing crystalline ribbons (1981).

[104] P. Daggolu, A. Yeckel, C. Bleil, J. Derby, Thermal-capillary analysis of the horizontal ribbon growth of silicon crystals, J. Cryst. Growth. 355 (2012) 129–139.

[105] P. Daggolu, A. Yeckel, C. Bleil, J. Derby, Stability limits for the horizontal ribbon growth of silicon crystals, J. Cryst. Growth. 363 (2013) 132–140.

[106] S. H. Park, D. K. Schroder, Deep-level impurities in edge-defined film-fed growth silicon, J. Appl. Phys. 78 (1995) 801–810.

[107] D. MacDonald, A. Cuevas, A. Kinomura, Y. Nakano, L. J. Geerligs, Transition metal profiles in a multicrystalline silicon ingot, J. Appl. Phys. 97 (2005) 033523.

[108] D. MacDonald, L. J. Geerligs, Recombination activity of iron and other transition metal point defects in n- and p-type crystalline silicon, Appl. Phys. Lett. 85 (2004) 4061.

[109] A. Istratov, T. Buonassisi, R. J. McDonald, A. R. Smith, R. Schindler, J. A. Rand, J. P. Kalejs, E. R. Weber, Metal content of multi crystalline silicon for solar cells and its impact on minority carrier diffusion length, J. Appl. Phys. 94 (2003) 6552.

[110] D. MacDonald, J. Tan, Impurities in solar-grade silicon, in: H. H. Tan, J. C. Chiao, L. Faraone, C. Jagadish, J. Williams, A. R. Wilson (Eds.), Devices and

process technologies for Microelectronics, MEMS, Photonics and Nnanotechnology IV, Proc. of SPIE, Vol. 6800, 2008, p. 7 pages.

[111] R. C. Newman, Defects in silicon, Rep. Prog. Phys. 45 (1982) 1163–1210.

[112] J. P. Kalejs, Impurity redistribution in EFG, J. Cryst. Growth. 44 (1978) 329–344.

[113] J. Cao, M. Prince, J. Kalejs, Impurity transients in multiple crystal growth from a single crucible for EFG silicon octagons, Journal of Crystal Growth 174 (1997) 170 – 175.

[114] S. Rajendran, M. Larrousse, B. Bathey, J. Kalejs, Silicon carbide control in the EFG system, Journal of Crystal Growth 128 (1993) 338 – 342.

[115] L. Braescu, S. Balint, L. Tanasie, Numerical studies concerning the dependence of the impurity distribution on the pulling rate and on the radius of the capillary channel in the case of a thin rod grown from the melt by edge-defined film-fed growth (EFG) method, Journal of Crystal Growth 291 (1) (2006) 52 – 59.

[116] L. Braescu, T. Duffar, Effect of buoyancy and marangoni forces on the dopant distribution in a single crystal fiber grown from the melt by edge-defined film-fed growth (EFG) method, Journal of Crystal Growth 310 (2) (2008) 484 – 489.

[117] O. Smirnova, V. Kalaev, A. Seidl, B. Birkmann, 3D unsteady analysis of melt flow and segregation during EFG Si crystal growth, Journal of Crystal Growth 310 (2008) 2209 – 2214.

[118] B. Gao, K. Kakimoto, Global simulation of coupled carbon and oxygen transport in a czochralski furnace for silicon crystal growth, Journal of Crystal Growth 312 (20) (2010) 2972 – 2976.

[119] T. Nozaki, Y. Yatsurugi, N. Akiyama, Concentration and behavior of carbon in semiconductor silicon, J. Electrochem. Soc. 117 (1970) 1566–1568.

[120] G. G. Gnesin, A. I. Raichenko, Kinetics of the liquid-phase reactive sintering of silicon carbide, Soviet Powder Metallurgy and Metal Ceramics 12 (1973) 383–389.

[121] J. A. Burton, R. C. Prim, W. P. Slichter, The distribution of solute in crystals grown from the melt. part I. Theoretical, J. Chem. Phys. 21 (1953) 1987–1991.

[122] R. Siegel, J. R. Howell, Thermal radiation heat transfer, Hemisphere Publishing Corporation, Washington, 1992.

[123] M. Cervera, R. Codina, M. Galindo, On the computational efficiency and implementation of block-iterative algorithms for nonlinear coupled problems, Eng. Comput. 13 (1996) 4–30.

[124] V. Kalaev, I. Evstratov, Y. Makarov, Gas flow effect on global heat transport and melt convection in Czochralski silicon growth, J. Cryst. Growth. 249 (2003) 87–99.

[125] Y. Y. Teng, J. C. Chen, C. W. Lu, C. Huang, W. Wun, H. Chen, C. Chen, W. C. Lan, Numerical simulation of the effect of heater position on the oxygen concentration in the CZ silicon crystal growth process,, International Journal of Photoenergy 2012 (2012) 395235.

[126] J. C. Chen, Y. Y. Teng, W. T. Wun, C. W. Lu, H. Chen, C. Y. Chen, W. C. Lan, Numerical simulation of oxygen transport during the CZ silicon crystal growth process, J. Cryst. Growth. 318 (2011) 318–323.

[127] L. Huang, P. Lee, C. Hsieh, W. Hsu, C. Lan, On the hot-zone design of Czochralski silicon growth for photovoltaic applications, J. Cryst. Growth. 261 (2004) 433–443.

[128] K. Takano, Y. Shiraishi, J. Matsubara, T. Iida, N. Takase, N. Machida, M. Kuramoto, H. Yamagishi, Global simulation of the CZ silicon crystal growth up to 400 mm in diameter,, J. Cryst. Growth. 229 (2001) 26–30.

[129] D. Song, S. Lee, Y. Mun, H. Kim, Oxygen content increasing mechanism in Czochralski silicon crystals doped with heavy antimony under a double- typed heat shield, J. Cryst. Growth. 325 (2011) 27–31.

[130] J. Baumgartl, A. Bune, K. Koai, G. Müller, A. Seidl, Global simulation of heat transport, including melt convection in a Czochralski crystal growth processcombined finite element/finite volume approach, Mater. Sci. Eng. A 173 (1993) 9–13.

[131] J. Virbulis, T. Wetzel, A. Muiznieks, B. Hanna, E. Dornberger, E. Tomzig, A. Mühlbauer, W. von Ammon, Numerical investigation of silicon melt flow in large diameter CZ crystal growth under the influence of steady and dynamic magnetic fields, J. Cryst. Growth. 230 (2001) 92–99.

[132] D. Lukanin, V. Kalaev, Y. Makarov, T. Wetzel, J. Virbulis, W. von Ammon, Advances in the simulation of heat transfer and prediction of the melt-crystal interface shape in silicon CZ growth, J. Cryst. Growth. 226 (2004) 20–27.

[133] A. Yeckel, A. Pandy, J. Derby, in: G. D. V. Davis, E. Leonardi (Eds.), Advances in Computational Heat Transfer, Vol. II, Begell House Inc., New York, 2001, p. pp.1193.

[134] A. Yeckel, G. Compere, A. Pandy, J. Derby, Three-dimensional imperfections in a model vertical bridgman growth system for cadmium zinc telluride, J. Cryst. Growth. 263 (2004) 629–644.

[135] A. Yeckel, L. Lun, J. J. Derby, An approximate block newton method for coupled iterations of nonlinear solvers: Theory and conjugate heat transfer applications, Journal of Computational Physics 228 (2009) 8566–8588.

[136] A. Yeckel, A. Pandy, J. J. Derby, Fixed-point convergence of modular, steady-state heat transfer models coupling multiple scales and phenomena for meltcrystal growth, Int. J. Numer. Meth. Engng 67 (2006) 1768–1789.

[137] J. J. Derby, L. Lun, A. Yeckel, Strategies for the coupling of global and local crystal growth models, J. Cryst. Growth. 303 (2007) 114–123.

[138] G. J. Galvin, J. W. Mayer, P. S. Peercy, Solidification kinetics of pulsed laser melted silicon based on thermodynamic considerations, Applied Physics Letters 46 (1985) 644 – 646.

[139] C. T. Tsai, O. W. Dillon, R. J. D. Angelis, Techniques to predict dislocation generation during growth of silicon ribbon, Journal of Engineering Materials and Technology 109 (1987) 209–215.

[140] C. T. Tsai, On the finite element modeling of dislocation dynamics during semiconductor crystal growth, J. Cryst. Growth. 113 (1991) 449–507.

[141] C. T. Tsai, N. Subramanyam, The numerical modeling of dislocation generation in semiconductor crystals during Czochralski growth, Modelling Simul. Mater. Sci. Eng. 3 (1995) 93–105.

[142] M. M. Myshlyaev, V. I. Nikitenko, V. I. Nesterenko, You have full text access to this contentdislocation structure and macroscopic characteristics of plastic deformation at creep of silicon crystals, Physica Status Solidi (B) 36 (1969) 8996.

[143] W. D. Sylwestrowicz, Mechanical properties of single crystals of silicon, Philosophical Magazine 7 (1962) 1825–1845.

[144] P. Haasen, Zur plastischen verformung von germanium und insb, Z. Phys 167 (1962) pp.461.

[145] H. Alexander, P. Haasen, Dislocations and plastic flow in the diamond structure, Solid Slate Physics 22 (1968) pp.22.

[146] P. Haasen, in: A. R. Rosenfield, G. T. Hahn, J. A. L. Bement, , I. Jaffee (Eds.), Dislocation Dynamics, McGraw-Hil, New York, 1967, p. pp.701.

[147] I. Yonengo, K. Sumino, Dislocation dynamics in the plastic deformation of silicon crystals, I. Experiments, Phys. Stat. Sol. (a) 50 (1978) pp.685.

[148] M. Suezova, K. Sumino, I. Yonenago, Dislocation dynamics in the plastic deformation of silicon crystals, II. Theoretical analysis of experimental results, Phys. Stat. Sol. (a), 51 (1979) pp.217.